Boston University

OpenBU **http://open.bu.edu**

Boston University Theses & Dissertations Boston University Theses & Dissertations

2022

Mitigation of chromium poisoning in solid oxide fuel cell cathodes

https://hdl.handle.net/2144/44781

Downloaded from OpenBU. Boston University's institutional repository.

BOSTON UNIVERSITY

COLLEGE OF ENGINEERING

Dissertation

MITIGATION OF CHROMIUM POISONING IN SOLID OXIDE FUEL CELL CATHODES

by

ZHIKUAN ZHU

B.Eng., Northeastern University (China), 2011
M.Eng., Boston University, 2017

Submitted in partial fulfillment of the

requirements for the degree of

Doctor of Philosophy

2022

© 2022 by
ZHIKUAN ZHU
All rights reserved except for
Chapter 2, which is © 2020 Elsevier,
Chapter 3, which is © 2020 Elsevier, and
Chapter 6, which is © 2021 Springer

Approved by

First Reader _____

Soumendra N. Basu, Ph.D.
Professor of Mechanical Engineering
Professor and Associate Division Head of Materials Science and Engineering

Second Reader _____

Uday B. Pal, Ph.D.
Professor of Mechanical Engineering
Professor of Materials Science and Engineering

Third Reader _____

Srikanth Gopalan, Ph.D.
Associate Professor of Mechanical Engineering
Associate Professor of Materials Science and Engineering

Fourth Reader _____

Chuanhua Duan, Ph.D.
Associate Professor of Mechanical Engineering
Associate Professor of Materials Science and Engineering

DEDICATION

This work is dedicated to my parents, Yinpeng Zhu and Yumin Liu.

ACKNOWLEDGMENTS

First and foremost, I would like to express my sincere gratitude to my academic advisor Prof. Soumendra N. Basu. Without his expert guidance and constant encouragement, I could not have finished this dissertation. I enjoyed the time working in the group and discussing research with him.

I would like to thank Prof. Uday B. Pal, whose thermodynamic course is one of the reasons why I decided to start my Ph.D. career in this area. I would like to thank Prof. Srikanth Gopalan for his valuable suggestions at group meetings. I would also like to thank Prof. Xin Zhang for her pertinent advice during my master's program.

I would like to thank Prof. Chuanhua Duan and Prof. Sheryl Grace for their willingness to give their time to serve on my committee and as chair.

I am also grateful to Dr. Alexey Nikiforov, Ms. Anlee Krupp, Dr. Jeffrey Bacon for their help with TEM, SEM, and XRD. Thanks to Mr. Bob Sjostrom, Ms. Kara Mogensen for their help in the EPIC center.

I would like to thank ME and MSE staff members, Ms. Selam Woldeselassie, Ms. Nichole Lawton, Ms. Anna Masland, Ms. Patty Robinson-Angel, and Ms. Elizabeth Flagg for their help with administrative issues.

I would like to acknowledge my colleagues for their friendship and experimental assistance. I would like to thank Ms. Michelle Sugimoto for her collaboration with the electrochemical cleaning experiments and Mr. Chibuzor Darl-Uzu for his help with high temperature x-ray diffraction experiments. Thanks also to Dr. Zhihao Sun, Dr. Ruofan Wang, Dr. Yanchen Lu, Mr. Haoxuan Yan, Mr. Ben Levitas, Ms. Jillian Rix, Ms. Ayesha

Akte, Dr. Jicheng Guo Dr. Yiwen Gong, Dr. Jane Banner, Dr. Paul Gasper, Dr. Boshan Mo, and my previous colleagues Dr. Xiaoguang Zhao, Dr. Guangwu Duan, Dr. Aobo Li, Dr. Xuefei Wu, Mr. Yishen Lu, and Dr. Yuanqiao Wu.

I would like to acknowledge Prof. Mark Horenstein and Mr. Neeraj Basu for their help with design and fabrication of the AC EPD controller. I would like to acknowledge Dr. A. Mohammed Hussain, Dr. Song Dong, Dr. Nilesh Dale, and Dr. Yosuke Fukuyam from Nissan Technical Center North America (NTCNA) for their valuable suggestions on the coatings research. I would like to acknowledge Ms. Yi Zhang from SOFCMAN, China, for her help with the supply of solid oxide fuel cells.

The research related to electrochemical cleaning was supported, in part, by the U. S. Department of Energy, Office of Fossil Energy under Award Number DE-FE0031206. The research related to electrophoretically deposited coatings was supported, in part, by a grant from NTCNA. Their support is gratefully acknowledged.

MITIGATION OF CHROMIUM POISONING IN

SOLID OXIDE FUEL CELL CATHODES

ZHIKUAN ZHU

Boston University College of Engineering, 2022

Major Professor: Soumendra N. Basu, Ph.D., Professor of Mechanical Engineering, Professor and Associate Division Head, Division of Materials Science and Engineering

ABSTRACT

Solid oxide fuel cells (SOFCs) have several advantages as electrochemical energy generation devices, including high energy conversion efficiency, easily sequesterable emissions, and high fuel flexibility. However, durability issues still limit the commercial viability of SOFCs. At high temperature operating conditions, volatile hexavalent chromium oxide/hydroxide species are formed from the thermally grown oxide (TGO) scale on stainless-steel interconnects. These vapor phase species are reduced and deposited on the electrochemically active areas in the cathode. This phenomenon, known as 'chromium poisoning,' is one of the primary reasons for long-term degradation of SOFC performance. In this study, two strategies were explored to mitigate Cr poisoning.

The first strategy is 'electrochemical cleaning', based on periodic reversible operation in a solid oxide electrolyser cell (SOEC) mode, which mitigates the deleterious effects of chromium poisoning by oxidizing the deposits species back into the vapor phase. Electrochemical cleaning of cells with lanthanum strontium manganite (LSM) cathodes showed that under the conditions tested, deposited Cr_2O_3 can be effectively removed, significantly reversing the deleterious effects of chromium poisoning. However, Cr-Mn

spinel deposits that were also formed at the cathode/electrolyte interface remain. In order to demonstrate that electrochemical cleaning can be carried out periodically without damaging the cell, cells were subjected to three cycles of repeated poisoning and cleaning. It was found that a similar level of degradation and recovery happened after each cycle. After the third cycle, the cell still maintained the initial level of power output, indicating that periodic electrochemical cleaning under mild electrolytic conditions is an effective method to reverse chromium poisoning without damaging the cell.

The second strategy explored was the deposition of protective coatings on the stainless-steel interconnects. Deposition of spinel coatings by DC and AC electrophoretic deposition (EPD) on flat and porous SUS 430 stainless steel substrates was studied. The required variations in deposition parameters to obtain uniform EPD coatings on porous substrates with increasing geometrical complexity were explored. Four spinel compositions for these coatings were studied; $CuMn_2O_4$, $CuNi_{0.2}Mn_{1.8}O_4$, $MnCo_2O_4$, and $MnFe_{0.34}Co_{1.66}O_4$. The coatings were evaluated based on multiple criteria; including phase stability, microstructural stability, conductivity, Cr gettering ability, ability to act as a diffusion barrier to outward chromium and inward oxygen diffusion at 700ºC and 800ºC in dry and humid air, and the ability to limit the increase in the area specific resistance (ASR) during high temperature oxidation exposures. The results showed that $CuNi_{0.2}Mn_{1.8}O_4$ was the best candidate for the coatings.

TABLE OF CONTENTS

DEDICATION iv

ACKNOWLEDGMENTS v

TABLE OF CONTENTS ix

LIST OF TABLES xiii

LIST OF FIGURES xiv

LIST OF ABBREVIATIONS xx

1. Introduction 1

1.1 Solid oxide fuel cells 1

1.2 Applications of solid oxide fuel cells 2

1.3 Types of solid oxide fuel cells 3

1.4 Materials for cell fabrication 4

1.4.1 Cathode materials 4

1.4.2 Anode materials 6

1.4.3 Electrolyte materials 7

1.5 Interconnect materials for SOFC stacks 8

1.5.1 Requirements for interconnect material 8

1.5.2 Ceramic interconnect materials 8

1.5.3 Metallic interconnect materials 9

1.6 Chromium poisoning in solid oxide fuel cell cathodes 9

1.6.1 Mechanism of chromium poisoning 9

1.6.2 Mitigation strategies 12

1.7 Mechanism of electrochemical cleaning 13

1.8 Electrophoretic deposition of protective layers on SOFC interconnects 15

1.8.1 Introduction of EPD coating 15

1.8.2 Material selection for protective coatings on SOFC interconnects 17

2. Electrochemical cleaning: Demonstration of feasibility 19

2.1 Introduction 19

2.2. Experimental methods 19

2.2.1 Cell fabrication 19

2.2.2 Experimental set-up 21

2.2.3 Cell testing details 22

2.3 Results and Discussion 24

2.4 Conclusions 33

3. Electrochemical cleaning: Multiple cycles 35

3.1 Introduction 35

3.2 Experimental Methods 35

3.3 Results and Discussion 38

3.4 Conclusions 45

4. Comparison of Cu-Mn and Mn-Co spinel coatings 47

4.1 Introduction 47

4.2 Experimental methods 48

4.2.1 Spinel powder fabrication 48

4.2.2 Spinel bar samples fabrication and conductivity measurement 48

4.2.3 The solubility limit of Cr_2O_3 in Cu-Mn and Mn-Co spinels 49

4.2.4 Electrophoretic deposition and two-step densification 50

4.2.5 Oxidation test for spinel coated samples 54

4.2.6 Characterization of spinel samples 55

4.3 Results and Discussion 55

4.3.1 Phase stability 55

4.3.2 Conductivity measurements 57

4.3.3 EPD coating and densification 58

4.3.4 Oxidation tests for spinel coated Samples 60

4.3.5 ASR measurements for 800°C oxidation tests 65

4.3.6 High humidity oxidation tests 65

4.3.7 Interaction between Cr_2O_3 and spinel 71

4.4 Conclusions 73

5. Composition optimization of $CuNi_xMn_{2-x}O_4$ 75

5.1 Introduction 75

5.2 Phase stability 75

5.3 Conductivity measurements 76

5.4 Microstructure of EPD coatings 78

5.5 Oxidation tests for spinel coated samples 79

5.6 Conclusions 82

6. Alternating current EPD on porous substrates 84

6.1 Introduction 84

6.2 Experimental Methods 85

6.3 Results and Discussion 88

6.4 Conclusions 95

7. Conclusions 96

8. Contributions and Recommendations for Future Work 99

8.1 Original Contributions 99

8.2 Future work on electrochemical cleaning 99

8.3 Future work on spinel coatings for interconnects 99

BIBLIOGRAPHY 101

CURRICULUM VITAE 115

LIST OF TABLES

Table 1. Experimental conditions for all cells at 800°C. 36

Table 2. EPD parameters used in this study 53

Table 3. Cr solubility in all spinel samples. 73

Table 4. Summary of comparative spinel properties. 74

LIST OF FIGURES

Figure 1. Schematic of the operation principles of a SOFC. 1

Figure 2. Schematic of (a) planar SOFC and stack (b) tubular SOFC and stack..... 4

Figure 3. Schematic of the mechanism of chromium poisoning in SOFCs..... 10

Figure 4. SEM images of LSM-YSZ based cathode in (a) the as-processed (clean) condition, and (b) after 50h operation at 800 °C in the air with 0.5A/cm^2 loading. 11

Figure 5. Schematic of strategies to mitigate chromium poisoning..... 12

Figure 6. Mechanisms for (a) chromium poisoning and (b) electrochemical cleaning of Cr deposits at a triple phase boundary, which occur in fuel cell (SOFC) mode and electrolyser (SOEC) mode, respectively. 14

Figure 7. A schematic of the EPD apparatus. 16

Figure 8. Schematic of the screen-printed cell structure (left). SEM micrograph of the screen-printed cell cross-section (right). 20

Figure 9. A schematic of the cell test setup. 21

Figure 10. I-V curves for the cell operated at 800°C under varying fuel humidity values at the fuel electrode and dry air at the air electrode. The condition used in this study is marked as X. Positive current corresponds to the SOFC mode and negative current to electrolytic mode..... 23

Figure 11. Current voltage curves for the (a) poisoned baseline cell, and the (b) electrochemically cleaned cell. Measurements were obtained at 800°C under dry air (air side) and 2% humidified H_2 (fuel side). 25

Figure 12. EIS curves for the (a) poisoned baseline cell and (b) electrochemically cleaned cell. Measurements were taken at 800°C under dry air (air side) and 2% humidified H_2 (fuel side) under open circuit condition..... 26

Figure 13. SEM micrograph of cathode/electrolyte interface for an untested cell with the sample holder a) with no tilt and b) tilted at 30º. The interface is clean with no deposits observed. SEM micrograph of the electrolyte surface in the (c) poisoned baseline cell, with large and small deposits visible in regions marked as 1 and 2.

SEM micrograph of the electrolyte surface in the (d) electrochemically cleaned cell, showing that the larger faceted deposits remain (region marked as 3) and the finer deposits are no longer present (region marked as 4). For micrographs (c) and (d), the sample holder is tilted at 30º. 28

Figure 14. The red EDS spectra are taken from (a) a large, faceted deposit (Region 1 in Figure 13c) and from (b) a region with many fine, rounded deposits (Region 2 in Figure 13c) in the poisoned baseline cell. The red EDS spectra are taken from (c) a large, faceted deposit (Region 3 in Figure 13d) and from (d) a region without deposits (Region 4 in Figure 13d) on the electrolyte surface in the electrochemically cleaned cell. All spectra are scaled to the blue reference spectrum for pure LSM. 30

Figure 15. Plot of Cr/La (atomic%) ratio, quantified using EDS measurements, as a function of the distance from the electrolyte into the cathode. 32

Figure 16. (a) I-V curves of Cell 1 after activation and after poisoning for 25 hours. (b) I-V curves for Cell 2 after the first poisoning/electrochemical cleaning cycle. (c) EIS curves for cell 2 during the first poisoning/electrochemical cleaning cycle. (d)Voltage versus time plot for cell 2 during the first electrochemical cleaning. (e) I-V curves for Cell 2 after the second poisoning/electrochemical cleaning cycle. (f) I-V curves for Cell 2 after the third poisoning/electrochemical cleaning cycle..... 40

Figure 17. I-V curves for the electrochemical reference cell (Cell 3) (a) after activation and after SOFC exposure, and (b) after SOFC exposure, after SOEC exposure, and after overnight activation of 12 hours. 41

Figure 18. (a) SEM micrograph of the cathode/electrolyte interface of Cell 1 after Cr-poisoning. (b) SEM micrograph of the cathode/electrolyte interface of Cell 3 after three poisoning/electrochemical cleaning cycles. (c) EDS spectra from Cell 1 after poisoning, and (d) from Cell 3 after three poisoning/electrochemical cleaning cycles. The red EDS spectra were taken from regions marked in the SEM micrographs. All spectra are scaled to the blue reference spectrum from an

as-processed LSM/YSZ cathode. SEM micrographs of Cell 3 at the (e) cathode/electrolyte interface and at the (f) anode/electrolyte interface..... 44
Figure 19. Conductivity measurements set-up for spinel bar. 49
Figure 20. $CuNi_{0.2}Mn_{1.8}O_4$ spinel powder samples (a) before ball milling, and (b) after ball milling. 50
Figure 21. Spinel powders fabricated after ball-milling with (a) 0.3 mm YSZ balls, (b) 0.1mm YSZ balls, (c) 0.05 mm YSZ balls, (d) 0.03 mm YSZ balls, (e) 0.015 mm YSZ balls. 51
Figure 22. SEM images of spinel powders after ball-milling with (a) 0.03 mm YSZ balls, (b) 0.015 mm YSZ balls. 51
Figure 23. Prototype of EPD chamber for SOFC interconnect samples..... 52
Figure 24. Schematic illustration of the microstructural development during the two-step sintering heat treatment. 54
Figure 25. ASR measurements set-up during oxidation tests. 54
Figure 26. XRD scans of spinel powder samples and SEM images of polished bar samples of (a)$CuMn_2O_4$ (b)$CuNi_{0.2}Mn_{1.8}O_4$ (c) $MnCo_2O_4$ and (d)$MnFe_{0.34}Co_{1.66}O_4$ at room temperature. The red arrows indicate the presence of a second phase in $CuMn_2O_4$, which can be seen as needle like precipitates in the SEM micrograph in (a). 56
Figure 27. Conductivity of spinel bar samples as a function of temperature. 57
Figure 28. Microstructural changes during densification of (a)$CuMn_2O_4$ (b)$CuNi_{0.2}Mn_{1.8}O_4$ (c)$MnCo_2O_4$ and (d) $MnFe_{0.34}Co_{1.66}O_4$ coating samples. The top row shows the as-deposited micristrcuture, the second row shows the microstructure after the reduction anneal, the third row shows the microstructure after the re-oxidation anneal, and the bottom row shows the surface of the coatings after the reoxidation anneal. 58
Figure 29. SEM image (top left) and EDS mapping of $CuNi_{0.2}Mn_{1.8}O_4$ sample after reduction. The top right image is the superposition of all the elemental dot maps. 59

Figure 30. Cross-sectional SEM micrographs of (a) $CuMn_2O_4$, (b) $CuNi_{0.2}Mn_{1.8}O_4$, (c) $MnCo_2O_4$, and (d) $MnFe_{0.34}Co_{1.66}O_4$ samples after 100 h oxidation at 700°C (top row) and 800°C (bottom row). 60
Figure 31. EDS line scans of Cr across (a) $CuMn_2O_4$, (b) $CuNi_{0.2}Mn_{1.8}O_4$, (c) $MnCo_2O_4$, and (d) $MnFe_{0.34}Co_{1.66}O_4$ samples after densification (light green), after 700°C oxidation (dark green), and 800°C oxidation (dark blue). 62
Figure 32. (a) Cr EDX line scans on uncoated SUS430 reference samples after 100h oxidation in flowing air at 700°C (dark green), and 800°C (dark blue). (b) ASR changes for uncoated SUS430 reference samples during the 700 ℃ (dark green) oxidation test and during the 800°C oxidation test (dark blue)..... 64
Figure 33. Cross-sectional microstructure (top) and surface microstructure (bottom) for uncoated SUS430 reference samples after 100h oxidation in flowing air at (a) 700°C and (b) 800°C. 64
Figure 34. Changes in ASR for spinel coated samples during the 800 ℃ oxidation tests for100 h in flowing air..... 65
Figure 35. Cross-sectional microstructure of (a)$CuMn_2O_4$ (b)$CuNi_{0.2}Mn_{1.8}O_4$ (c)$MnCo_2O_4$ and (d) $MnFe_{0.34}Co_{1.66}O_4$ samples after100 h oxidation at 700℃ in 10% humidified air. 66
Figure 36. EDS line scans of (a) $CuMn_2O_4$, (b) $CuNi_{0.2}Mn_{1.8}O_4$, (c) $MnCo_2O_4$, and (d) $MnFe_{0.34}Co_{1.66}O_4$ samples after 100 h oxidation at 700℃ in 10% humidified air. 67
Figure 37. Cross-sectional microstructure of (a)$CuMn_2O_4$ (b)$CuNi_{0.2}Mn_{1.8}O_4$ (c)$MnCo_2O_4$ and (d) $MnFe_{0.34}Co_{1.66}O_4$ samples after100h oxidation at 700℃ in 20% humidified air. 68
Figure 38. Surface microstructures of (a) $CuMn_2O_4$, (b) $CuNi_{0.2}Mn_{1.8}O_4$, (c) $MnCo_2O_4$, and (d) $MnFe_{0.34}Co_{1.66}O_4$ samples in the as-processed state before oxidation testing in 20% humid air. 69

Figure 39. Surface microstructures of (a) $CuMn_2O_4$, (b) $CuNi_{0.2}Mn_{1.8}O_4$, (c) $MnCo_2O_4$, and (d) $MnFe_{0.34}Co_{1.66}O_4$ samples after100 h oxidation at 700°C in 20% humidified air. 70
Figure 40. EDS line scans of (a) $CuMn_2O_4$, (b) $CuNi_{0.2}Mn_{1.8}O_4$, (c) $MnCo_2O_4$, and (d) $MnFe_{0.34}Co_{1.66}O_4$ samples after 100h oxidation at 700°C in 20% humidified air. 71
Figure 41. XRD scans of products of reactions between varying molar rations of (a) $CuMn_2O_4$, (b) $CuNi_{0.2}Mn_{1.8}O_4$, (c) $MnCo_2O_4$, and (d) $MnFe_{0.34}Co_{1.66}O_4$ spinel powders and Cr_2O_3 powders, after annealing the powder mixtures at 800°C in the air for 6 h in air. 72
Figure 42. XRD scans of (a) $CuMn_2O_4$, (b) $CuNi_{0.2}Mn_{1.8}O_4$, (c) $CuNi_{0.4}Mn_{1.6}O_4$, and (d) $CuNi_{0.6}Mn_{1.4}O_4$ powders at room temperature. 76
Figure 43. The conductivity of undoped and various Ni-doped Cu-Mn spinels as a function of temperature. 77
Figure 44. SEM images of polished cross-sections of (a) $CuMn_2O_4$, (b) $CuNi_{0.2}Mn_{1.8}O_4$, (c) Cu $Ni_{0.4}Mn_{1.6}O_4$, and (d) $CuNi_{0.6}Mn_{1.4}O_4$ bar samples. 77
Figure 45. Cross-sectional microstructure of (a) $CuMn_2O_4$, (b) $CuNi_{0.2}Mn_{1.8}O_4$, (c) $CuNi_{0.4}Mn_{1.6}O_4$, and (d) $CuNi_{0.6}Mn_{1.4}O_4$ samples after the re-oxidation anneal. 78
Figure 46. Surface microstructure of (a) $CuMn_2O_4$, (b) $CuNi_{0.2}Mn_{1.8}O_4$, (c) $CuNi_{0.4}Mn_{1.6}O_4$, and (d) $CuNi_{0.6}Mn_{1.4}O_4$ coatings before the oxidation test. .. 80
Figure 47. Surface microstructures of (a) $CuMn_2O_4$, (b) $CuNi_{0.2}Mn_{1.8}O_4$, (c) $CuNi_{0.4}Mn_{1.6}O_4$, and (d) $CuNi_{0.6}Mn_{1.4}O_4$ coating samples after100 h oxidation at 800°C in air. 80
Figure 48. Cross-sectional microstructures of (a) $CuMn_2O_4$, (b) $CuNi_{0.2}Mn_{1.8}O_4$, (c) $CuNi_{0.4}Mn_{1.6}O_4$, and (d) $CuNi_{0.6}Mn_{1.4}O_4$ samples after100h oxidation at 800°C in air. 81
Figure 49. EDS line scans of (a)$CuMn_2O_4$ (b)$CuNi_{0.2}Mn_{1.8}O_4$ (c) $CuNi_{0.4}Mn_{1.6}O_4$ (d) $CuNi_{0.6}Mn_{1.4}O_4$ samples after 100h oxidation at 800°C in air. 82

Figure 50. AC signal generating setup. 86
Figure 51. AC signal used for deposition. 87
Figure 52. SEM micrographs of cross-sections of (a) as-deposited DC EPD sample, (b) as-deposited AC EPD sample, and (c) AC EPD sample after the two-step densification process. The top parts of the images show pores in the middle of the samples, while the bottom parts of the images show near-surface pores... 89
Figure 53. Surface microstructure of (a) uncoated sample and (b) $CuNi_{0.2}Mn_{1.8}O_4$ coated and densified sample. 90
Figure 54. Low magnification SEM image, and EDS mapping of coated sample after two-step densification and 100h oxidation test. 91
Figure 55. Plot of weight gain per unit area measured by thermogravimetry of (a) uncoated sample and (b) coated sample as a function of time. ASR changes as a function of time for uncoated sample (c) and coated sample (d). All the data are measured at 700°C in air. 93
Figure 56. SEM micrographs of cross-sections after 100h oxidation test at 700°C in air, of (a) uncoated sample and (b) coated sample. EDS line scans across the (c) TGO/substrate in the uncoated sample, and (d) coating/TGO/substrate in the coated sample. 94

LIST OF ABBREVIATIONS

AC	Alternating Current
AFC	Alkaline Fuel Cell
ASR	Area Specific Resistance
BOP	Balance of Plant
CHP	Combined Heat and Power System
CTE	Coefficient of Thermal Expansion
CVD	Chemical Vapor Deposition
DC	Direct Current
DMFC	Direct Methanol Fuel Cell
EDS	Energy Dispersive X-ray Spectroscopy
EIS	Electrochemical Impedance Spectroscopy
EPD	Electrophoretic Deposition
GDC	Gadolinia Doped Ceria
GNP	Glycine Nitrate Process
HT-SOFC	High-Temperature Solid Oxide Fuel Cell
IT-SOFC	Intermediate Temperature Solid Oxide Fuel Cell
I-V	Current-Voltage
LSC	Lanthanum Strontium Cobaltite
LSCF	Lanthanum Strontium Cobalt Ferrite
LSF	Lanthanum Strontium Ferrite
LSM	Strontium Doped Lanthanum Manganite

MCFC	Molten Carbonate Fuel Cell
MIEC	Mixed Ionic and Electronic Conductivity
OCV	Open Circuit Voltage
ORR	Oxygen Reduction Reaction
PAFC	Phosphoric Acid Fuel Cell
PEMFC	Proton Exchange Membrane Fuel Cell
PLD	Pulsed Laser Deposition
PVD	Physical Vapor Deposition
SAFC	Solid Acid Fuel Cell
SCZ	Scandia Stabilized Zirconia
SDC	Samarium Doped Ceria
SEM	Scanning Electron Microscopy
SOFC	Solid Oxide Fuel Cell
TEM	Transmission Electron Microscopy
TGA	Thermogravimetric Analysis
TGO	Thermal Growth Oxide
TPB	Triple Phase Boundary
XRD	X-ray Diffraction
YCCN	Nickel Doped Yttrium Chromite
YSZ	Yttria Stabilized Zirconia

1. Introduction

1.1 Solid oxide fuel cells

Solid oxide fuel cells (SOFCs) are electrochemical devices that generate electricity directly from fuels using electrochemical reactions with the oxidant. SOFCs have several advantages as energy generation devices, including high energy conversion efficiency, easily sequesterable emissions, and high fuel flexibility. Unlike a battery, a fuel cell can keep generating electricity as long as the fuel and oxidant supply is provided [1, 2].

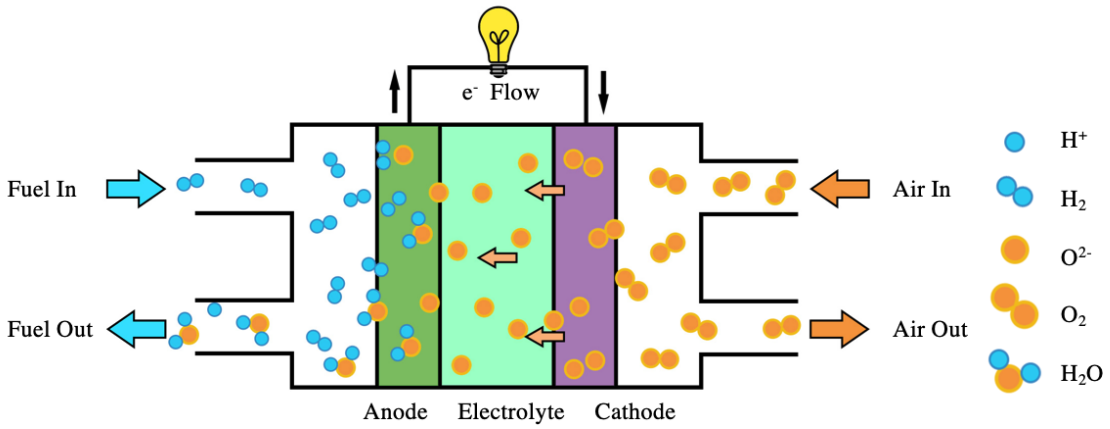

Figure 1. Schematic of the operation principles of a SOFC.

A single SOFC cell consists of a dense ceramic electrolyte sandwiched between a porous cathode electrode and a porous anode electrode. The operating principle of a SOFC is schematically shown in Figure 1. When an external load is applied, an oxygen molecule is reduced at the porous cathode electrode to produce two oxide ions. This is called the oxygen reduction reaction (ORR). These ions migrate through the solid electrolyte to the anode electrode side, and then react with the fuel such as hydrogen, to produce water. At

the same time, electrons from the anode side migrate through the external load to the cathode side, providing electricity. The solid electrolyte only has sufficient ionic conductivity at high operation temperatures, so SOFCs are usually operated at 600 ℃ to 800 ℃ [3-5].

Besides SOFCs, there are several other types of fuel cells, including alkaline fuel cell (AFC), solid acid fuel cell (SAFC), phosphoric acid fuel cell (PAFC), molten carbonate fuel cell (MCFC), proton exchange membrane fuel cell (PEMFC) and direct methanol fuel cell (DMFC). These fuel cells are classified based on the different materials used for electrolytes. Even though they use different fuels, and work under different conditions, they all operate with the same basic principles [2, 4].

1.2 Applications of solid oxide fuel cells

The major application for SOFCs is for distributed stationary power generation ranging from hundreds of kWs to MW. This system consists of a fuel processor, desulphurizing part, fuel cell power module, power conditioning equipment for AC and DC converter, and process gas heat exchanger. Synthetic gas (hydrogen and carbon monoxide mixtures) formed by reformation of methane is typically used as fuel for these SOFCs [6, 7].

Another application of SOFCs is secondary power generation of long-haul trucks, where electricity generated by SOFCs is used to power the cabin when the trucks are off-road. There is also ongoing research on SOFC-powered cars due to their high efficiency and lower emissions. However, the need for rapid start-up and shut-down of these systems

remains a challenge. This is being addressed by research on reducing the working temperature, which would alleviate these issues [3, 8].

The electrochemical reactions used to generate electricity in SOFCs are typically exothermic and can lead to large amounts of heat as a by-product. This leads to high temperature exhaust gases that can be used to drive a gas turbine to generate more electricity and can also provide heat or hot water. This type of combined heat and power (CHP) systems are being explored for residential and small businesses units [3].

Due to the modularity and flexibility in the choice of fuels, SOFC systems can be used in small and portable. In remote applications with no natural gas supply, bottled gas can be directly used for electricity generation [7, 9].

1.3 Types of solid oxide fuel cells

One single cell can only produce around 0.5W to 1W of DC electricity. In order to generate enough power, cells must be combined together to work in series or in stacks [5, 7]. There are two major types of SOFCs. The first type is flat-plate or planar SOFC. A single cell is configured as flat plates usually in square or circular shapes. Stacks based on this type of SOFC connect cells in series using interconnects (or separators) as shown in Figure 2a. During operation, air and fuel flow through separate channels on either side of the interconnects.

The second type is tubular SOFC. The single cell is configured as a tube. The stack consists of a bundle of single cell tubes. A common design is a cathode-supported tube closed at one end. The electrolyte and anode are concentrically placed outside the cathode.

During operation, air flows inside the tube, and fuel flows outside the tube as shown in Figure 2b.

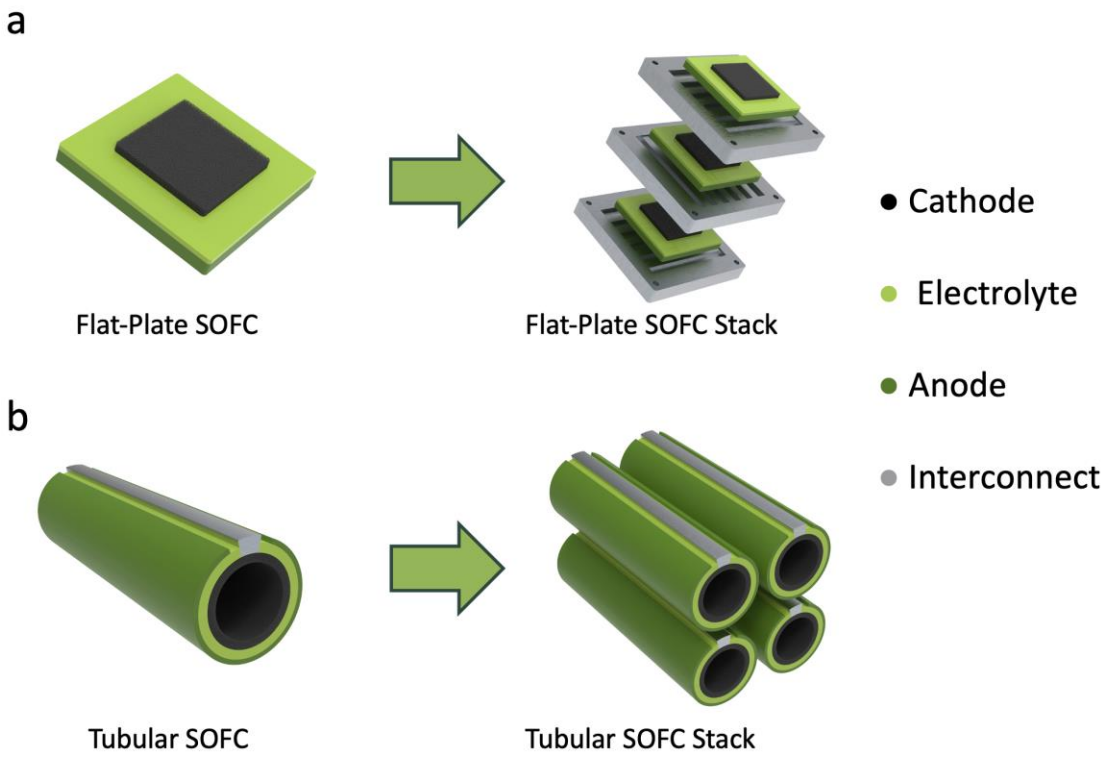

Figure 2. Schematic of (a) flat-plate SOFC and stack (b) tubular SOFC and stack.

1.4 Materials for cell fabrication

1.4.1 Cathode materials

The cathode electrodes work in the oxidation environment and participate in the oxygen reduction reaction. Oxygen is reduced to oxygen ions and consumes two electrons. The cathode material should have high electronic conductivity, high chemical and physical stability in oxidizing environments in operating temperatures in contact with the electrolyte,

matched thermal expansion coefficient with the electrolyte, and be able to be fabricated in a porous structure for gas transport [10, 11].

Lanthanum manganite doped with alkaline and rare earth elements is widely used for cathode fabrication. The electronic conductivity of lanthanum manganite is due to electron hopping between Mn^{+3} and Mn^{+4}. Doping divalent ions can significantly increase the conductivity. Strontium doped lanthanum manganites (LSM) are recognized as the best lanthanum manganite-based cathode materials and are widely used in industry. Doping with strontium not only reduces Mn^{+4} to Mn^{+3} but also creates oxygen vacancies due to the substitution of La^{3+} by Sr^{2+}. LSM has high electronic conductivity (200 S/cm at 800°C) but negligible oxygen ion conductivity (10^{-8} S/cm at 800°C). Therefore, the oxygen reduction reaction occurs only at the triple-phase boundary (TPB), where the LSM/YSZ and air meet. For a LSM cathode on a YSZ electrolyte, TPBs are only located at the cathode/electrolyte interface. Mixing YSZ with the LSM in the cathode increases the cathode ionic conductivity and reduces cathodic activation polarization. Moreover, it also increases the total TPB density and leads to improved cathode performance [12].

Another class of cathode materials has mixed ionic and electronic conductivity (MIEC). In a MIEC cathode, the ORR reaction can occur on the entire air/cathode interface and not just the cathode/electrolyte interface. Lanthanum strontium ferrite (LSF), lanthanum strontium cobaltite (LSC), and lanthanum strontium cobalt ferrite (LSCF) are the most widely used MIEC cathode materials. Typically, MIEC cathodes perform better than electronically conducting cathodes such as LSM. However, these materials suffer from poor chemical stability due to the reaction with the YSZ electrolyte. Therefore, an

additional barrier layer is required between the cathode and electrolyte. Gadolinium doped ceria (GDC) and samarium doped ceria (SDC) are commonly used barrier materials [13].

1.4.2 Anode materials

The anode electrodes work in a reducing environment and provide pathways for fuel oxidation and electron release. Anode material should have high electrical conductivity, high electrocatalytic activity for the fuel oxidation reaction, matched CTE and compatibility with the electrolyte, and phase stability in the high temperature reducing environments, and be able to be fabricated in a porous structure for gas transport. Metals such as nickel have high catalytic activity toward the fuel oxidation reduction and are stable in reducing conditions present on the fuel side [14]. The fuel oxidation reaction occurs at the TPBs between the ionic conducting phase (YSZ), electronic conducting phase (Ni) and the fuel (pores). Typically, in planar cells, the anode is thick and provides mechanical support to the cell.

Porous stainless steels such as SUS430 are becoming more popular as anode support material in low-temperature SOFC. They have high mechanical properties and structure reliability, high conductivity, and low cost. Ferritic stainless steels are well matched the CTE with electrolyte. The Cr in these stainless steels form a passivation layer of Cr_2O_3 and $CrMn_2O_4$ on the surface of alloy grains and limit further oxidation [15, 16].

Ceramic materials such as lanthanum chromite, strontium titanate, and fluorite materials based on ceria have also been investigated. They show higher stability than metals and have reasonable electronic conductivity. However, ceramic anodes have to be operated at higher temperatures (~ 1000°C) and have higher fabrication costs [17].

Ni and YSZ cermets are most commonly used as anode materials. The Ni phase has high catalytic activity towards the fuel oxidation reaction, but also has a much higher CTE than the electrolyte. The YSZ phase reduces the CTE of the anode to match it to the electrolyte. The mixture of Ni and YSZ phases also introduces TPBs throughout the thickness of the anode, ensuring that electrochemical reactions do not just occur at the anode/electrolyte interface. Disadvantages of Ni-YSZ anodes include coarsening of Ni phase at high temperatures, and poisoning due to impurities in the fuel, which leads to a reduction in catalytic activity in the anode [18].

1.4.3 Electrolyte materials

The electrolyte is exposed to both the fuel-side and air-side environments. It must be chemically stable in both oxidizing and reducing atmospheres. It must have the ability to be processed as a thin dense layer to minimize ohmic losses and prevent direct reactions between the fuel and oxidant, and should be adherent to the anode and cathode without deleterious chemical reactions with anode and cathode materials. Most importantly, electrolyte materials must have high oxygen ion conductivity and negligible electronic conductivity.

Zirconia (ZrO_2) based materials are most commonly used for electrolytes. On heating pure ZrO_2, the crystal structure transfers from monoclinic to tetragonal, which results in high stresses. By doping with a lower oxidation state cation Y^{3+}, the crystal structure becomes stable. Thus yttria-stabilized zirconia (YSZ) is the most widely used electrolyte material [12, 18]. Scandia stabilized zirconia (SCZ) has also been explored as an electrolyte material. It has higher ionic conductivity (0.12 S/cm at 800°C) than YSZ

(0.01 S/cm at 800°C) but is also more expensive. However, since the electrolyte is quite thin and does not require a lot of material, SCZ is attracting more interest as an electrolyte material [17].

1.5 Interconnect materials for SOFC stacks

1.5.1 Requirements for interconnect material

The interconnects in SOFC stacks connect the cells in series, collect electrons from the electrodes, help distribute the air and fuel to the cathodes and anodes of individual cells, respectively, and insulate the cells from the outside environment [19].

The interconnect material should have high electrical conductivity to limit ohmic loss, high thermal conductivity to remove heat from electrodes and maintain an even temperature distribution, a coefficient of thermal expansion (CTE) match with the electrode and YSZ electrolyte (12×10^{-6}/°C) to reduce the stress during temperature change to avoid delamination, high chemical and thermal stability in both reduction and oxidation environments, good mechanical strength to bear loading and thermal stress, good machinability, and low cost [19-23].

1.5.2 Ceramic interconnect materials

Ceramic interconnect materials are usually used in high-temperature SOFCS (HT-SOFC). The most widely used ceramic material is based on the perovskite structured lanthanum chromite ($LaCrO_3$). It is usually doped with divalent cations such as Sr or Ca to get better sinterability and achieve high conductivity in the working environment. Calcium

and nickel doped yttrium chromite (YCCN) is another candidate, that shows better sinterability in air and compatibility with the YSZ electrolyte. The disadvantage of ceramic interconnects is that they have low electrical and thermal conductivities and high cost for fabrication. The application is limited to the tubular geometry which requires less interconnect material [12].

1.5.3 Metallic interconnect materials

Compared to ceramic interconnects, metallic interconnects are more robust and easier to fabricate into complex geometries. Cr-containing stainless steels, such as SUS430 and Crofer22 APU, are widely used as interconnect materials in SOFC applications. They have high electrical and heat conductivities, matched CTE with YSZ electrolytes, low cost, and high machinability. Most alloys are unstable in air, so oxidation resistance is a key property for interconnect materials. The Cr in the stainless steels increases hardenability and provides oxidation. At operating temperatures (600°C–800°C), thermally grown Cr_2O_3 and $MnCr_2O_4$ form on the surface of these interconnects. These thermally grown oxides (TGO) are excellent diffusion barriers, and they protect the substrate from further oxidation [19, 22, 24, 25].

1.6 Chromium poisoning in solid oxide fuel cell cathodes

1.6.1 Mechanism of chromium poisoning

Durability issues still limit the commercial viability of SOFCs. Although the thermally grown oxides (Cr_2O_3 and $MnCr_2O_4$) scales provide oxidation resistance to the

stainless steels used in interconnects and balance-of-plant (BOP) components, at high temperatures in flowing air, volatile hexavalent chromium oxide/hydroxide species are formed. These Cr-containing vapor phase species are reduced and form Cr-containing deposits at the electrochemically active regions of the cathode (Figure 3). This phenomenon, known as 'chromium poisoning,' is one of the primary mechanisms for the performance degradation of SOFCs [26-29].

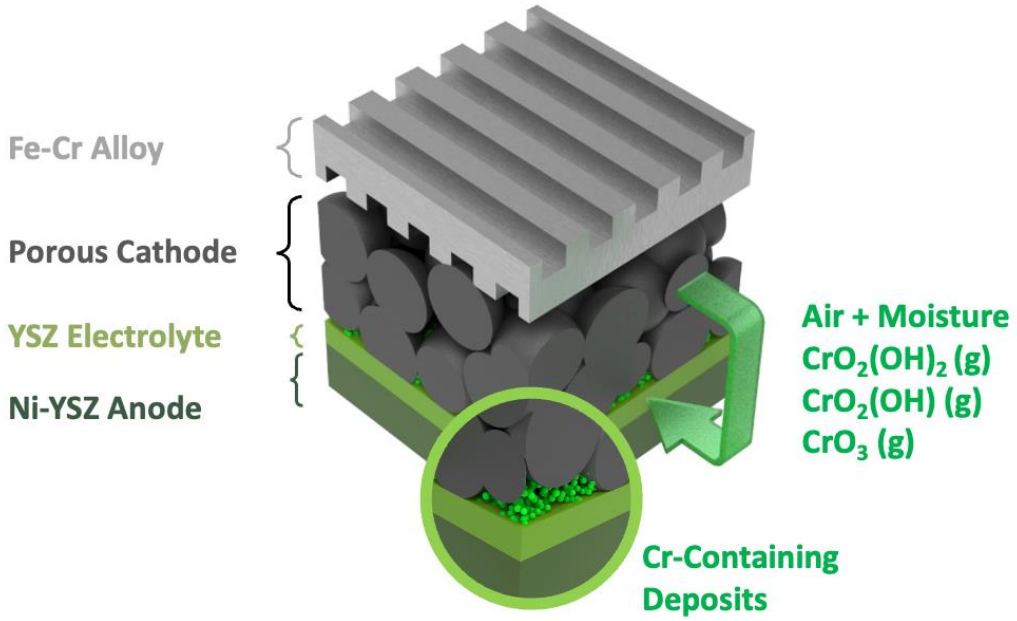

Figure 3. Schematic of the mechanism of chromium poisoning in SOFCs.

Despite intensive research on chromium poisoning, there are still a lack of complete understanding on the nature of the Cr-containing deposits and their effects on cell performance. The consensus is that solid Cr_2O_3 is formed at the surface of the alloy interconnects at high temperatures. Then, Cr-containing vapor species such as CrO_3(g), $CrO_2(OH)_2$(g), and CrO_2OH(g) are generated under airflow, with hydroxide-containing

species formed in the presence of water vapor. Increasing the humidity and temperature may increase the partial pressure of the Cr-containing vapor species [30, 31]. Such Cr species are then electrochemically reduced under current load in the active areas of the porous cathode. This leads to solid-phase deposits in the electrochemically active areas of the cathode, which impedes ORR, thereby poisoning the cathode. Figure 4 shows an example of such solid-phase deposit formation in an LSM-YSZ cathode.

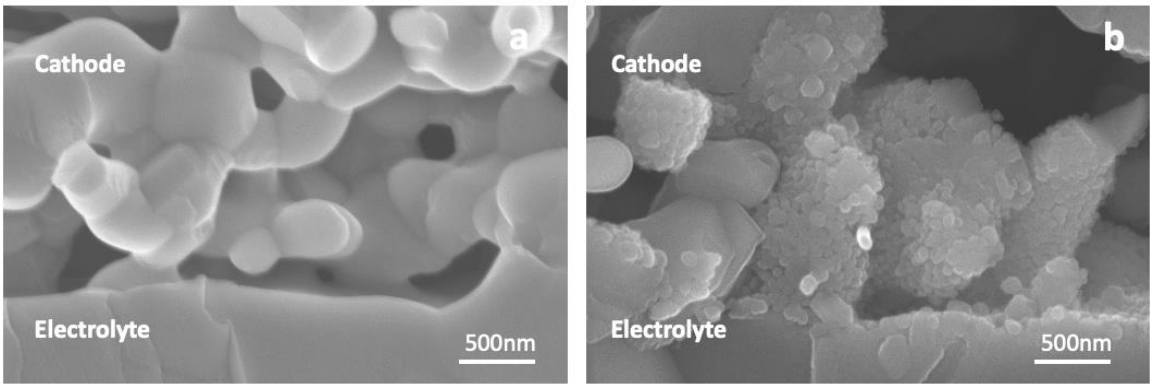

Figure 4. SEM images of LSM-YSZ based cathode in (a) the as-processed (clean) condition, and (b) after 50h operation at 800 ℃ in the air with 0.5A/cm^2 loading.

Different Cr-containing deposits have been found, depending on the cathode material. For lanthanum strontium manganite (LSM) or LSM/yttria-stabilized zirconia (YSZ) based cathodes, the primary deposits have been reported to be Cr_2O_3 and chromium-manganese (Cr, Mn) spinel [26, 32, 33]. For lanthanum strontium cobalt ferrite (LSCF) or lanthanum strontium ferrite (LSF) based cathode, the primary deposits have been reported to be Cr_2O_3 and $SrCrO_4$ [34].

The effects of humidity and cathodic current in chromium poisoning have already been studied in our group [35, 36]. It was found that cathodic current is the driving force

for Cr vapor reduction at the cathode and electrolyte interface. Humidified air promotes higher Cr vapor pressure which increases the deposition rate significantly.

1.6.2 Mitigation strategies

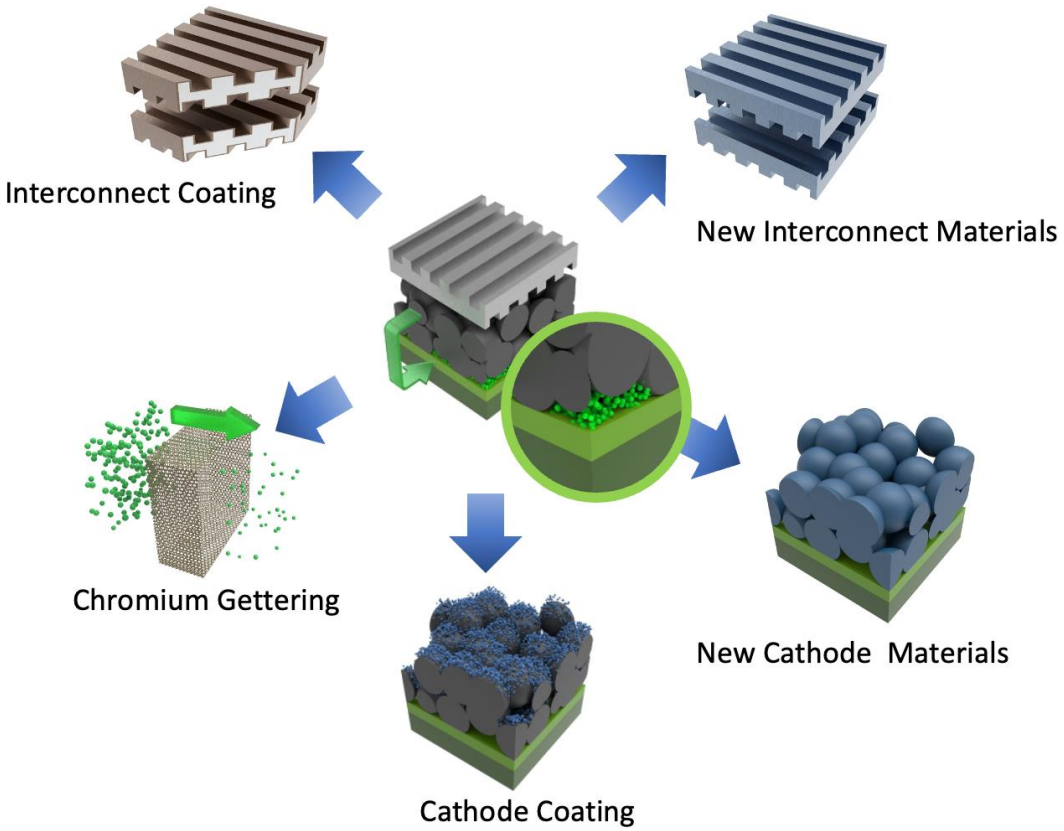

Figure 5. Schematic of strategies to mitigate chromium poisoning.

Many solutions have been proposed to mitigate chromium poisoning, as shown schematically in Figure 5. These include using more Cr-tolerant cathode materials [11, 37, 38], gettering of the Cr-containing vapor species before they reach the cathode [32], applying diffusion resistant coatings on interconnects [39, 40], applying a hybrid catalyst coating on cathode by infiltration [41-45] and using alumina forming alloys for the balance

of plant (BOP) components [46-48]. In all these cases, substantial changes must be made to existing SOFC systems. Many of these techniques impede chromium poisoning for a period but are not able to ensure reliable SOFC performance over the lifetime of the device.

1.7 Mechanism of electrochemical cleaning

Previous studies have shown that the mechanism of Cr poisoning is electrochemical in nature [26, 49-52]. The overall cell reaction equations for Cr deposition involving CrO_3(g), the most abundant Cr-containing vapor species in dry air, and $CrO_2(OH)_2$(g) and CrO_2OH(g), the most abundant in humidified air, are shown below.

$$2CrO_3(g, \text{air side}) + 3H_2(g, \text{fuel side}) = Cr_2O_3(s, \text{air side}) + 3H_2O(g, \text{fuel side}) \quad (1)$$

$$2CrO_2(OH)_2(g, \text{air side}) + 3H_2(g, \text{fuel side}) = Cr_2O_3(s, \text{air side}) + 2H_2O(g, \text{air side}) + 3H_2O(g, \text{fuel side}) \quad (2)$$

$$3CrO_2(OH)(g, \text{air side}) + 3H_2(g, \text{fuel side}) = 3/2Cr_2O_3(s, \text{air side}) + 3/2H_2O(g, \text{air side}) + 3H_2O(g, \text{fuel side}) \quad (3)$$

These above equations require the transport of oxygen ions across the electrolyte from the air side to the fuel side. In the electrochemical cleaning method, the Cr deposition reactions are reversed by operating the device in reverse, i.e., as a solid oxide electrolyser cell (SOEC). During the application of an electrolytic current, oxygen ions are transported across the electrolyte to the air side from the fuel side, converting the deposited Cr_2O_3 into

Cr-containing vapors species. This reaction is enhanced by increasing the temperature and the humidity on the air side.

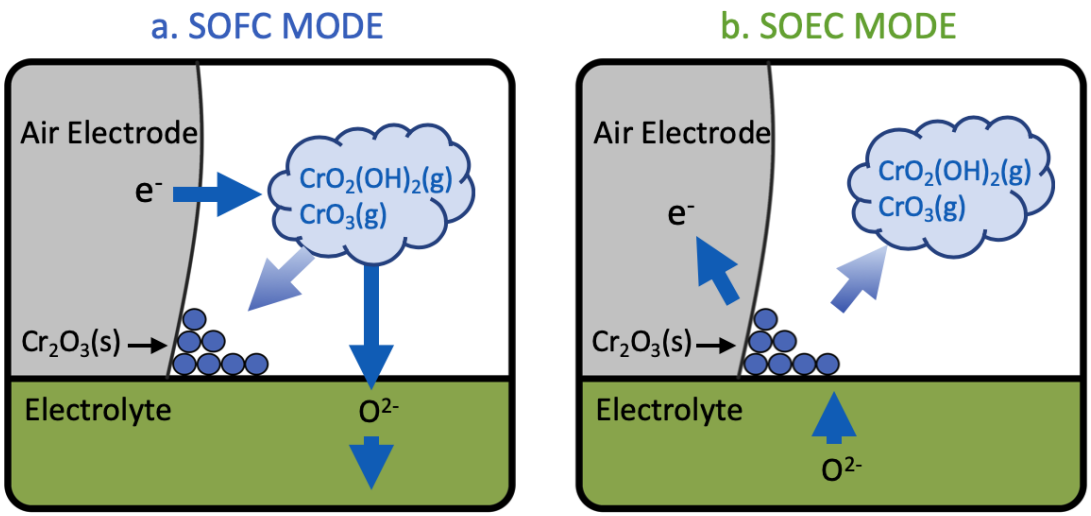

Figure 6. Mechanisms for (a) chromium poisoning and (b) electrochemical cleaning of Cr deposits at a triple phase boundary, which occur in fuel cell (SOFC) mode and electrolyser (SOEC) mode, respectively.

The poisoning and cleaning mechanisms are shown schematically in Figure 6, respectively. Many previous studies have shown that Cr deposition requires the application of cathodic polarization, i.e., SOFC mode. This indicates that the Cr deposition reaction is electrochemical in nature. Thus, we conclude that the Cr deposits can also be removed by electrochemical means. By operating the cell in SOEC mode, i.e., application of anodic polarization, Cr deposition reactions are reversed. Chromium-containing vapor species are reformed from the deposits and leave the system with the airflow.

1.8 Electrophoretic deposition of protective layers on SOFC interconnects

1.8.1 Introduction of EPD coating

Recently, significant research efforts have been focused on electrophoretic deposition (EPD) to deposit protective coatings on metallic interconnects. Deposition by EPD is a low-cost approach using a relatively simple apparatus. EPD provides good thickness control and allows for coating on substrates with complex shapes and makes mass manufacturing possible [47, 53, 54].

EPD suspensions are usually water based or organic based. Organic based suspension are prepared by mixing spinel powders with ethanol, acetone, and I_2 solution. H^+ ions were formed after the reaction between I_2 and acetone and adhered to the surface of spinel particles (Equation 4). This process makes the spinel particles positively charged [54, 55].

$$CH_3\text{-}CO\text{-}CH_3+2I_2=ICH_2\text{-}CO\text{-}CH_2I+2H^++2I^- \quad (4)$$

The mobility of charged particles depends on the dielectric constant of the suspension, the potential gradient between two electrodes, and the ($\boldsymbol{\zeta}$) potential around the particle. The mobility is also inversely proportional to the viscosity as shown by the Henry equation below:

$$\mu = \frac{v}{E} = \frac{2}{3}\frac{\varepsilon_0\,\varepsilon_r\zeta}{\eta} f(\kappa r) \quad (5)$$

In this equation, (v) is the velocity of particles moving under electric field (E), (ε_0) is the dielectric constant of vacuum, (ε_r) is the relative dielectric constant of the solvent, (η) is the solvent viscosity, $f(\kappa r)$ is the Henry coefficient [56, 57].

During the EPD process, the positively charged particles migrate toward to cathode electrode under the electric field. After that, the particles lose the charge and deposit on the substrate. Figure 7 shows a schematic of the EPD apparatus. The as-deposited layer is homogeneous but loose and porous, therefore a densification process is required which is usually a heat treatment.

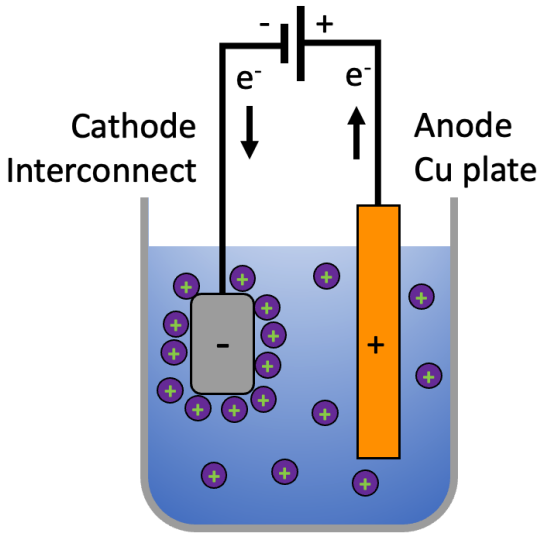

Figure 7. A schematic of the EPD apparatus.

Besides EPD, there are several other methods that can be used for protective layer deposition. These include electroplating (ELD) [53, 58], physical vapor deposition (PVD) [59, 60], chemical vapor deposition (CVD) [54, 61-63], pulsed laser deposition (PLD) [58, 64], sol-gel techniques [65-67] and screen printing [68]. ELD suspension is based on a solution of metal salts and the moving species are ions. However, it is time-consuming and hard to accurately control the coating composition. Moreover, the waste solution needs to be disposed properly. PVD deposition can deposit thin and uniformly on flat surfaces but not on surfaces with complex geometries. CVD can deposit coatings on complex shapes,

but needs significant process development which changes with coating composition changes. Both CVD and PVD need expensive equipment. Screen printing uses simple apparatus and can be inexpensive. However, it cannot be used to coat complex shapes, and it is difficult to deposit thin coatings uniformly. Thus, EPD is an optimal method for depositing protective coatings on SOFC interconnects [69].

1.8.2 Material selection for protective coatings on SOFC interconnects

Protective coating materials for SOFC interconnects should have phase stability in oxidizing and reducing environments, matched CTE with interconnects, high electrical and thermal conductivity, and low oxygen and chromium diffusivity to limit TGO growth and Cr-volatilization, respectively [53, 69-71]. Petric and Ling studied the CTEs and electrical conductivities of different pure spinels. They concluded that the promising materials for coatings are Mn-Co spinels, Cu-Mn spinels, and Cu-Fe spinels [72]. Lots of works have been done to explore Mn-Co spinel coatings[73-77].

Brylewski optimized the Mn-Co spinel composition by testing samples with different Mn/Co ratios. The results showed that $MnCo_2O_4$ remained a cubic spinel over the entire temperature range of 100ºC–800ºC. The study showed that as the Mn/Co ratio increased, the electrical conductivity decreased, and the samples exhibited both tetragonal and cubic structures [78].

Wang et al. investigated Fe doped Mn-Co spinel. They found that the Cr diffusion rate at 900ºC decreased significantly with the Fe doping, leading to a better matched CTE than pure $MnCo_2O_4$ spinel. Without doping, $MnCo_2O_4$ has a CTE value of 10.8×10^{-6}/ºC, which is smaller than the CTE of ferritic stainless-steel (12×10^{-6}/ºC). By changing the ratio

of Co/Fe, they found the optimal composition was $MnCo_{1.66}Fe_{0.34}O_4$, with a perfectly matched CTE value of 12×10^{-6}/ºC and conductivity at 65 S/cm [79].

Compared to Mn-Co based spinels, Cu-Mn based spinels are much cheaper and have higher electrical conductivity [72]. Cr diffusion profiles of $Cu_{1.3}Mn_{1.7}O_4$, $Cu_{1.2}Mn_{1.8}O_4$, and $CuMn_{1.8}O_4$ were analyzed by our group. $CuMn_{1.8}O_4$ exhibited the slightest weight gain and the smallest oxygen diffusivity among the three spinel compositions. However, undoped Cu-Mn spinel is not a pure phase at room temperature, and it is a mixture of spinel and Mn oxide. A CuO layer was also detected on the coating surface after densification [39, 40, 80].

Joshi et al. reported that adding Ni to the Cu-Mn spinel expands the stability region of the spinel while maintaining high conductivity. Another advantage is that doping Ni can reduce the CTE of the coating layer to prevent delamination [81]. Our group also examined the Cr retention ability of Ni-doped Cu-Mn spinel. This spinel was found to be a single phase at room temperature, and Cr diffused distance was shorter than the value for the undoped spinel sample, which indicates that doping of Ni decreases Cr diffusivity in the coating layer [81, 82].

.

2. Electrochemical cleaning: Demonstration of feasibility

2.1 Introduction

In this study, the feasibility of a novel method termed as 'electrochemical cleaning' was demonstrated. The *in-situ* process, based on the reversible operation of LSM-based cells, removes the chromium deposits from the cathode. Two cells were fabricated and tested; a poisoning baseline and a cell that was poisoned and then electrochemically cleaned. To demonstrate the effect of cleaning, both cells were exposed to Cr vapor species under identical SOFC working conditions, leading to degradation of cell performance. Electrochemical cleaning was then applied to one cell under SOEC conditions. Current-voltage (I-V) and electrochemical impedance spectroscopy (EIS) data were acquired were to evaluate cell performance. Microstructural characterization of poisoned and electrochemically cleaned cells was carried out using scanning electron microscopy (SEM) and energy dispersive x-ray spectroscopy (EDS). The results showed that after electrochemical cleaning, most of the Cr-containing deposits were removed compared to the poisoning baseline cell. This was accompanied by a significant recovery of cell performance as a result of electrochemical cleaning.

2.2. Experimental methods

2.2.1 Cell fabrication

In this research, button half cells were commercially purchased from SOFCMAN Energy (Ningbo, China). The half cells consisted of a 400 µm NiO-8YSZ (8 mol% Y_2O_3-

92 mol% ZrO_2) anode substrate, a 7 µm NiO-8YSZ anode active layer, and a 7 µm dense YSZ electrolyte. Cathode slurries were prepared before screen printing by mixing the desired cathode powders and then ball milling with alpha-terpineol (Alfa Aesar), carbon black pore former (Fisher Scientific), and binder (V6, Heraeus). A 1:1 weight ratio of $(La_{0.8}Sr_{0.2})_{0.9}MnO_{3-\delta}$ (Fuel Cell Material) and 8YSZ (Tosoh Corp) powders was used for the cathode active layer. Only LSM powder was used for the cathode current collector layer. The two layers, each 25 µm thick, were screen printed on the electrolyte and sintered separately at 1200°C for two hours[52, 83]. The diameters of the NiO-YSZ substrate and cathode were 3 cm and 1.6 cm, respectively (Figure 8).

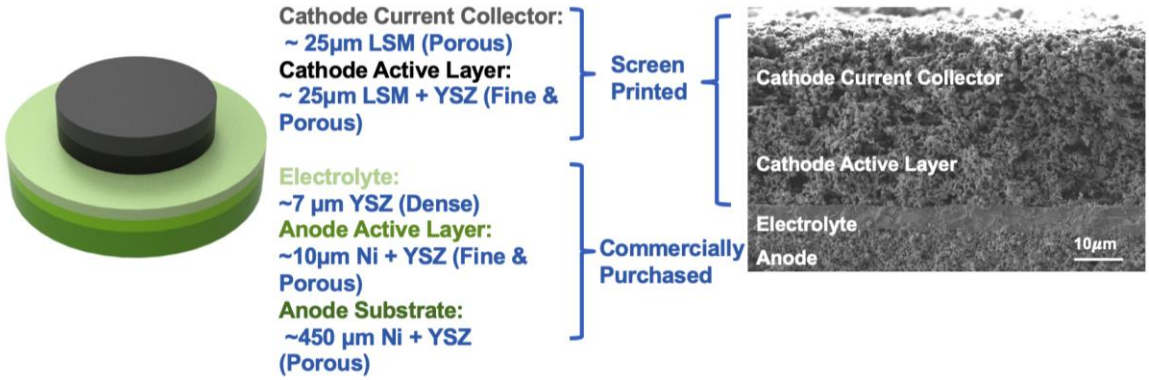

Figure 8. Schematic of the screen-printed cell structure (left). SEM micrograph of the screen-printed cell cross-section (right).

The fabricated cathodes were purposely designed with large grain sizes and high porosity to reduce the triple phase boundary length. With this specific microstructure, less deposited chromium is needed to have a large effect on cell performance as evidenced by I-V and EIS analyses. Thus, the changes in performance are enhanced in this study to elucidate performance changes with changes in the concentration of Cr-containing deposits

within the cathode.

2.2.2 Experimental set-up

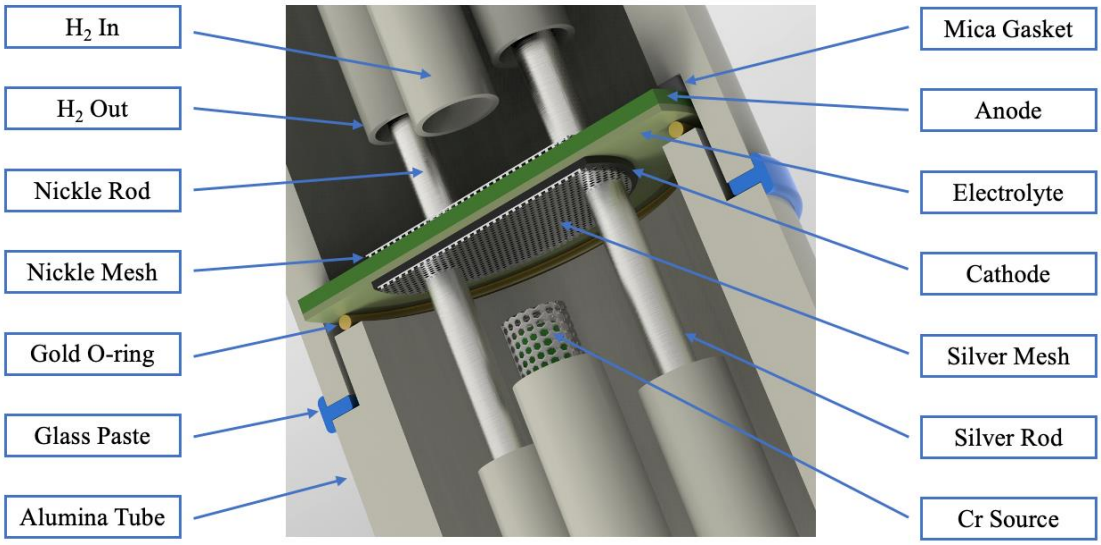

Figure 9. A schematic of the cell test setup.

Before loading the cell into the test stand (Figure 9), a silver mesh (Fuel Cell Materials) was attached using Ag paste on the air side of the cell, and nickel mesh (Alfa Aesar) was attached using Ni paste on the fuel side. Both served as current collectors. The cell was sandwiched between two alumina tubes, with a gold O-ring and mica gasket (Fuel Cell Materials) used as seals on either side. The outside of the tube was sealed with glass paste (Fuel Cell Store). Spring-loaded silver wire and nickel rods (Alfa Aesar) were used for electrical conduction. Small Cr_2O_3 pellets (Alfa Aesar) were wrapped inside a silver mesh (Alfa Aesar) and attached to the end of a retractable ceramic tube, which supplied humidified air during poisoning [35]. During the poisoning phase, the Cr_2O_3 bundle was

positioned ~1 cm from the air electrode in the hot zone to facilitate Cr vaporization.

2.2.3 Cell testing details

All cell testing was conducted at 800°C. For cell stabilization, a fuel gas mixture of 98% H_2 – 2% H_2O was supplied to the cell at a flow rate of 300 cm^3/min by bubbling pure hydrogen through a water bath at room temperature, establishing a low fuel utilization condition. Dry air was supplied at 1,000 cm^3/min by passing compressed air through a desiccant, which also established a low oxygen utilization condition. Both cells were first stabilized for 48 hours using 0.5 A/cm^2 applied current density.

During the Cr-poisoning phase, the air humidity was increased to 5% to increase the rate of Cr vaporization and thus deposition onto the cathode. This was accomplished by bubbling air through a water bath maintained at 33°C. The Cr source was introduced into the air flow. The cells were exposed to Cr vapors for 120 hours under 0.5 A/cm^2 current density. The Cr source was then removed from the air flow. The poisoning baseline cell was cooled down at this point.

The other poisoned cell was electrochemically cleaned for two hours under a mild electrolytic current of 0.15 A/cm^2. 10% humidified air on the air side and 10% humidified H_2 on the fuel side were supplied to the cell by passing each gas stream through their respective water baths maintained at 46°C. The fuel humidity was chosen to allow for a higher electrolytic current without polarizing the cell. High electrolytic cell polarization conditions can result in cell degradation causing void formation in YSZ grain boundaries and delamination of the air electrode [84]. Figure 2 demonstrates the significant impact low fuel humidity has on cell polarization in the SOEC mode, i.e. negative current regime.

Hydrogen with 10% water vapor was chosen to limit cell polarization in the SOEC mode. Based on Figure 10, the electrochemical cleaning condition was chosen to be 10% fuel humidity with an electrolytic current density of 0.15 A/cm^2 (marked by X in Figure 10). This limited the overpotential to 0.075 V for a Cr-free cell. Chromium deposition causes an increase in the various polarizations across the cell. Therefore, the measured voltage under these conditions of a poisoned cell, i.e., during the cleaning phase in this study, is much higher. However, as is discussed below, cell degradation as a result of operating the cell in SOEC mode was not observed under the conditions used in this study.

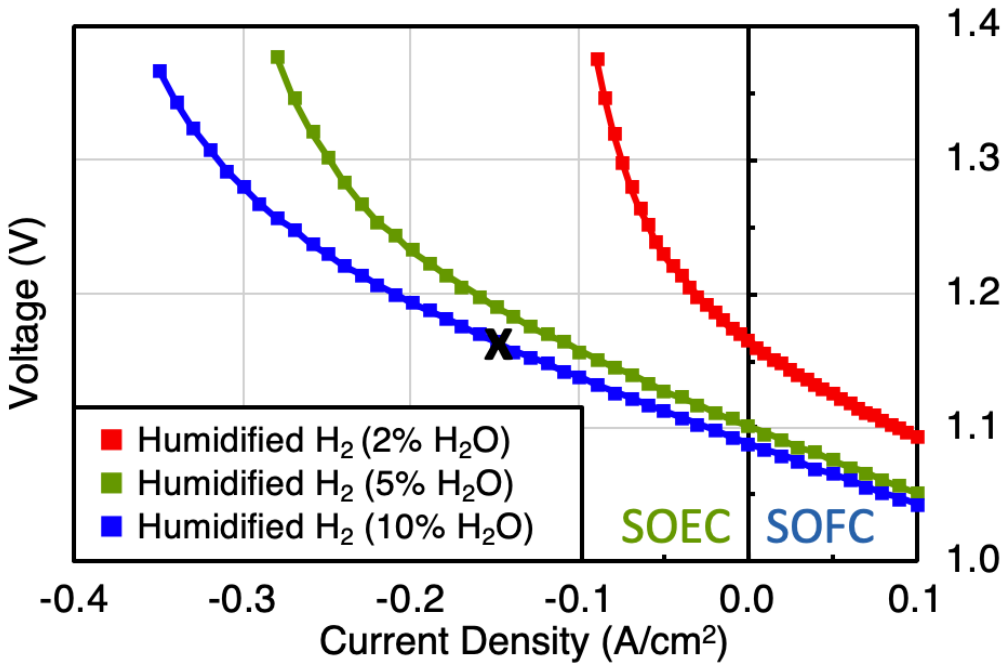

Figure 10. I-V curves for the cell operated at 800°C under varying fuel humidity values at the fuel electrode and dry air at the air electrode. The condition used in this study is marked as X. Positive current corresponds to the SOFC mode and negative current to electrolytic mode.

Current-voltage (I-V) and electrochemical impedance spectroscopy (EIS) measurements were acquired between each test phase to quantify changes in cell performance. All measurements were acquired at 800°C, under dry air (air side) and 2% humidified hydrogen (fuel side). Adequate time (~1 hour) was given before each I-V and EIS measurement to ensure cell equilibration. Electrochemical measurements were conducted using a Princeton Applied Research 263A PARSTAT®, KEPCO COP 20-20M power amplifier, and a Solartron SI 1250 frequency response analyzer.

Fractured samples were examined under the SEM to observe the microstructure of Cr-containing deposits after poisoning and after electrochemical cleaning. Samples were also mounted in cross-section in epoxy and polished for quantitative analysis of the Cr concentration profile across the cathode. After sputter coating both types of samples with carbon, samples were examined using scanning electron microscopy (Zeiss Supra 55 VP) and energy dispersive spectroscopy (EDS, Oxford Instruments, High Wycombe, UK). The acquired EDS spectra were analyzed using AZtec software (Oxford Instruments, High Wycombe, UK).

2.3 Results and Discussion

Figure 11a shows the changes in performance for the poisoning baseline cell. After stabilization, the maximum power density, used as an indicator of cell performance, was 0.753 W/cm^2. This dropped down to 0.403 W/cm^2 after 120 hours of Cr-poisoning, which constitutes a 46% drop in performance. Similarly, the cell that was electrochemically cleaned, started at a power density of 0.712 W/cm^2 after stabilization and dropped down to

0.428 W/cm^2, which is a 40% drop in performance (Figure 11b). After electrochemical cleaning, the maximum power density increased to 0.617 W/cm^2. Compared to the stabilized cell before poisoning, application of these specific electrochemical cleaning conditions for two hours resulted in a 67% recovery in cell performance.

Previous studies have shown that Cr-containing deposits form at the triple phase boundaries between the pore (gas phase), YSZ, and LSM phases near the cathode/electrolyte interface. The Cr-rich deposits block the electrochemically active sites, increasing the cathodic activation polarization. Also, the solid Cr-containing deposits reduce pore volume, increasing cathodic concentration polarization [85]. Both mechanisms lower cell performance. The recovery in the I-V curve as a result of cleaning demonstrates the removal of Cr-containing deposits from the TPBs, reversing the two deleterious mechanisms of chromium poisoning.

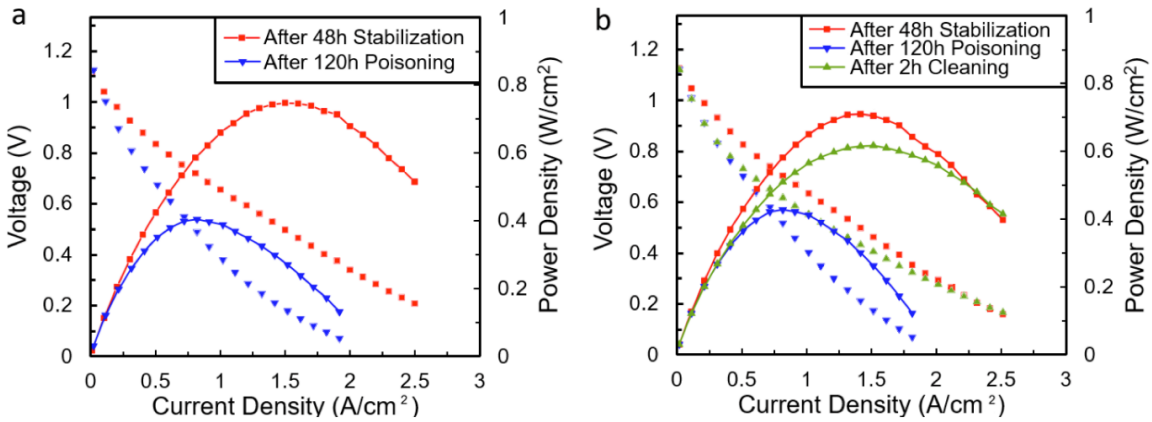

Figure 11. Current voltage curves for the (a) poisoned baseline cell, and the (b) electrochemically cleaned cell. Measurements were obtained at 800°C under dry air (air side) and 2% humidified H_2 (fuel side).

Figure 12a and Figure 12b show the impedance spectra for the two cells measured under open-circuit condition. The high frequency intercept on the real (x) axis provides the

ohmic resistance (R_Ω) of the cell, interconnects, and lead wires, while the low frequency intercept corresponds to the total resistance including the ohmic resistance as well as the polarization resistance (R_P). Thus, R_P is the difference between the two intercepts and includes the activation and concentration polarization resistances of the cell.

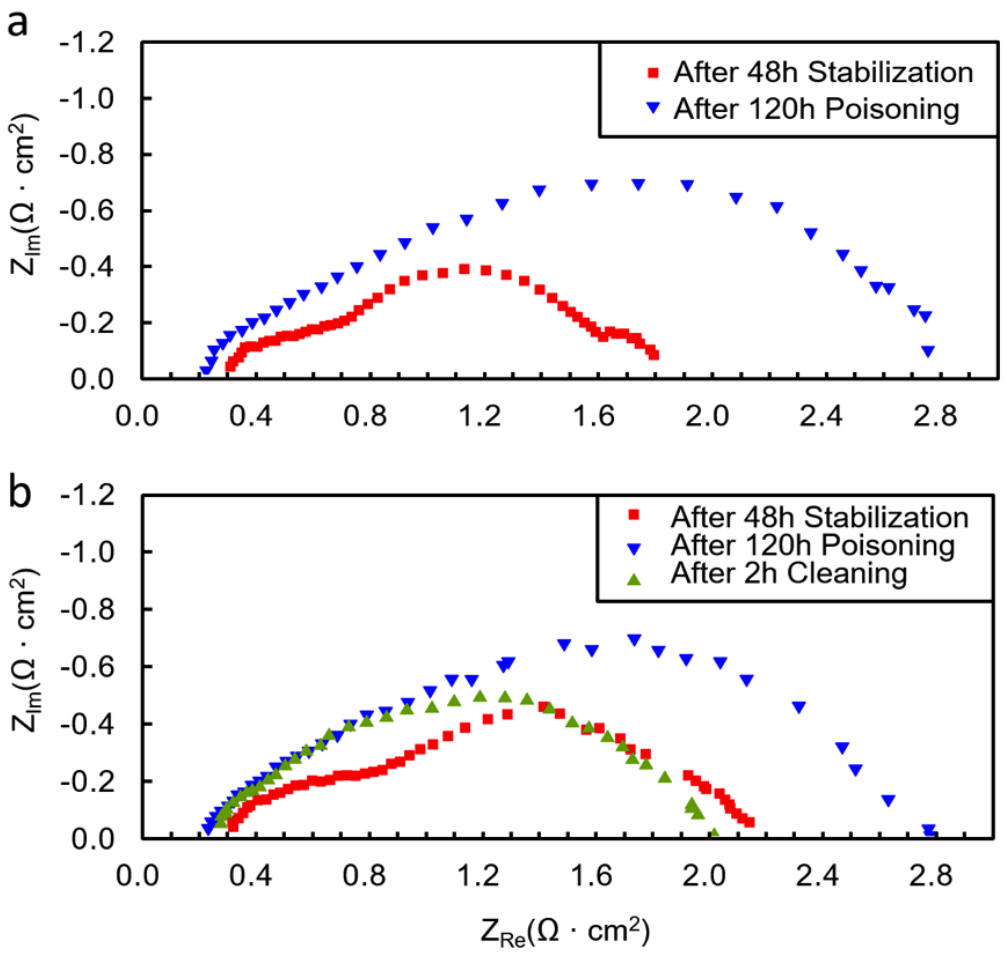

Figure 12. EIS curves for the (a) poisoned baseline cell and (b) electrochemically cleaned cell. Measurements were taken at 800°C under dry air (air side) and 2% humidified H_2 (fuel side) under open circuit condition.

The ohmic resistance of the cell decreases slightly over the course of cell operation, which is expected. It has been observed by several researchers that the ohmic resistance of the cell can continue to decrease for many hours under cathodic polarization even in the

presence of a chromium source [86, 87]. This trend has been attributed to improved contact resistance between the various cell components. The changes in polarization resistance however mirror the changes observed in the maximum power density. For both cells, R_P increased after poisoning, and for the cell that was electrochemically cleaned, R_P decreased after cleaning. The increase in R_P is commonly observed as a result of poisoning and results from Cr deposits blocking electrochemically active sites and thus hindering the oxygen reduction reaction [49, 52, 85, 87]. Therefore, the subsequent decrease in R_P as a result of cleaning demonstrates the reversal of performance degradation by freeing the electrochemically active sites. Both I-V and EIS results corroborate the improvement in cell performance due to electrochemical cleaning of the poisoned cell.

SEM-based EDS analyses were conducted on the two cells after electrochemical testing to determine the amount of Cr-containing deposits present in each cell and to determine the nature of the Cr-containing deposits. Figure 13a and Figure 13b shows SEM micrographs of an untested cell. Here, the YSZ electrolyte surface and LSM/YSZ grains in the cathode are clean and devoid of any deposits. In comparison, the poisoned baseline cell, shown in Figure 13c, show that the electrolyte surface at the electrolyte/cathode interface was covered with many small, rounded deposits as well as larger, faceted deposits. The larger deposits (see region marked as 1 in Figure 13c) ranged from 100–200 nm in size, while the smaller deposits (see region marked as 2 in Figure 13c) ranged from 20-50 nm in size.

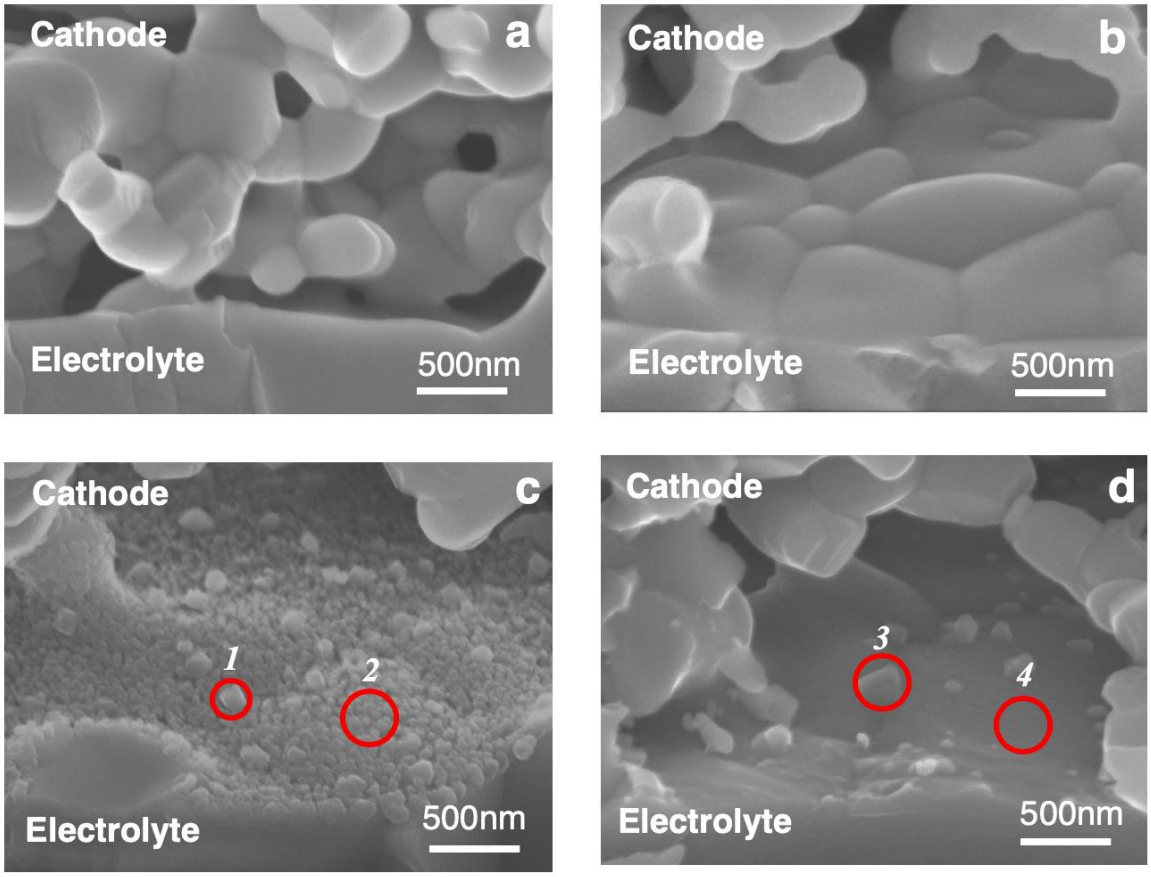

Figure 13. SEM micrograph of cathode/electrolyte interface for an untested cell with the sample holder a) with no tilt and b) tilted at 30º. The interface is clean with no deposits observed. SEM micrograph of the electrolyte surface in the (c) poisoned baseline cell, with large and small deposits visible in regions marked as 1 and 2. SEM micrograph of the electrolyte surface in the (d) electrochemically cleaned cell, showing that the larger faceted deposits remain (region marked as 3) and the finer deposits are no longer present (region marked as 4). For micrographs (c) and (d), the sample holder is tilted at 30º.

EDS spectra from Region 1 (large faceted deposit) and 2 (small rounded deposits) of the poisoned baseline cell (Figure 13c) are shown in red in Figure 14a and Figure 14b, respectively. We cannot directly compare the measured intensities of either Cr peak (at ~5.4 keV and ~5.9 keV) since the background LSM grains contribute to the 5.4 peak as La$L\beta_2$ and to the 5.9 peak as Mn$K\alpha$. Instead, the ratios between peaks can be used to compare Cr

as well as Mn content in the deposits [88, 89]. Since the La$L\alpha$ peak in the spectra (at ~4.65 keV) can only come from nearby LSM grains in the cathode, an EDS spectrum from an LSM grain in the clean untested cell can be used as a reference. The reference LSM spectrum is shown in blue in all four plots in Figure 14. All spectra from the deposits are scaled with the reference spectrum such that the La$L\alpha$ peak intensity of the deposit spectrum is the same as that from the LSM reference spectrum. The ratio of La$L\beta_2$/La$L\alpha$ peak intensities is fixed for pure LSM. Thus, the relative intensity ratio, (Cr$K\alpha$ +La$L\beta_2$)/La$L\alpha$, can be used as an indicator for Cr concentration, and the ratio, Mn$K\beta$/La$L\alpha$ can be used as an indicator for Mn concentration, in the deposits. In other words, in the scaled deposit spectra (shown in red), elevation of the peak at ~5.4 keV relative to the peak at ~ 4.65 keV is indicative of the presence of Cr in the deposits. An increase in the intensity of the peak at ~6.5 keV relative to the peak at ~ 4.65 keV is indicative of the presence of Mn in the deposits.

The EDS spectrum (Figure 14a) from the larger, faceted deposits (Region 1 in Figure 13c) shows a relative elevation of both peaks (at ~ 5.4 keV and ~6.5 keV), indicating that the faceted deposit is rich in Cr and Mn. Thus, the larger, faceted deposits have been identified as (Cr,Mn) spinel. The EDS spectra (Figure 14b) from the finer, rounded deposits (Region 2 in Figure 13c) shows a relative elevation of only the peak at ~ 5.4 keV, indicating that the rounded deposits are only rich in Cr. Thus, these finer, rounded deposits have been identified as Cr_2O_3. The observation of the two deposit types and their identification by composition as well as general morphology has been reported in many previous studies [26, 32, 33].

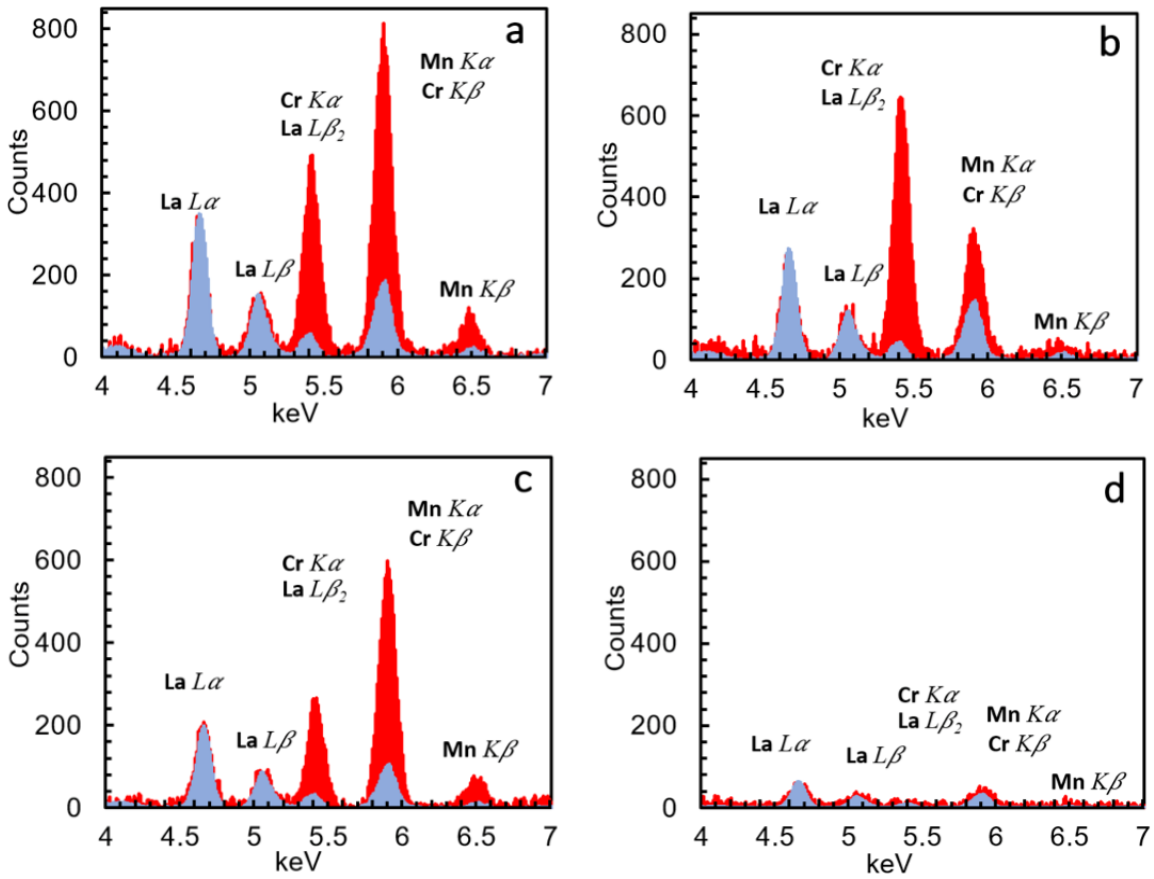

Figure 14. The red EDS spectra are taken from (a) a large, faceted deposit (Region 1 in Figure 13c) and from (b) a region with many fine, rounded deposits (Region 2 in Figure 13c) in the poisoned baseline cell. The red EDS spectra are taken from (c) a large, faceted deposit (Region 3 in Figure 13d) and from (d) a region without deposits (Region 4 in Figure 13d) on the electrolyte surface in the electrochemically cleaned cell. All spectra are scaled to the blue reference spectrum for pure LSM.

The effect of electrochemical cleaning is clear when comparing the SEM micrographs of the poisoned baseline and the electrochemically cleaned cells (Figure 13c and Figure 13d). Figure 13d shows that a majority of the deposits were removed from the electrolyte surface as a result of electrochemical cleaning. The EDS spectrum from a clean region (Region 4 in Fig. Figure 13d) is shown in Figure 14d. The spectrum shows there is no Cr or Mn enhancement, indicating that the deposits were completely removed from

these regions by electrochemical cleaning. The SEM micrograph of the electrochemically cleaned cell (Figure 13d) also shows that the large, faceted deposits still remain on the electrolyte surface (Region 3). Figure 14c shows an EDS spectrum from the large faceted deposit in Region 3, showing the faceted deposit to be (Cr,Mn) spinel. Furthermore, SEM images demonstrate that the mild electrolytic bias applied was sufficient to remove Cr deposits, while avoiding delamination between the electrolyte and air electrode, a common failure mechanism for SOECs.

The electrochemical cleaning process almost completely removes the Cr_2O_3 deposits, but leaves the (Cr,Mn) spinel deposits behind. This can be partially explained by the difference in vaporization kinetics between the two deposit types. The Cr vapor species are more readily produced over pure Cr_2O_3 compared to (Cr,Mn) spinel. During transpiration tests conducted at 800°C under 2% humidified air, Stanislowski et al. found that chromium vaporized from $(Mn,Cr)_3O_4$ at 30% of the rate of vaporization from Cr_2O_3 [48]. Chromium removal from (Cr,Mn) spinel deposits is thus expected to be limited by the diffusion of Cr to the surface of the spinel deposit. Furthermore, chromium poisoning studies by Jiang et al. found that the formation of (Cr,Mn) spinel is due to its stability in SOFC operating conditions and is not electrochemical in nature [38].

The Cr concentration profile was measured by EDS on polished cross-sections of the poisoned baseline and the electrochemically cleaned cells. Figure 15 shows the change in the Cr concentration (normalized to La) across the cathode thickness after poisoning (baseline) and after electrochemical cleaning. The (atomic %) ratio of Cr/La was determined at various depths in the cathode. Each value was averaged over 5 spectra, each

obtained from rectangular areas, 1.5 μm thick and 40 μm long, all at a given distance from the electrolyte/cathode interface. Figure 15 demonstrates a significant difference in the Cr concentration profiles between the two cells. Both cells demonstrate a higher Cr concentration closer to the electrolyte as expected for LSM/YSZ cathodes in the presence of chromium under cathodic polarization. However, the electrochemically cleaned cell demonstrates a significant decrease in the total amount of chromium compared to the poisoned baseline cell. At the cathode/electrolyte interface, where the Cr concentration is highest, the difference in Cr content between the poisoned baseline cell and the electrochemically cleaned cell is ~78%. Thus, under the conditions used, the electrochemical cleaning method is most effective on Cr_2O_3 deposits, which constitute the majority of the Cr deposition as qualitatively evidenced by Figure 13c, and quantitively by the decrease in total Cr concentration (Figure 15).

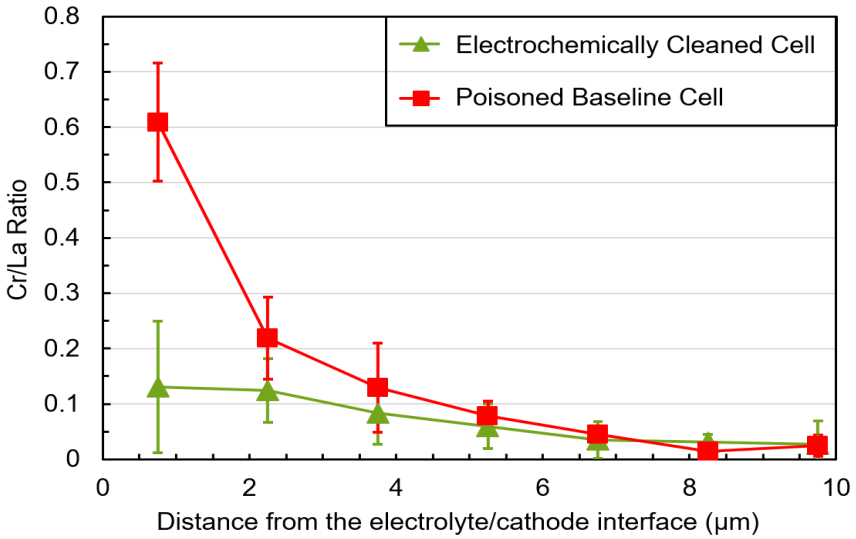

Figure 15. Plot of Cr/La (atomic%) ratio, quantified using EDS measurements, as a function of the distance from the electrolyte into the cathode.

Future studies will focus on optimizing the cleaning parameters. More aggressive electrolytic cleaning conditions may remove the (Cr,Mn) spinel deposits, but may also damage the cell. These issues will be explored for LSM based cells, as well as for cells with different cathode materials.

2.4 Conclusions

In this study, LSM based solid oxide fuel cells were fabricated and tested at 800°C. After poisoning with humidified air passing through Cr_2O_3, under cathodic current, performance degradation due to Cr-poisoning was observed. SEM and EDS analyses of the poisoned baseline cell revealed two types of Cr deposits: Cr_2O_3 and (Cr,Mn) spinel. The Cr_2O_3 deposits covered the entire YSZ electrolyte surface and extended several micrometers into the cathode. These deposits inhibited the ORR reaction and led to performance degradation of the cell in terms of a decrease in maximum power density and an increase in polarization resistance.

Electrochemical cleaning was implemented by operating the cell in the SOEC mode. A mild electrolytic cleaning condition was chosen to avoid irreversible damage to the cell. I-V and EIS analyses corroborated that chromium poisoning was reversed via electrochemical cleaning. Moreover, the electrochemically cleaned cell shows a relatively clean cathode/electrolyte interface, indicating that most of the Cr_2O_3 deposits were removed. This was accompanied by a significant recovery of the cell performance, i.e., an increase in the maximum power density and a reduction in the polarization resistance. Some deposits remained after cleaning and were identified to be (Cr,Mn) spinel, which are

difficult to remove by the electrochemical cleaning conditions used in this study. This research demonstrates, for the first time, the reversal of the chromium poisoning using an *in-situ* electrochemical cleaning process. It is anticipated that fuel cell stacks can be periodically run in electrolytic mode for 2 hours to substantially reverse the deleterious effects of chromium poisoning without having to cool the system down to room temperature.

3. Electrochemical cleaning: Multiple cycles

3.1 Introduction

As described in Chapter 2, the cell performance is recovered via the removal of Cr_2O_3 deposits by the electrochemical cleaning method. However, in order to provide an effective solution to long-term cell degradation due to chromium poisoning, electrochemical cleaning must be successfully applied many times over the lifetime of the cell, typically when the performance has degraded to a preset limit. Chapter 3 describes the results of the study of the efficacy of electrochemical cleaning as a repeatable Cr poisoning mitigation method for a cell subjected to accelerated poisoning conditions. This was accomplished by poisoning and cleaning a single cell a total of three times while tracking changes in cell performance using I-V measurements.

3.2 Experimental Methods

Three cells were tested in this study. They are designated as: poisoning baseline cell (Cell 1), multiple cycle poisoning-electrochemical cleaning cell (Cell 2), and an electrochemical reference cell (Cell 3).

The cell fabrication and testing setup are the same as we used in the last chapter. Cathodes were screen printed on half cells. Each cell consisted of 5 layers: a 25 μm thick LSM ($(La_{0.8}Sr_{0.2})_{0.9}MnO_{3-\delta}$) cathode current collect layer, a 25 μm thick LSM-8YSZ (8 mol% Y_2O_3-92 mol% ZrO_2) active layer with LSM/YSZ weight ratio of 1:1, a 7 μm thick, dense YSZ electrolyte, a 7 μm thick NiO-8YSZ anode active layer, and a 400 μm thick NiO-8YSZ anode substrate. For testing, a cell was placed between two alumina tubes, with

a gold O-ring on the air electrode side and a mica gasket on the fuel electrode side. For electrical conduction, a silver mesh and silver wires were used on the air side, and a nickel mesh and nickel rods were used on the fuel side. Glass paste was applied from the outside at the location the two tubes came together as a sealing material. Retractable Cr_2O_3 pellets served as the Cr source during the poisoning phases.

The experiment conditions for the poisoning and electrochemical cleaning are listed in Table 1. For the poisoning baseline (Cell 1), the fuel and air humidity were both set at 2%, which was achieved by bubbling gas through a water bath maintained at 18°C. After activating the cell for 48 hours at 800°C and 0.5 A/cm^2 current density, an I-V measurement was carried out. The Cr source was then introduced into the humidified air flow to form Cr-containing vapor species. This cell was then exposed to Cr-poisoning conditions for 25 hours at 800°C and 0.5 A/cm^2 current density. The Cr source was then removed from the air flow and an I-V measurement was carried out. The furnace was cooled down to room temperature.

Table 1. Experimental conditions for all cells at 800°C.

Procedure	**Air Electrode Humidity**	**Fuel Electrode Humidity**	**Current Density (A/cm^2)**	**Duration (hours)**
Activation	0%	2%	0.5	48
Poisoning	2%	2%	0.5	25
Electrochemical Cleaning	5%	10%	-0.15	2

Cell 2 (multiple cycle poisoning-electrochemical cleaning cell) was activated and poisoned under identical conditions as Cell 1, and I-V curves were generated after

activation and after poisoning. The cell was then electrochemically cleaned for two hours under a mild electrolytic current of -0.15 A/cm^2, with 5% humidified air (water bath set at 33°C) on the air side and 10% humidified H_2 (water bath set at 46°C) on the fuel side. The mild current and humidity on fuel side were chosen to limit the overpotential and avoid damaging of the cell [16]. The increase in the air humidity from 2% to 5% was used to increase the equilibrium vapor pressures of $CrO_2(OH)_2$, which is the most abundant Cr species in humidified air, from 1.1×10^{-10} MPa to 2.7×10^{-10} MPa. This in turn increases the driving force for vaporization of the Cr-containing deposits. The increase in fuel humidity (i.e. supply of oxygen for oxygen reduction reaction) from 2% to 10% was to avoid anodic polarization. An I-V curve was generated after the electrochemical cleaning. The poisoning and electrochemical cleaning processes were each repeated twice more without changing the temperature of the cell, for a total of three poisoning/electrochemical cleaning cycles at 800°C. The cell performances were characterized using I-V after every poisoning and cleaning step.

The role of Cell 3 (electrochemical reference cell) was to confirm that cell degradation was caused entirely by exposure to Cr-containing vapor species and that minimal damage was induced by running the cell in the SOEC mode during cleaning. After activation, Cell 3 was exposed to identical poisoning conditions as Cells 1 and 2 (2% humidified air and 0.5 A/cm^2 current density, for 25 hours at 800°C), but without the Cr source (referred hereon as SOFC exposure). The cell was then switched to the electrolytic (cleaning) mode for 2 hours (referred hereon as SOEC exposure). After the SOEC exposure, Cell 3 was held overnight for 12 hours at 800°C and 0.5 A/cm^2 current density

before being cooled to room temperature. Electrochemical I-V measurements were taken after each stage.

Current-voltage (I-V) and voltage-time (V-t) measurements were taken using a Princeton Applied Research 263A PARSTAT® with KEPCO COP 20-20M power amplifier. Electrochemical impedance spectroscopy measurements were taken using a Princeton Applied Research 2273 PARSTAT®. All measurements were taken at 800°C, with dry air on the air side and 2% humidified H_2 on the fuel side. The samples were allowed to equilibrate for one hour before the I-V curves were recorded.

After electrochemical tests, the microstructure of each sample was examined by scanning electron microscopy. The Cr-containing deposits were examined by fracturing the samples followed by SEM (Zeiss Supra 55 VP) observations. Polished cross-sectional samples were prepared for quantitative analysis of the Cr concentration using SEM and energy dispersive spectroscopy (Oxford Instruments, High Wycombe, UK). All samples were sputter coated with carbon to avoid charging under the electron beam.

3.3 Results and Discussion

Figure 16a shows the changes in the performance of Cell 1 (poisoning baseline cell) induced by the Cr-poisoning process. After activation, the maximum power density, used as an indicator of cell performance, was 0.89 W/cm^2, which dropped down to 0.79 W/cm^2 after 25 hours of poisoning, an 11% drop in performance due to Cr poisoning. Figure 16b shows the changes in performance for Cell 2 (multiple poisoning/cleaning cycle cell) after the first poisoning stage. After activation, the maximum power density was 0.78 W/cm^2.

This dropped down to 0.64 W/cm^2 after 25 hours of poisoning, which indicates 18% drop in performance. The differences in the performance drop between the two cells can be attributed to naturally occurring cell-to-cell variations.

Figure 16b also shows the performance of Cell 2 after the first cleaning cycle. The maximum power density of Cell 2 increased to 0.80 W/cm^2. The fact that the electrochemically cleaned cell exhibited better performance than before poisoning (but after activation) may be because some cell activation was still ongoing during the poisoning process. Figure 16c shows impedance changes during poisoning/cleaning cycle 1. The polarization resistance (R_p) is the difference between the high frequency intercept which provides the ohmic resistance (R_Ω) and the low frequency intercept which provides the total resistance. It clearly shows that R_p increased after poisoning and decreased after cleaning. Figure 16d shows the potential change during cleaning cycle 1. The current was kept constant during cleaning and the voltage drop confirms that the overpotential decreased during cleaning. Figure 16d suggests that significant portion of the cleaning occurs during the first 40 minutes of the cleaning cycle.

Figure 16c and Figure 16d show cell performances after the second and third poisoning/electrochemical cleaning cycles, respectively. In each case, the performance of the cell after the previous cleaning cycle is also shown. Both figures show drops in cell performance after poisoning, with significant recovery of the performance after electrochemical cleaning. This clearly indicates that the electrochemical cleaning process is repeatable.

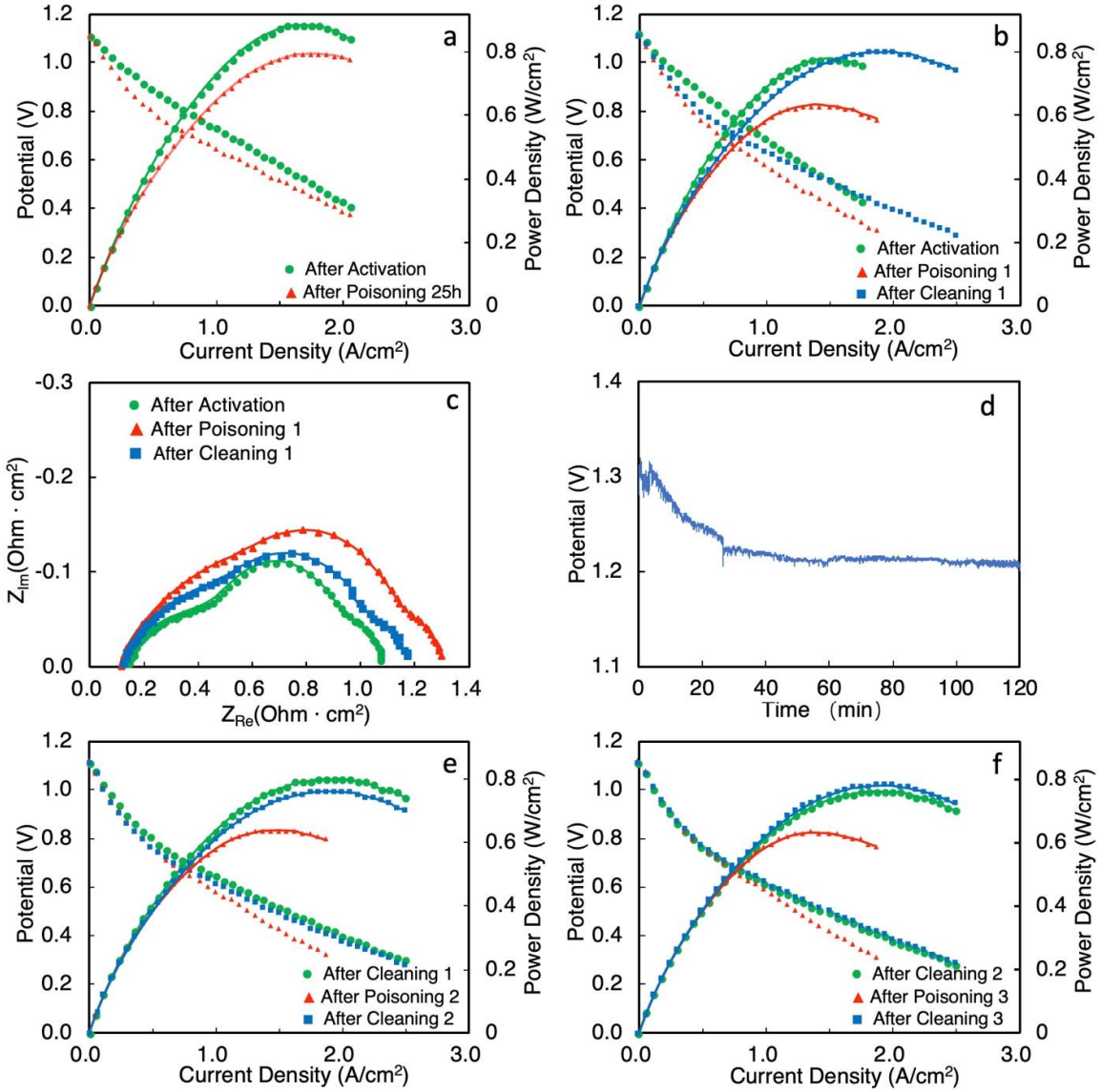

Figure 16. (a) I-V curves of Cell 1 after activation and after poisoning for 25 hours. (b) I-V curves for Cell 2 after the first poisoning/electrochemical cleaning cycle. (c) EIS curves for cell 2 during the first poisoning/electrochemical cleaning cycle. (d)Voltage versus time plot for cell 2 during the first electrochemical cleaning. (e) I-V curves for Cell 2 after the second poisoning/electrochemical cleaning cycle. (f) I-V curves for Cell 2 after the third poisoning/electrochemical cleaning cycle.

This supports the assertion that cells in SOFC stacks can be periodically electrochemically cleaned after Cr-poisoning without changing the stack temperature to

recover the original performance, thus reversing a major degradation mechanism of SOFC stacks over their lifetime.

The electrochemical reference cell (Cell 3) was activated under the same conditions as Cells 1 and 2. Then, emulating the poisoning stage, Cell 3 was exposed to 2% air humidity without the Cr source for 25 hours (SOFC exposure). As seen in Figure 17a, the maximum power density increased from 0.96 W/cm^2 after activation to 1.04 W/cm^2 after the SOFC exposure, which can be explained by continued cell activation. The difference in performance changes between the reference cell and the poisoned cells confirms that degradation in Cell 1 and Cell 2 during the poisoning stage were in fact due to chromium poisoning and not due to the SOFC exposure.

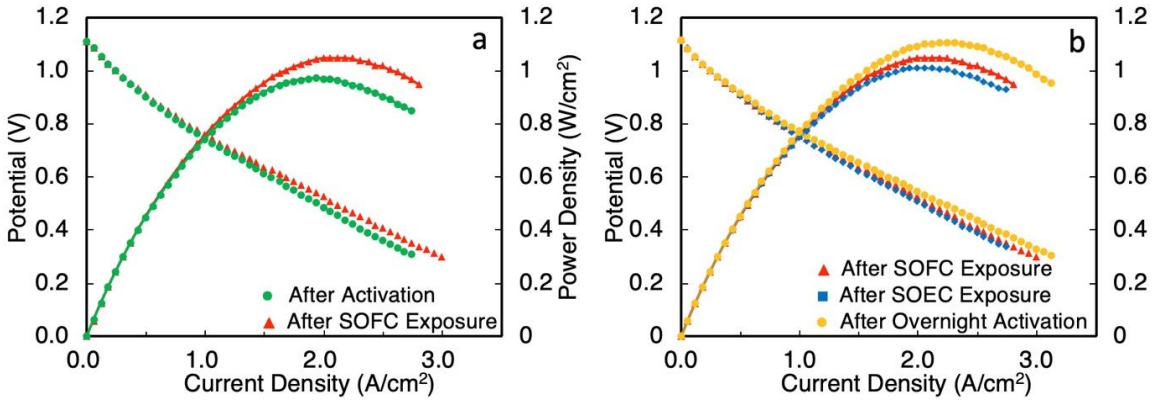

Figure 17. I-V curves for the electrochemical reference cell (Cell 3) (a) after activation and after SOFC exposure, and (b) after SOFC exposure, after SOEC exposure, and after overnight activation of 12 hours.

As seen in Figure 17b, after subjecting Cell 3 to identical electrolytic (electrochemical cleaning) conditions (SOEC exposure) after the SOFC exposure, the maximum power density decreased slightly. This confirms that the performance increase

in Cell 2 after every electrochemical cleaning was due to reversal of Cr-poisoning during the SOEC exposure, and not due to the SOEC exposure by itself. Interestingly, when Cell 3 was kept overnight for 12 hours under activation conditions following the SOEC exposure, the cell performance recovered and was better than before exposure to electrolytic conditions (Figure 17b). This implies that the performance loss due to operation in SOEC mode can be reversed by running the cell in SOFC mode. This phenomenon has been previously reported by Jiang and co-workers [17]. They reported that under anodic polarization (SOEC mode), 'deactivation' of the cell occurred due to a reduction in oxygen vacancy concentration at the cathode/electrolyte interface, which was charge compensated by partial oxidation of the Mn ions in LSM. Exposure to cathodic polarization (SOFC mode) re-activates the cell by increasing the oxygen vacancy concentration accompanied by partial reduction of Mn, thereby improving its performance.

Figure 18a shows a SEM micrograph of the cathode/electrolyte interface of Cell 1 after poisoning. The figure shows the cathode/electrolyte interface covered by deposits. In our previously published paper, we had identified two deposit morphologies; fine rounded deposits that were identified as Cr_2O_3 and larger faceted deposits that were identified as (Cr,Mn) spinels [16]. Figure 18a shows that almost all the Cr-containing deposits are fine rounded Cr_2O_3. This is confirmed by the EDS spectra shown in Figure 18c. The spectrum in red is taken from the region marked by a circle in Figure 18a. Since the $Cr_{K\alpha}$ and the $La_{L\beta 2}$ peaks overlap, this spectrum is superimposed with another spectrum (in blue) taken from an as-processed cathode which does not contain Cr. The $La_{L\alpha}$ peaks of both have been scaled to the same height. The significantly higher $Cr_{K\alpha}/La_{L\beta 2}$ peak in the red spectrum

indicated that the deposit has a high Cr content. The quantitative analysis methodology has been presented in detail in our earlier publication [16].

Figure 18a shows that virtually no larger faceted (Cr,Mn) spinel deposits were formed. This is in contrast with the results presented in our previously published paper, that shows a significant concentration of (Cr,Mn) spinel deposits in a cell poisoned under similar conditions, but with a higher air humidity of 5% and a longer duration of 120 hours. This suggests that the spinel phase forms later in time compared to the Cr_2O_3 phase, at least under the poisoning conditions used in this study. This observation is consistent with the formation mechanism of (Cr,Mn) spinel deposits as suggested by Krumpelt et al. [18]. They reported that under cathodic polarization, gas phase Cr species are reduced to Cr_2O_3 first. The (Cr,Mn) spinel phase forms when Cr_2O_3 reacts with MnO formed from the decomposition of LSM. Since it takes longer for MnO to be available from decomposition of LSM, Cr_2O_3 forms initially during poisoning, followed by the formation of the spinel phase.

Figure 18b shows a SEM micrograph of Cell 2 after three cycles of poisoning and cleaning. The interface appears to be relatively clean, with only a few clustered particles visible. EDS analysis (Figure 18d) showed that these deposits do not contain chromium since the Cr_{Ka}/La_{Lb2} peaks of the scaled red and blue spectra are identical. Due to the small size of the particles, it is difficult to confirm their exact composition using EDS. It is possible that they are a decomposed cathode electrode phase. Decomposition of LSM to form Mn_2O_3 during poisoning has been reported previously [19]. Figure 18b shows that running the cell under mildly electrolytic conditions can reverse the formation of Cr_2O_3

deposits, and that such an *in-situ* cleaning procedure can be repeated multiple times.

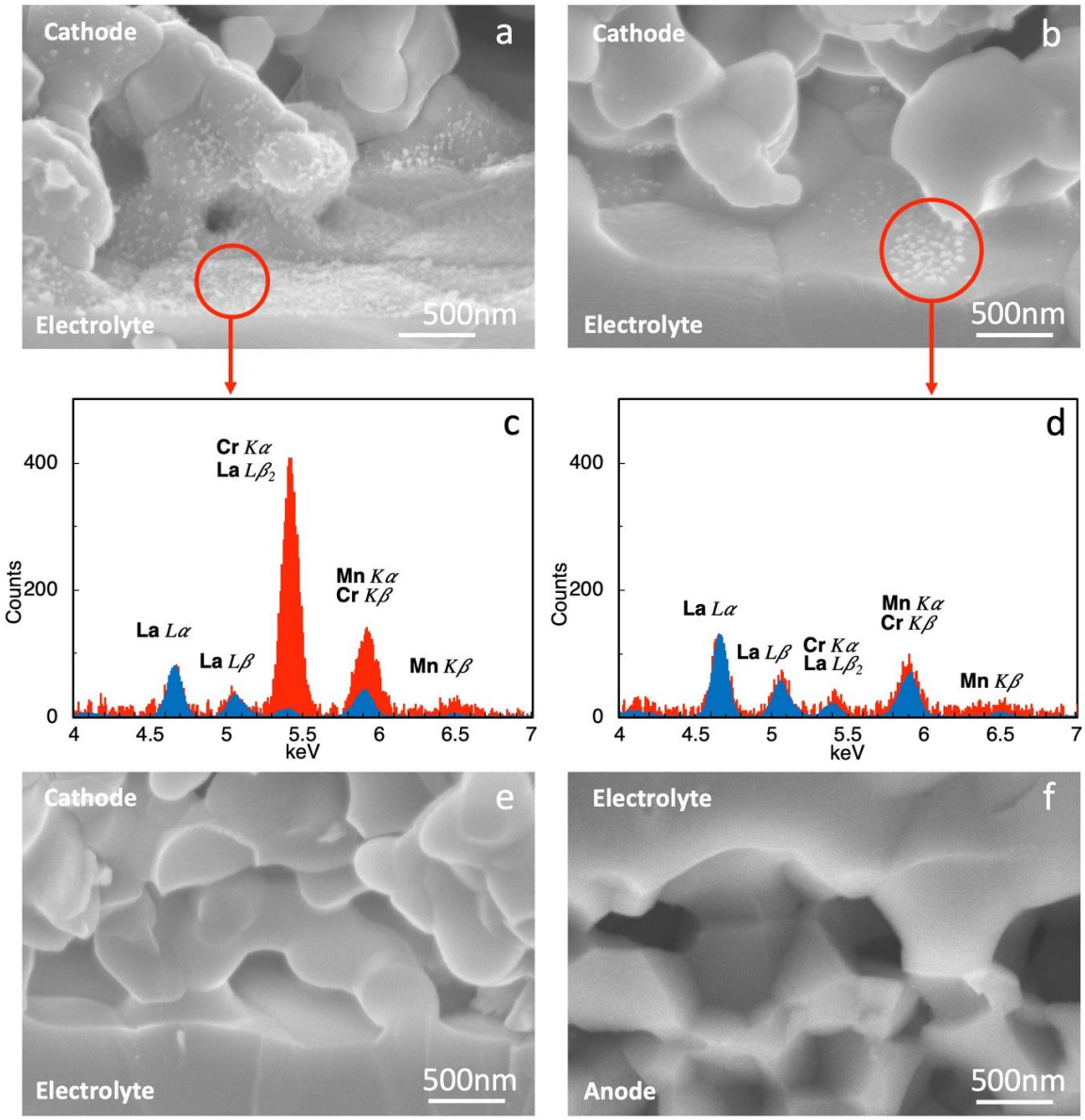

Figure 18. (a) SEM micrograph of the cathode/electrolyte interface of Cell 1 after Cr-poisoning. (b) SEM micrograph of the cathode/electrolyte interface of Cell 3 after three poisoning/electrochemical cleaning cycles. (c) EDS spectra from Cell 1 after poisoning, and (d) from Cell 3 after three poisoning/electrochemical cleaning cycles. The red EDS spectra were taken from regions marked in the SEM micrographs. All spectra are scaled to the blue reference spectrum from an as-processed LSM/YSZ cathode. SEM micrographs of Cell 3 at the (e) cathode/electrolyte interface and at the (f) anode/electrolyte interface.

Figure 18e and Figure 18f show that the cathode/electrolyte and anode/electrolyte interfaces, respectively, are clean and intact in Cell 3. No delamination was observed at either interface, which shows that the mild electrolytic condition used during electrochemical cleaning does not damage the cell microstructure.

It should be noted that the poisoning condition is quite severe in this study, with the Cr-source right in the path of the cathode inlet gas located close to the cathode surface. It is possible that under significantly more mild Cr-poisoning conditions that occur in actual operating SOFC systems due to the use of protective coatings and Cr-getters, the formation of (Cr,Mn) spinels might be delayed until much longer times. Thus, periodic *in-situ* electrochemical cleaning prior to (Cr,Mn) spinel formation may be a practical pathway to total Cr-containing deposit removal that i) does not damage the cell microstructure, and ii) does not need to occur too frequently during SOFC operation.

3.4 Conclusions

The poisoning baseline cell (Cell 1) showed significant Cr deposit formation. During 25 hours of poisoning, most of the deposits formed were Cr_2O_3. Since Cr_2O_3 can be effectively removed by electrochemical cleaning under mild SOEC conditions, as shown in chapter 2, a second cell was exposed to multiple (3) poisoning-cleaning cycles (Cell 2). It was found that a similar level of performance degradation and recovery occurred in each of the three individual cycles. After 3 cycles, the cell still maintained the initial power output level, and no damage due to electrolytic operation was found in the cell. A separate reference cell (Cell 3) tested without a Cr source and operated under similar SOEC

conditions shows that electrochemical cleaning did not damage the cell. This indicates that *in-situ* electrochemical cleaning under mild electrolytic conditions is an effective mitigation method, which can be repeatedly used to reverse the effects of Cr poisoning and thus, greatly extend the lifetime of SOFC systems.

4. Comparison of Cu-Mn and Mn-Co spinel coatings

4.1 Introduction

Protective coatings deposited by electrophoretic deposition has been attracting significant attention due to the low cost of the deposition apparatus, the ability to deposit uniform coatings on substrates with complex shapes, and the ease of operation for mass manufacturing. Mn-Co spinels and Cu-Mn spinels are widely used materials for protective coatings on SOFC interconnects due to their high electronic conductivities, matched CTE with the YSZ electrolyte, as well as low oxygen and chromium diffusivity. To choose the optimal coating material SOFC interconnects, it is necessary to have a comprehensive comparison of performance of Cu-Mn spinel and Mn-Co spinel coatings. Such a comparison was carried out by examining the performance of electrophoretically deposited undoped and doped Cu-Mn and Mn-Co spinel coatings under high temperature oxidation conditions.

In this study, $CuMn_2O_4$, $CuNi_{0.2}Mn_{1.8}O_4$, $MnCo_2O_4$, and $MnFe_{0.34}Co_{1.66}O_4$ spinel powders were fabricated and their phase stability, conductivity, and Cr gettering ability were measured. The powders were then deposited as coatings on flat SUS430 stainless steel substrates by EPD. A two-step densification method was then explored to form thin, uniform, protective coating layers. In order to evaluate the ability of the coatings to limit TGO (Cr_2O_3) growth under operating conditions, 100 h oxidation tests were carried out at 700°C and 800ºC in the dry air and humidified air. The microstructure changes, Cr concentration profiles and area specific resistance changes were tracked during the high temperature oxidation exposures.

4.2 Experimental methods

4.2.1 Spinel powder fabrication

Spinel powders of four different compositions, $CuMn_2O_4$, $CuNi_{0.2}Mn_{1.8}O_4$, $MnCo_2O_4$, and $MnFe_{0.34}Co_{1.66}O_4$, were fabricated by the glycine-nitrate combustion synthesis process (GNP) [90]. This method can manufacture finer and more homogeneous spinel powders than the traditional solid-state reaction method. The GNP process has been studied previously in our group [39, 40].

Proportional quantities of different nitrate hydrates and glycine were dissolved in deionized water. After stirring, a clear solution was formed. To evaporate excess water, the solution was transferred to a heavy-duty beaker with a thicker wall and heated on a hot plate in a chemical hood. After the solution changed to viscous gel, the hot plate was set to 500°C until the combustion reaction. Spinel powders were formed during the reaction. A fine stainless-steel mesh was applied on the top of the beaker to prevent ash ejection. To remove unreacted residuals, The resulting powders were calcined in a box furnace at 800°C in air condition for 2 h [39, 40]. Cu-Mn based spinel powders were dark brown in color, while Mn-Co based spinel powders were black in color.

4.2.2 Spinel bar samples fabrication and conductivity measurement

To better understand the relationship between conductivity and composition of all spinels, dense bar samples were fabricated from the powders. Spinel powders were compressed in a mold, sintered in a box furnace at 1000℃ for 20 h to get a dense body, and then held at 800℃ for 10 h to equilibrate the phase at the measurement temperature.

After sintering, electrical conductivities were measured as a function of temperature using a four-probe configuration as shown in Figure 19.

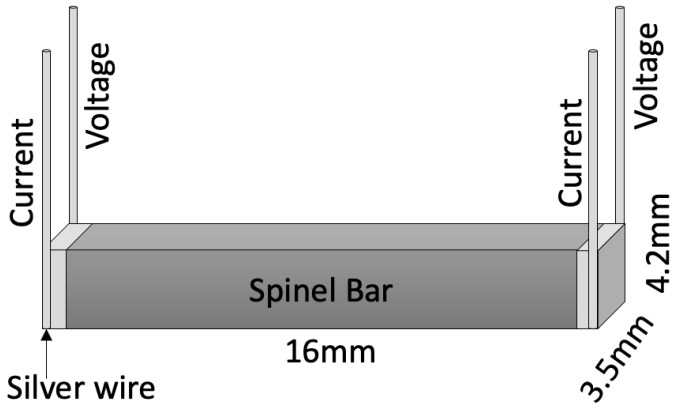

Figure 19. Conductivity measurements set-up for spinel bar.

4.2.3 The solubility limit of Cr_2O_3 in Cu-Mn and Mn-Co spinels

Previous results from our group showed that Cr can diffuse into the spinel layer while maintaining a cubic spinel structure, and there is a saturation limit before Cr_2O_3 precipitates out [40]. This Cr gettering ability for spinel coatings is important to avoid Cr diffusion to the coating surface where vapor-phase Cr species can be formed. The solubility limits of Cr_2O_3 in the four spinels were determined by mixing different molar ratios of spinel and Cr_2O_3 powders in ethanol. After ball milling, the powders were transferred into a box furnace and sintered at 800ºC. The resulting phases in the mixed powders were examined by x-ray diffraction (XRD, Bruker D2). Solubility limit for Cr_2O_3 is reached when separate Cr_2O_3 peaks can be seen in the x-ray diffraction scans.

4.2.4 Electrophoretic deposition and two-step densification

Since finer deposited particles lead to denser coatings, the sizes of spinel powders were reduced by ball milling. The powders were mixed with ethanol and 0.05 mm YSZ balls. Ball-milling was carried out using a ratio (ball/powder mass ratio) of 2:1 for 4 hours in a 30 ml milling bottle with 1.8g spinel powders, 3.6g YSZ milling balls and 15ml ethanol.

As an example, the microstructure of $CuNi_{0.2}Mn_{1.8}O_4$ powders before and after ball milling are shown in Figure 20. After milling, spinel powders were ~ 200 nm in size.

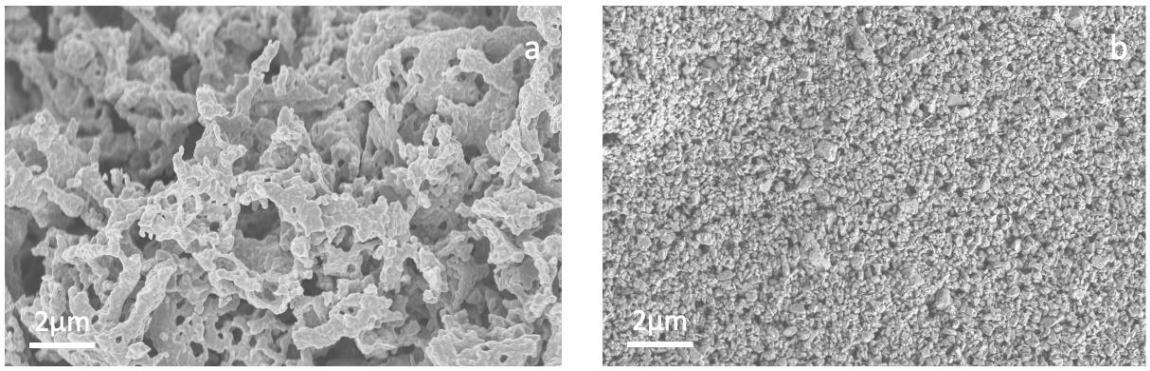

Figure 20. $CuNi_{0.2}Mn_{1.8}O_4$ spinel powder samples (a) before ball milling, and (b) after ball milling.

Usually, using smaller size YSZ milling balls results in the formation of finer spinel powders. We also prepared powders ball milled by 0.3mm, 0.1mm, 0.03mm and 0.015mm milling balls. Figure 21 shows a comparison of the powders milled using different sizes of YSZ milling balls. It shows that the spinel particle sizes were not reduced when using the smaller size YSZ milling balls.

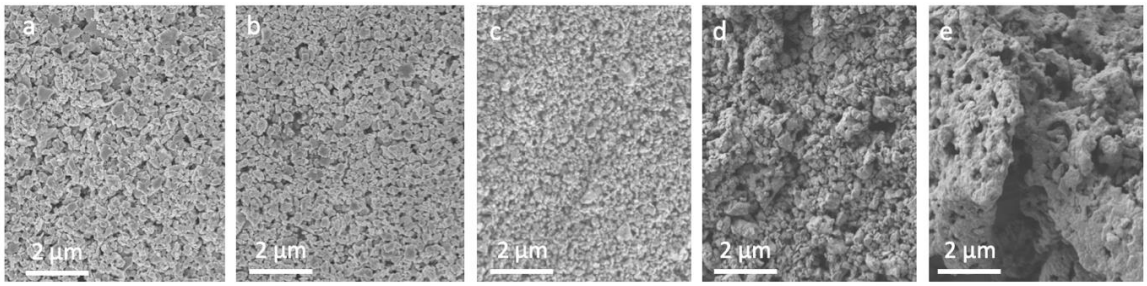

Figure 21. Spinel powders fabricated after ball-milling with (a) 0.3 mm YSZ balls, (b) 0.1mm YSZ balls, (c) 0.05 mm YSZ balls, (d) 0.03 mm YSZ balls, (e) 0.015 mm YSZ balls.

Figure 22 shows the microstructure of milled spinel powders before sieving the YSZ milling balls out. For the sample milled by 0.03mm YSZ balls (Figure 22a), there some large spinel particles remain. This is because the weight of YSZ balls is too small to break the larger spinel chunks. And this phenomenon becomes more obvious when using 0.015mm YSZ balls as shown in Figure 22b. The 0.05 YSZ milling balls worked best, and this milling ball size was used for all powder preparation experiments.

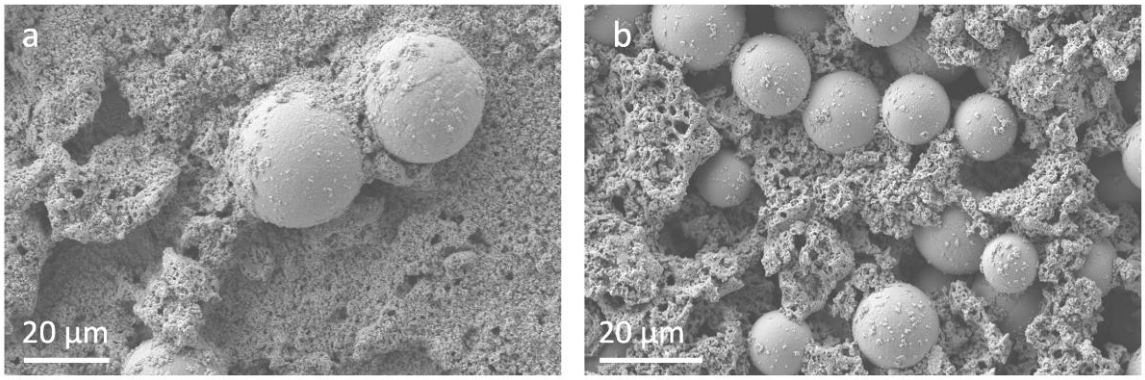

Figure 22. SEM images of spinel powders after ball-milling with (a) 0.03 mm YSZ balls, (b) 0.015 mm YSZ balls.

After 4 h of ball milling, all the YSZ balls were removed by sieving. EPD suspensions were prepared by mixing spinel powders with ethanol, acetone, and I_2 solution.

H^+ ions were formed after the reaction between I_2 and acetone and adhered to the surface of spinel particles. This process made the spinel particles positively charged. In this step, it is critical to keep the temperature of the solution low (< 25 °C) because I_2 evaporates very quickly. Therefore, ice was added to the water bath. Evaporation of I_2 can result in an insufficient number of charge carriers and thus a reduction in deposition rate or even failure of the deposition. The effect of the ratio of the weight of spinel powders to the weight of iodine can be found in a previous study in our group [56].

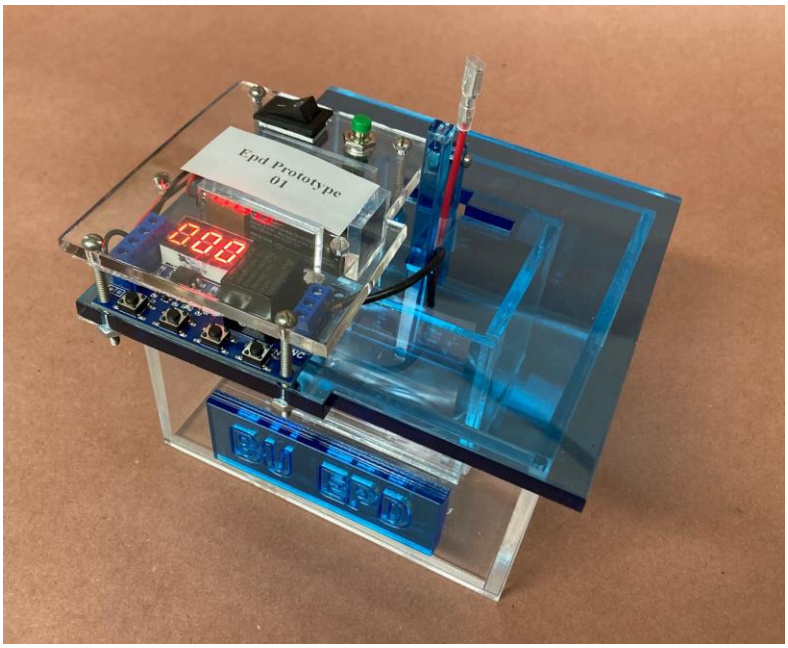

Figure 23. Prototype of EPD chamber for SOFC interconnect samples.

The prototype of the EPD chamber was designed and fabricated in our lab as shown in Figure 23. The blue tank cap is designed to hold the two electrodes and allows for changing the distance between the two electrodes. The fixed electrode holder with the black wire is for the copper plate, and the movable electrode holder with the red wire is for the

samples. A programmable timer was installed on the cap to control the deposition time. The bottom part of the apparatus is the spinel suspension tank which contains two separated areas. The inside area is for spinel suspensions, and the outside area is for chilled water/ice for temperature control.

SUS430 stainless steel interconnects were used as the cathode, with the anode being a Cu plate. The electrodes were immersed into a suspension of spinel powders. When a negative bias is applied to the interconnect, the positively charged spinel particles migrate to the interconnect due to electrostatic forces and are deposited on the sample surface. Different voltages were tested. It was found that if the voltage was smaller than 10 V, no coating layer formed on the substrate. If the voltage was too large, the deposition processed too fast, making thickness control difficult. An optimal voltage of 20V was applied for 5 minutes on the immersed electrodes. The experimental parameters used for the EPD process are listed in Table 2.

Table 2. EPD parameters used in this study

Ethanol (vol%)	**Acetone (vol%)**	**I_2 (mg/ml)**	**Spinel (mg/ml)**	**Voltage (V)**	**Electrode Spacing (cm)**	**Deposition Time (min)**
25	75	1.09	4.5	20	1.5	5

After deposition, the two-step heat treatment was applied for further densification [91]. This process consisted of a reduction anneal followed by a re-oxidation anneal as shown schematically in Figure 24. As-deposited Cu-Mn samples were reduced at 950°C for 6h, and Mn-Co samples were reduced at 900°C for 2 h. All the reductions were carried out in a pure H_2 environment to minimize the O_2 partial pressure. After the reduction

anneals, the sample was cooled down to room temperature and then re-oxidized in the air at 750°C for 24 h. A dense spinel coating layer was formed during the two-step densification process.

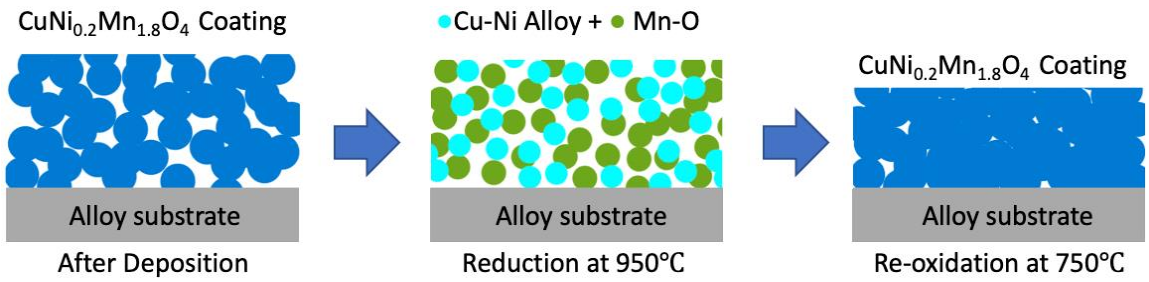

Figure 24. Schematic illustration of the microstructural development during the two-step sintering heat treatment.

4.2.5 Oxidation test for spinel coated samples

Oxidation tests were carried out for all as-densified samples at 700 °C and 800 °C for 100 h in air with 200ml/min flow rate. Silver mesh and paste were applied on both sides of samples, and ASR changes were tracked using a 4-quadrant power potentiostat (Zahner PP211) shown in Figure 25. As a reference, uncoated SUS430 substrates were also tested and compared in identical environments.

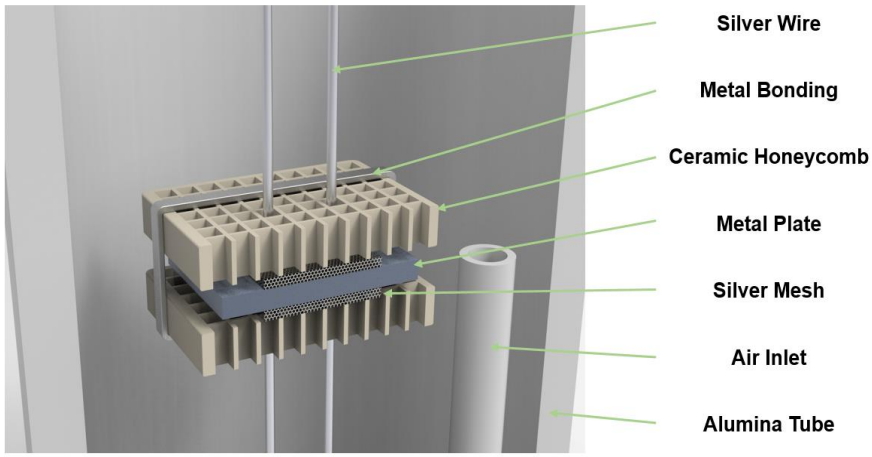

Figure 25. ASR measurements set-up during oxidation tests.

4.2.6 Characterization of spinel samples

The crystal structures of the spinel powders were analyzed by X-ray diffraction (XRD, Bruker D2 for room temperature) to study the phase purity of the powders. The coatings (as-deposited, after densification heat-treatment, and after testing) were mounted in epoxy and polished in cross-section. Sample surfaces and polished cross-sections were examined by scanning electron microscopy (SEM, Zeiss Supra 55 VP). Energy dispersive spectroscopy (EDS, Oxford Instruments) was used in mapping mode to analyze the composition distribution after reduction annealing, and in line-scan mode to analyze the Cr profiles changes during oxidation tests.

4.3 Results and Discussion

4.3.1 Phase stability

Figure 26 shows the XRD scans of spinel powder samples at room temperature. $CuNi_{0.2}Mn_{1.8}O_4$, $MnCo_2O_4$, and $MnFe_{0.34}Co_{1.66}O_4$ show standard cubic spinel peaks indicating that the powders were phase-pure. Besides the spinel peaks, $CuMn_2O_4$ also shows manganese oxide peaks (marked in red). These peaks could be indexed to Mn_3O_4, implying that the $CuMn_2O_4$ powder was a mixture of the spinel phase and manganese oxide phase. Based on phase diagrams, Cu-Mn based spinel has a much narrower single phase region as compared to Mn-Co spinel. The XRD data shows that Ni doping stabilized the Cu-Mn spinel composition and enlarges the single phase spinel zone.

Comparing the peak locations of undoped and doped spinels (i.e., $CuMn_2O_4$ versus $CuNi_{0.2}Mn_{1.8}O_4$, and $MnCo_2O_4$ versus $MnFe_{0.34}Co_{1.66}O_4$) in the XRD spectra, there is a

peak shift to the left after doping. This indicates that doping causes an increase in the lattice parameter of the spinel.

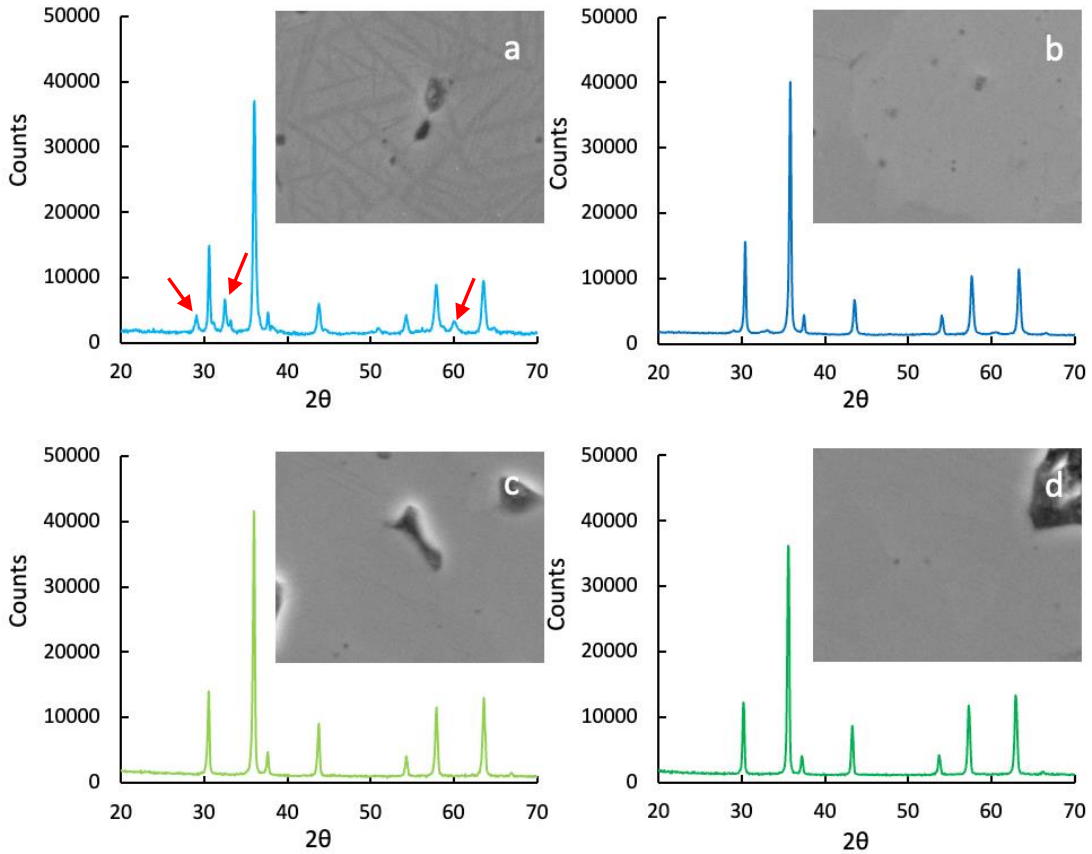

Figure 26. XRD scans of spinel powder samples and SEM images of polished bar samples of (a)$CuMn_2O_4$ (b)$CuNi_{0.2}Mn_{1.8}O_4$ (c) $MnCo_2O_4$ and (d)$MnFe_{0.34}Co_{1.66}O_4$ at room temperature. The red arrows indicate the presence of a second phase in $CuMn_2O_4$, which can be seen as needle like precipitates in the SEM micrograph in (a).

The SEM images in Figure 26 show micrographs of the polished cross-section of the four spinel bars. Only $CuMn_2O_4$ shows a two-phase microstructure with some needle-like phase seen clearly. The width of the needle-like structure is around 100-200nm. Previous TEM studies by our group showed that similar needle-like structures formed in $CuMn_{1.8}O_4$ coatings, and they were identified as Mn_3O_4, consistent with the XRD results.

The previous study showed that the Mn_3O_4 phase disappeared at 700°C and above, and the powders reverted to a phase-pure spinel [40].

4.3.2 Conductivity measurements

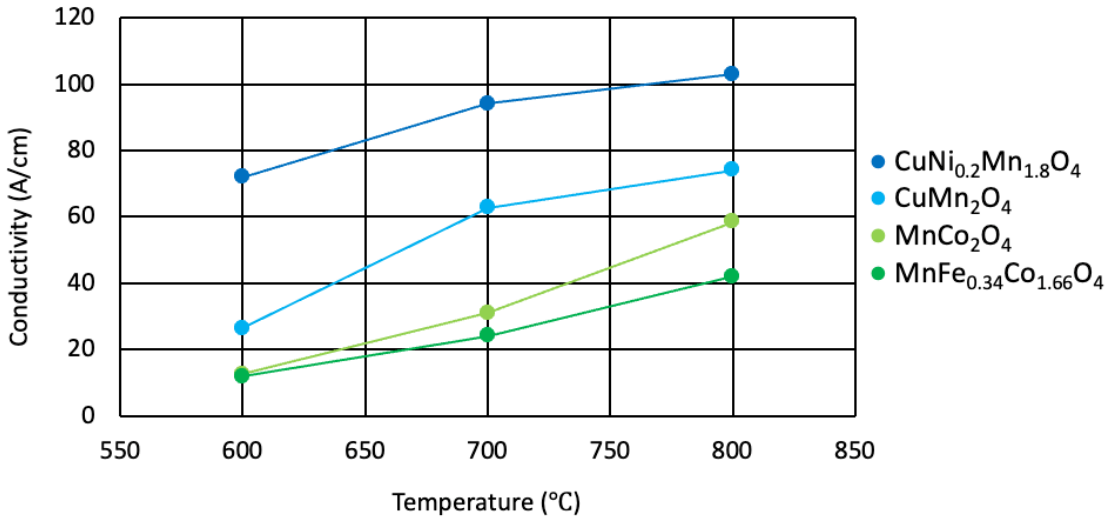

Figure 27. Conductivity of spinel bar samples as a function of temperature.

Figure 27 shows the measured conductivities of the four spinel bars. The data have been corrected for the measured porosity in the bars. It was found that Cu-Mn based spinels have higher conductivities than Mn-Co based spinels. As expected, all conductivities increased with increasing temperature. $CuNi_{0.2}Mn_{1.8}O_4$ has the highest conductivity from 600°C-800°C. At 700°C, Ni doping increased the conductivity of Cu-Mn spinel from 63 S/cm to 94 S/cm. Since the conductivity of the spinel phase in significantly larger than the manganese oxide phase, the increase of conductivity by Ni doping may be related to the lack of the manganese oxide phase [81]. In contrast, doping Fe decreased the conductivity of Mn-Co spinel from 31 S/cm to 24 S/cm. In Mn-Co spinel, Fe doping decreases the

concentration of Co^{3+}, leading to fewer available sites for small polaron hopping [76].

4.3.3 EPD coating and densification

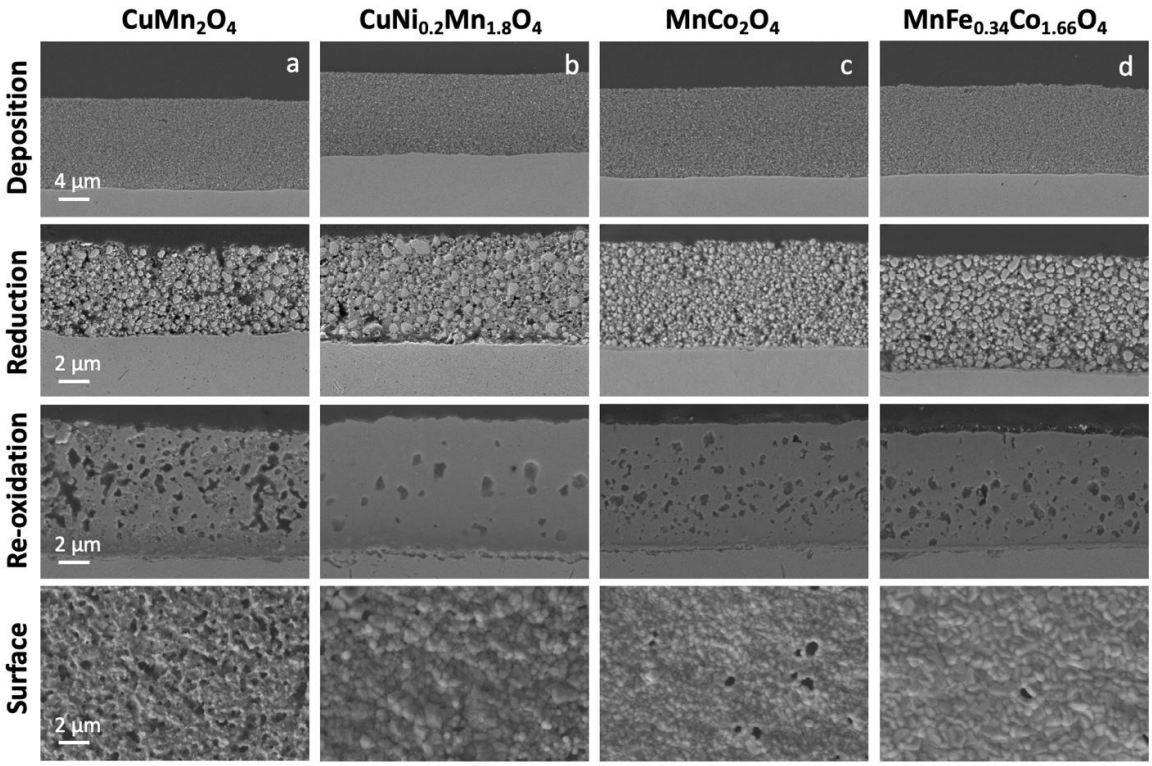

Figure 28. Microstructural changes during densification of (a)$CuMn_2O_4$ (b)$CuNi_{0.2}Mn_{1.8}O_4$ (c)$MnCo_2O_4$ and (d) $MnFe_{0.34}Co_{1.66}O_4$ coating samples. The top row shows the as-deposited microstructure, the second row shows the microstructure after the reduction anneal, the third row shows the microstructure after the re-oxidation anneal, and the bottom row shows the surface of the coatings after the reoxidation anneal.

After 5 min of EPD deposition, a ~16 µm spinel coating layer formed on the SUS430 substrates for all four powders. No appreciable differences in the four as-deposited samples can be seen in the top row of Figure 28. Figure 29 shows an example of the EDS elemental distribution maps for $CuNi_{0.2}Mn_{1.8}O_4$ after the reduction anneal. The figure shows an overlap of Cu and Ni maps, as well as Mn and O maps, indicating a two-phase

microstructure of a Cu-Ni alloy and MnO. Similarly, $CuMn_2O_4$ reduced to Cu metal and MnO, $MnCo_2O_4$ reduced to Co metal and MnO, and $MnFe_{0.34}Co_{1.66}O_4$ reduced to Fe-Co alloy and MnO. Also, the grain size for alloy phases appeared to be larger than pure metal phases, implying that doped spinels are easier to be reduced than undoped spinels.

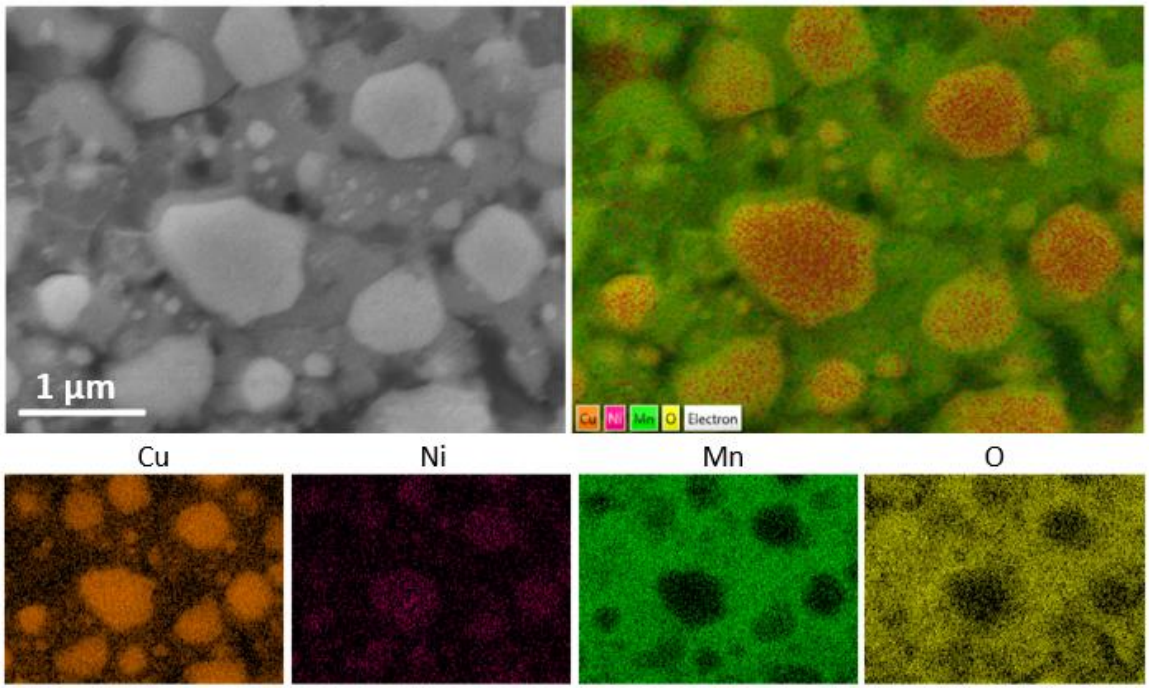

Figure 29. SEM image (top left) and EDS mapping of $CuNi_{0.2}Mn_{1.8}O_4$ sample after reduction. The top right image is the superposition of all the elemental dot maps.

After re-oxidation, ~10 µm dense spinel coatings re-formed on the substrates. It should be noted that there is a 0.6-0.7 µm TGO layer formed during the densification process. The $CuMn_2O_4$ spinel coating has a relatively large porosity as well as needle-like manganese oxide present in the densified layer. Compared to the undoped $CuMn_2O_4$ sample, the $CuNi_{0.2}Mn_{1.8}O_4$ spinel coating had a much smaller porosity. The undoped and Fe-doped Mn-Co based spinel coatings had similar microstructures, with the

$MnFe_{0.34}Co_{1.66}O_4$ coating being slightly less porous than the $MnCo_2O_4$ coating. The bottom images of Figure 28 show the surface microstructure of as-densified samples. The $CuMn_2O_4$ coating had the largest surface porosity, followed by $MnCo_2O_4$, while $CuNi_{0.2}Mn_{1.8}O_4$, and $MnFe_{0.34}Co_{1.66}O_4$ had the least surface porosity. Also, the spinel grain sizes for doped samples were found to be larger than the undoped samples. One possible reason for this may be that dopants increased the grain boundary energy, which is the major driving force for grain growth. Larger grain sizes lead to smaller grain boundary area/volume ratio. Larger grains may also be beneficial to limit Cr diffusion since grain boundary diffusion rate is typically much larger than bulk diffusion in grains.

4.3.4 Oxidation tests for spinel coated Samples

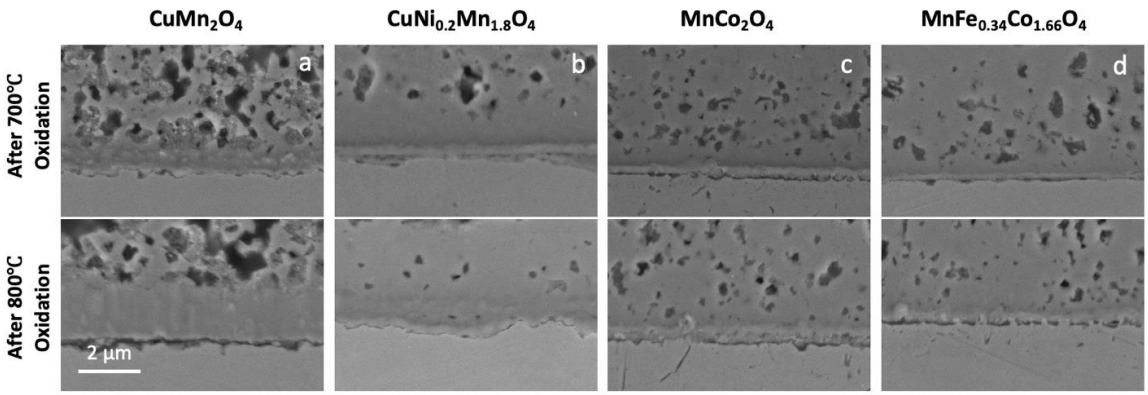

Figure 30. Cross-sectional SEM micrographs of (a) $CuMn_2O_4$, (b) $CuNi_{0.2}Mn_{1.8}O_4$, (c) $MnCo_2O_4$, and (d) $MnFe_{0.34}Co_{1.66}O_4$ samples after 100 h oxidation at 700°C (top row) and 800°C (bottom row).

To evaluate the effectiveness of EPD coatings in limiting further Cr_2O_3 growth, oxidation tests were carried out for $CuMn_2O_4$, $CuNi_{0.2}Mn_{1.8}O_4$, $MnCo_2O_4$, and $MnFe_{0.34}Co_{1.66}O_4$ coated samples. After the two-step densification, all the samples were

oxidized for 100 h at 700°C and 800°C under 200 ml/min airflow. SEM images of polished cross-sections and EDS line scans were taken after the oxidation tests. The top images in Figure 31 show the coating cross-sections after the 700°C oxidation anneal. To quantify the TGO growth, EDS lines scans of Cr of the coating cross-sections were obtained, as shown in Figure 31. The changes of peak width at half maximum were tracked. After densification, the thickness of the Cr rich layer for coating samples were well controlled under 1 µm. After the 700°C oxidation, the TGO thickness increased between 0.2-0.3 µm for all samples. The EDS line scan data at 700°C in Figure 31, shows a fairly significant Cr diffusion profile into the $CuMn_2O_4$ coating. However, it is difficult to conclude which of the other three spinel coatings, $CuNi_{0.2}Mn_{1.8}O_4$, $MnCo_2O_4$, or $MnFe_{0.34}Co_{1.66}O_4$, best limited Cr growth. To differentiate between these three coatings, oxidation at 800°C was carried out.

The bottom row of images in Figure 30 show SEM micrographs of the samples after the 800°C oxidation tests. Clear differences can be seen in the Cr profiles in the Cu-Mn and Mn-Co spinel samples (Figure 31). In the Cu-Mn spinel samples ($CuMn_2O_4$ and $CuNi_{0.2}Mn_{1.8}O_4$), the Cr profiles show a peak (~ 1 µm wide) at the coating/alloy interface, as well as a relatively flat region (~ 1 µm thick for $CuMn_2O_4$ and 0.2 µm for $CuNi_{0.2}Mn_{1.8}O_4$) in the coating to the left of the peak, before the Cr signal decays to zero in the outer part of the coating. This is different from the results seen after the 700°C test for 100h, where the flat portion of the Cr profile was absent. The Cr profile in the Mn-Co samples looks different where a thicker peak (~ 0.9 µm for $MnCo_2O_4$ and ~ 0.7 µm $MnFe_{0.34}Co_{1.66}O_4$) can be seen with a steeper decline to zero into the coating without the

presence of a flat region to the left of the peak.

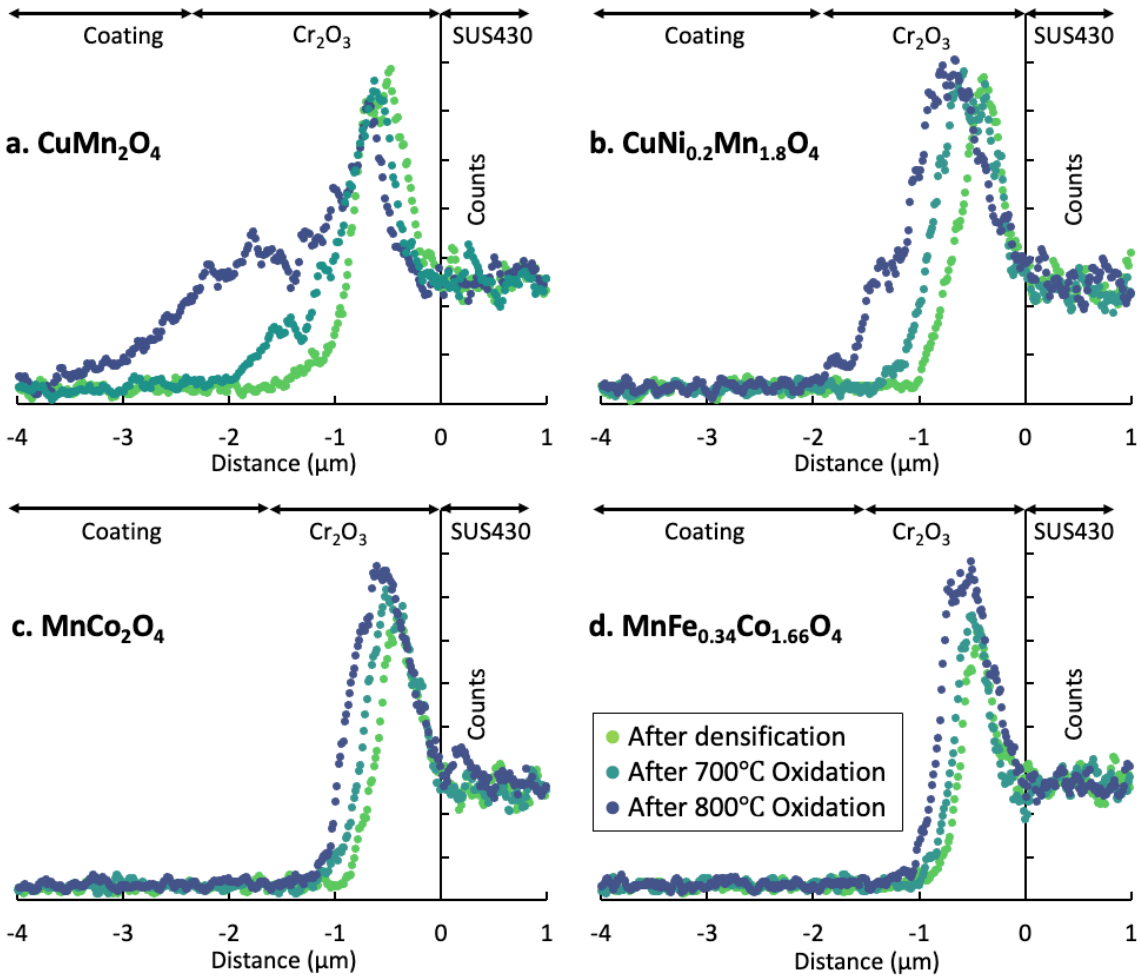

Figure 31. EDS line scans of Cr across (a) $CuMn_2O_4$, (b) $CuNi_{0.2}Mn_{1.8}O_4$, (c) $MnCo_2O_4$, and (d) $MnFe_{0.34}Co_{1.66}O_4$ samples after densification (light green), after 700°C oxidation (dark green), and 800°C oxidation (dark blue).

The peaks correspond to the thermally grown Cr_2O_3 at the coating/alloy interface. It should be noted that in the presence of the coating, it is the inward diffusion of oxygen through the coating that determines the growth rate of the TGO. In Figure 31a and Figure 31b, the flat Cr profile into the left of the peak indicates that saturation of Cr in that region of the coating has occurred. The Cr profile where the concentration decays to zero is a

measure of the Cr diffusion in the coating. It is interesting to note that the $CuNi_{0.2}Mn_{1.8}O_4$ spinel coating has a thinner peak, indicating that Cr diffusivity in this coating is smaller than in the $CuMn_2O_4$ spinel coating.

Within the Mn-Co spinels, the Cr diffusion profile to the left of the peak is steeper in the $MnFe_{0.34}Co_{1.66}O_4$ sample. This indicates that the Cr diffusivity in $MnFe_{0.34}Co_{1.66}O_4$ is smaller than $MnCo_2O_4$.

Based on the Cr profiles, Mn-Co based spinels show a better ability to limit TGO growth than the Cu-Mn based spinels. Also, doped spinels performed better than the undoped spinels in limiting TGO growth. As a reference, uncoated SUS430 formed a 1 µm thick TGO during 700°C oxidation test, and a 3 µm thick TGO during 800°C oxidation test as shown in Figure 32 and Figure 33.

Recently, improvements in ceramic processing have led to a decrease in the thickness of the electrolyte without compromising its effectiveness as a diffusion barrier by avoiding pinholes, this allows the operating temperatures of SOFCs to be in the intermediate temperature range of 600°C - 700°C. At these operating temperatures, all the spinels studied here, except $CuMn_2O_4$, will work well to limit TGO growth.

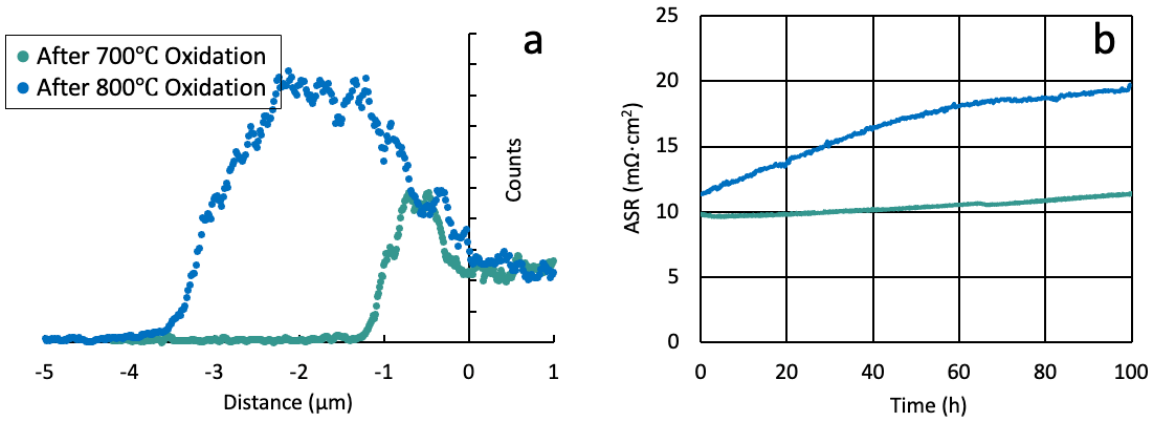

Figure 32. (a) Cr EDX line scans on uncoated SUS430 reference samples after 100h oxidation in flowing air at 700°C (dark green), and 800°C (dark blue). (b) ASR changes for uncoated SUS430 reference samples during the 700 ℃ (dark green) oxidation test and during the 800°C oxidation test (dark blue).

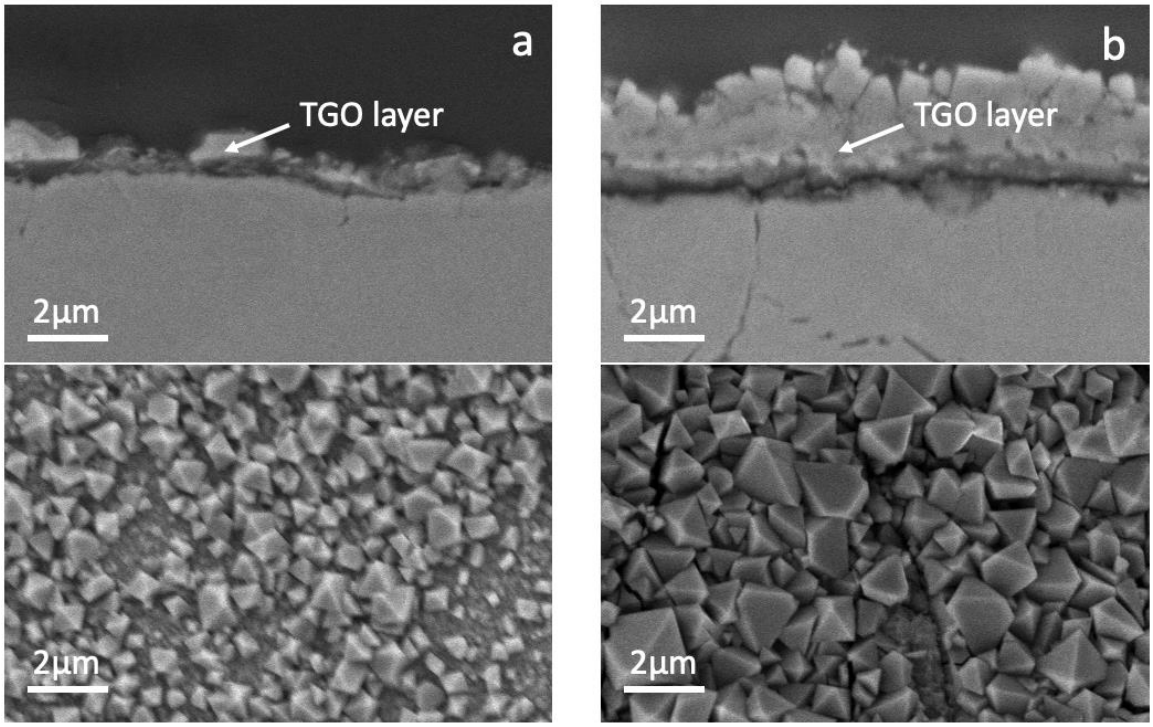

Figure 33. Cross-sectional microstructure (top) and surface microstructure (bottom) for uncoated SUS430 reference samples after 100h oxidation in flowing air at (a) 700°C and (b) 800°C.

4.3.5 ASR measurements for 800°C oxidation tests

Since there were almost no changes in ASR at 700°C for all samples, ASR changes during the 100 h exposure in flowing air at 800°C were tracked. Figure 34 shows that the ASR for the $CuNi_{0.2}Mn_{1.8}O_4$ coated sample increased by 0.2 mΩ·cm^2**,** making the coating the best in terms of ASR performance. The ASR for the $CuMn_2O_4$ coated sample increased by 1 mΩ·cm^2, the ASR for the $MnCo_2O_4$ coated sample increased by 0.9 mΩ·cm^2, while the ASR for the $MnFe_{0.34}Co_{1.66}O_4$ coated sample increased by 0.6 mΩ·cm^2. As a reference, ASR for uncoated SUS430 increased by 2 mΩ·cm^2 even at the lower temperature 700°C oxidation test and increased by 8 mΩ·cm^2 at 800°C oxidation test (Figure 32).

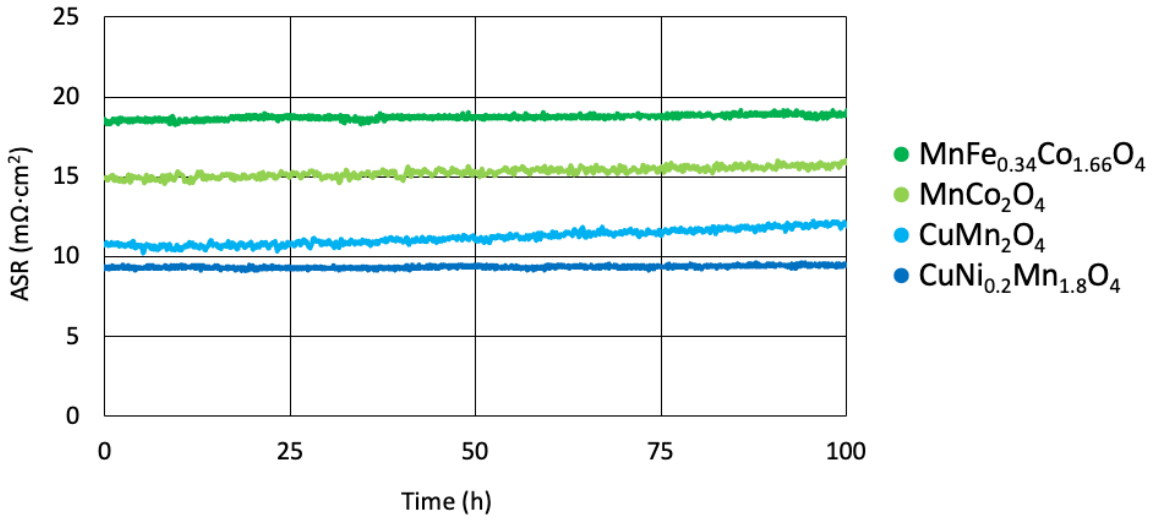

Figure 34. Changes in ASR for spinel coated samples during the 800 ℃ oxidation tests for100 h in flowing air.

4.3.6 High humidity oxidation tests

To evaluate the stability of EPD coatings in a higher humidity environments, additional oxidation tests were carried out on $CuMn_2O_4$, $CuNi_{0.2}Mn_{1.8}O_4$, $MnCo_2O_4$, and

$MnFe_{0.34}Co_{1.66}O_4$ spinel coated flat samples. In all our previous oxidation tests, the air humidity is around 2-3%. For this test, the humidity was increased to 10% by bubbling air through a water bath maintained at 46°C.

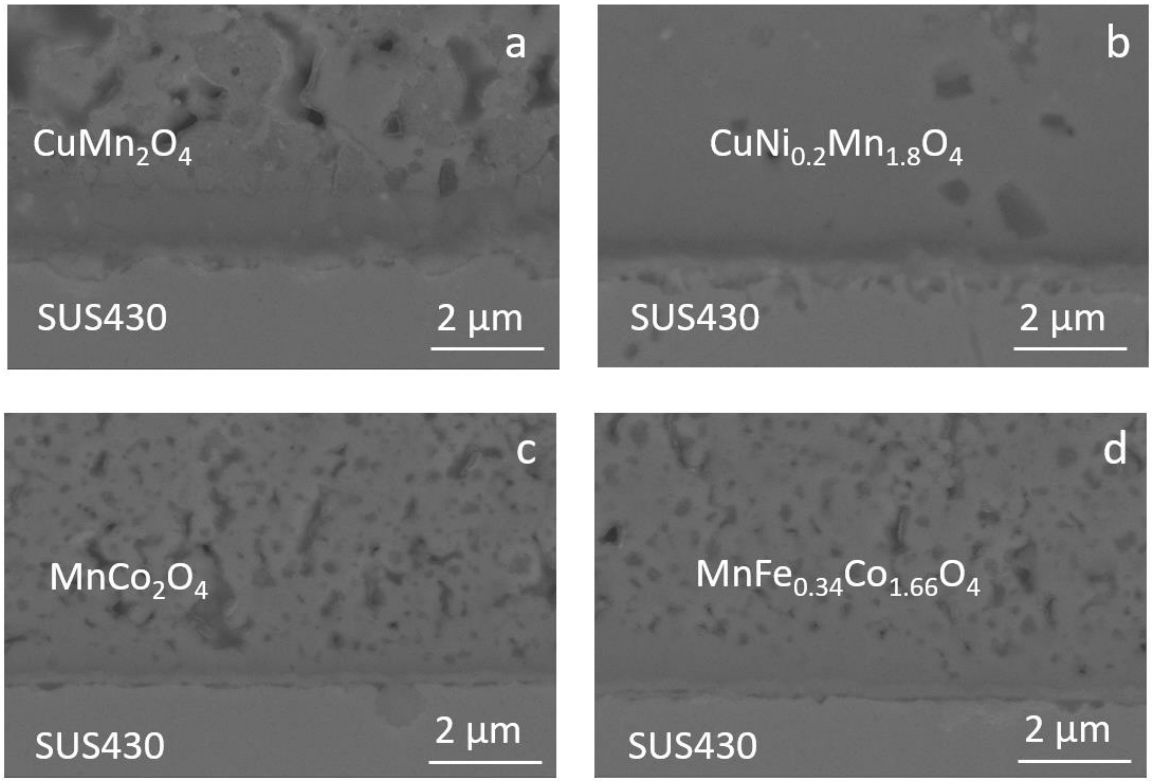

Figure 35. Cross-sectional microstructure of (a)$CuMn_2O_4$ (b)$CuNi_{0.2}Mn_{1.8}O_4$ (c)$MnCo_2O_4$ and (d) $MnFe_{0.34}Co_{1.66}O_4$ samples after 100 h oxidation at 700 ℃ in 10% humidified air.

The coating and densification parameters are the same as previously used. The samples were oxidized at 700°C with 200 ml/min 10% humid airflow for 100 hours. Polished cross-sectional SEM images and EDS line scans were taken after testing. Figure 35 shows the microstructure after the oxidation test. For $CuNi_{0.2}Mn_{1.8}O_4$, $MnCo_2O_4$ and $MnFe_{0.34}Co_{1.66}O_4$ spinel coated samples, no obvious changes in the microstructure were observed as compared to as-densified samples, indicating that the Cr_2O_3 layer had not

grown significantly during the 100 h oxidation in 10% humidified air. The $CuMn_2O_4$ spinel coating had more porosity than the other samples.

The change in the TGO thickness was quantified by EDX line scans. Figure 36 shows the Cr EDS line scans for all the samples after the test. For $CuNi_{0.2}Mn_{1.8}O_4$, $MnCo_2O_4$ and $MnFe_{0.34}Co_{1.66}O_4$ spinel coated samples the thickness of Cr_2O_3 layer was limited under 1 µm thickness. However, the $CuMn_2O_4$ spinel coated sample shows a 1.5 µm Cr_2O_3 layer.

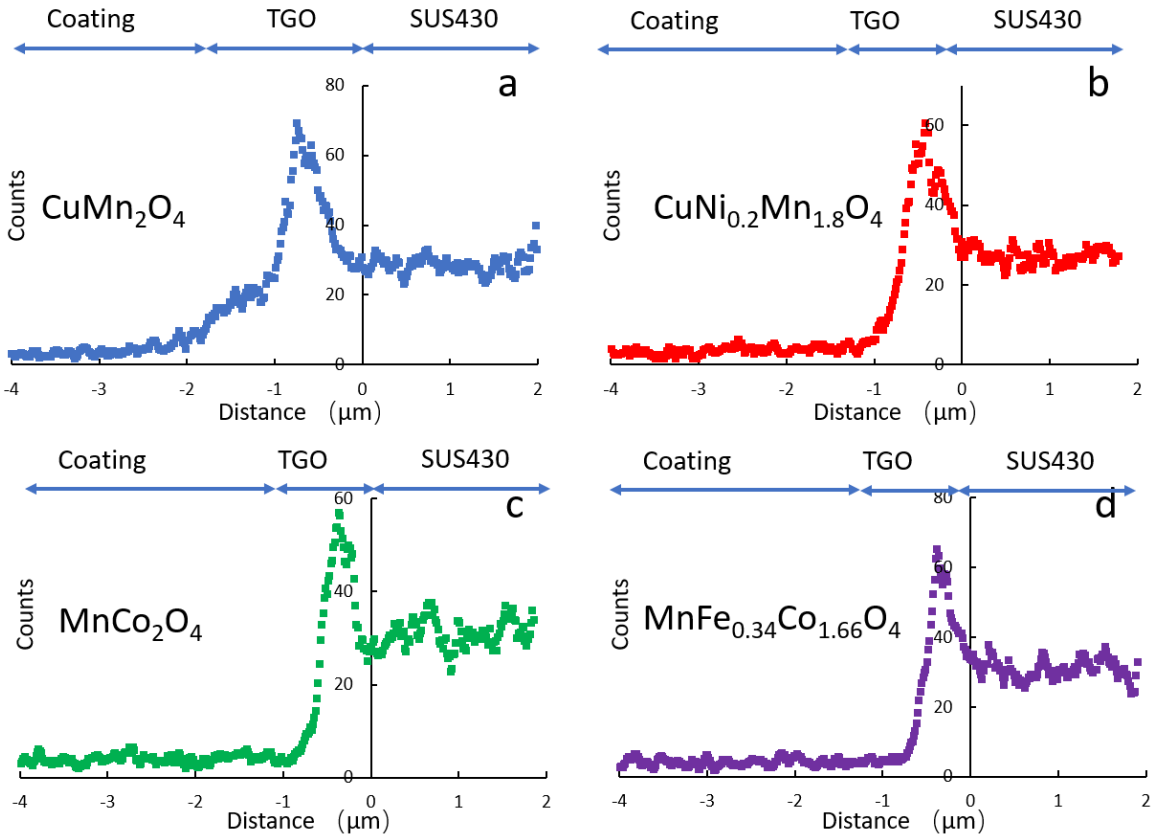

Figure 36. EDS line scans of (a) $CuMn_2O_4$, (b) $CuNi_{0.2}Mn_{1.8}O_4$, (c) $MnCo_2O_4$, and (d) $MnFe_{0.34}Co_{1.66}O_4$ samples after 100 h oxidation at 700 ℃ in 10% humidified air.

Based on the SEM images and EDS line scan, it appears that the $CuNi_{0.2}Mn_{1.8}O_4$,

$MnCo_2O_4$ and $MnFe_{0.34}Co_{1.66}O_4$ spinel coatings are stable in 10% humidified air at 700°C. The $CuMn_2O_4$ spinel coating was less stable, maybe due to the presence of the manganese oxide phase and the larger porosity.

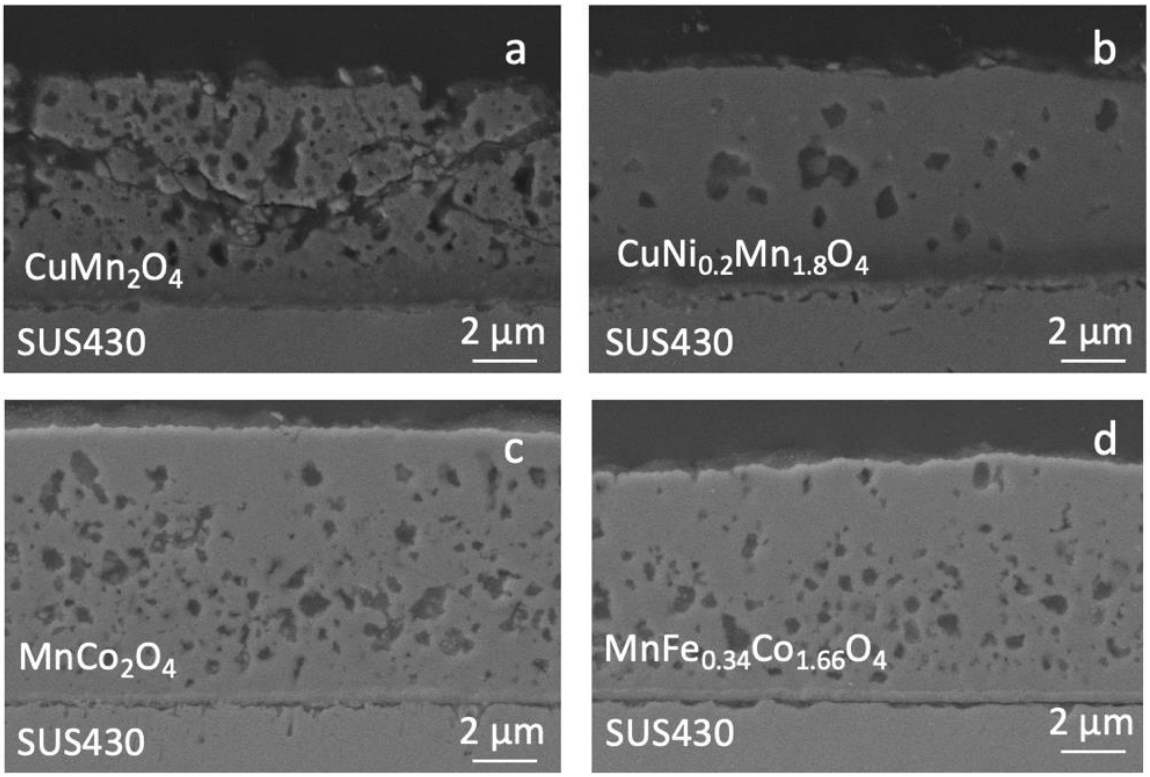

Figure 37. Cross-sectional microstructure of (a)$CuMn_2O_4$ (b)$CuNi_{0.2}Mn_{1.8}O_4$ (c)$MnCo_2O_4$ and (d) $MnFe_{0.34}Co_{1.66}O_4$ samples after100h oxidation at 700 ℃ in 20% humidified air.

The humidity was further increased to 20% by bubbling air through a water bath maintained at 61°C. The samples were oxidized at 700°C with 200 ml/min airflow for 100 hours. After testing, the polished cross-sectional SEM images surface images and EDS line scans were taken. Figure 37 shows the microstructure after the oxidation test. For $CuNi_{0.2}Mn_{1.8}O_4$, $MnCo_2O_4$ and $MnFe_{0.34}Co_{1.66}O_4$ spinel coated samples, no noticeable change in the microstructure was found as compared to the as-densified samples indicating

that the Cr_2O_3 layer has not grown significantly during the 100h oxidation in 20% humidified air. The $CuMn_2O_4$ spinel coated sample exhibited extensive porosity, and some cracks formed in the coating.

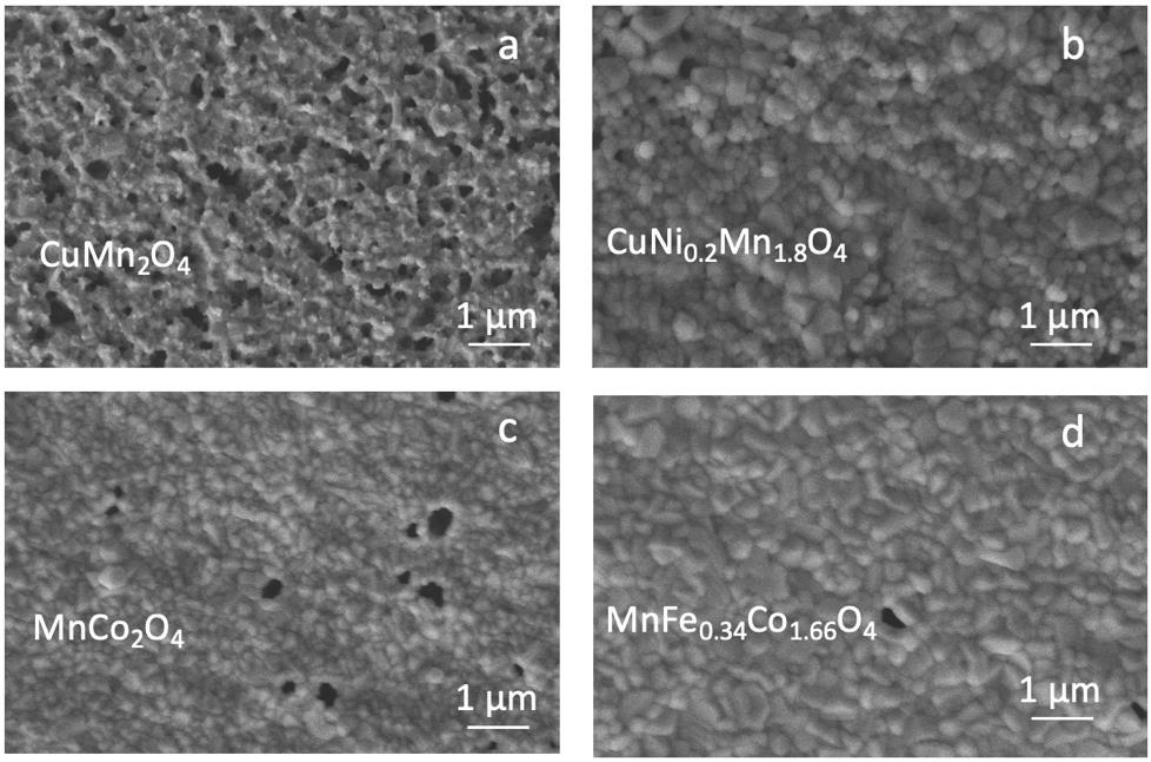

Figure 38. Surface microstructures of (a) $CuMn_2O_4$, (b) $CuNi_{0.2}Mn_{1.8}O_4$, (c) $MnCo_2O_4$, and (d) $MnFe_{0.34}Co_{1.66}O_4$ samples in the as-processed state before oxidation testing in 20% humid air.

Figure 38 and Figure 39 show the surface microstructure of the four coatings before and after the 100 h oxidation test at 20% humidity, respectively. The $CuMn_2O_4$ coated sample exhibits the most surface pores after the oxidation test. The high porosity will allow air and water vapor to get into the coating layer and increase the TGO growth rate. All the other samples appeared to be fairly dense after the oxidation test, although significant grain growth has occurred in the $CuNi_{0.2}Mn_{1.8}O_4$, sample.

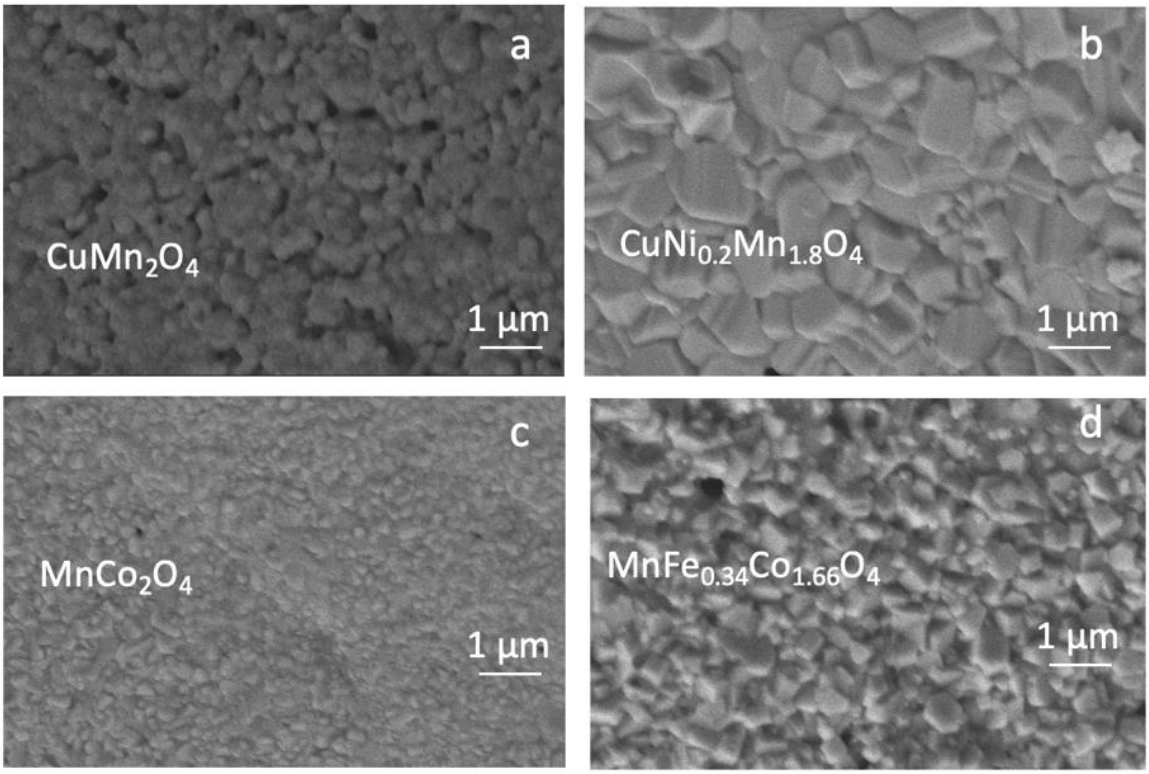

Figure 39. Surface microstructures of (a) $CuMn_2O_4$, (b) $CuNi_{0.2}Mn_{1.8}O_4$, (c) $MnCo_2O_4$, and (d) $MnFe_{0.34}Co_{1.66}O_4$ samples after100 h oxidation at 700 ℃ in 20% humidified air.

Figure 40 shows the Cr EDS line scans for all the samples after the test. The $CuMn_2O_4$ spinel coated sample shows a 1.7 µm thick Cr_2O_3 layer. For $CuNi_{0.2}Mn_{1.8}O_4$, $MnCo_2O_4$, and $MnFe_{0.34}Co_{1.66}O_4$ spinel coated samples the thickness of Cr_2O_3 layer was limited under 1 µm. This result is similar to Cr_2O_3 layer growth in 2% humidified air and 10% humidified air. This means if the coating layer is dense and stable enough, increasing the air humidity will not lead to enhanced Cr_2O_3 layer growth.

Based on the SEM images and EDS line scan, the $CuNi_{0.2}Mn_{1.8}O_4$, $MnCo_2O_4$, and $MnFe_{0.34}Co_{1.66}O_4$ spinel coatings are stable in 20% humidified air at 700°C. The $CuMn_2O_4$ spinel coating is more sensitive to humidity and cannot provide adequate protection to the

substrate.

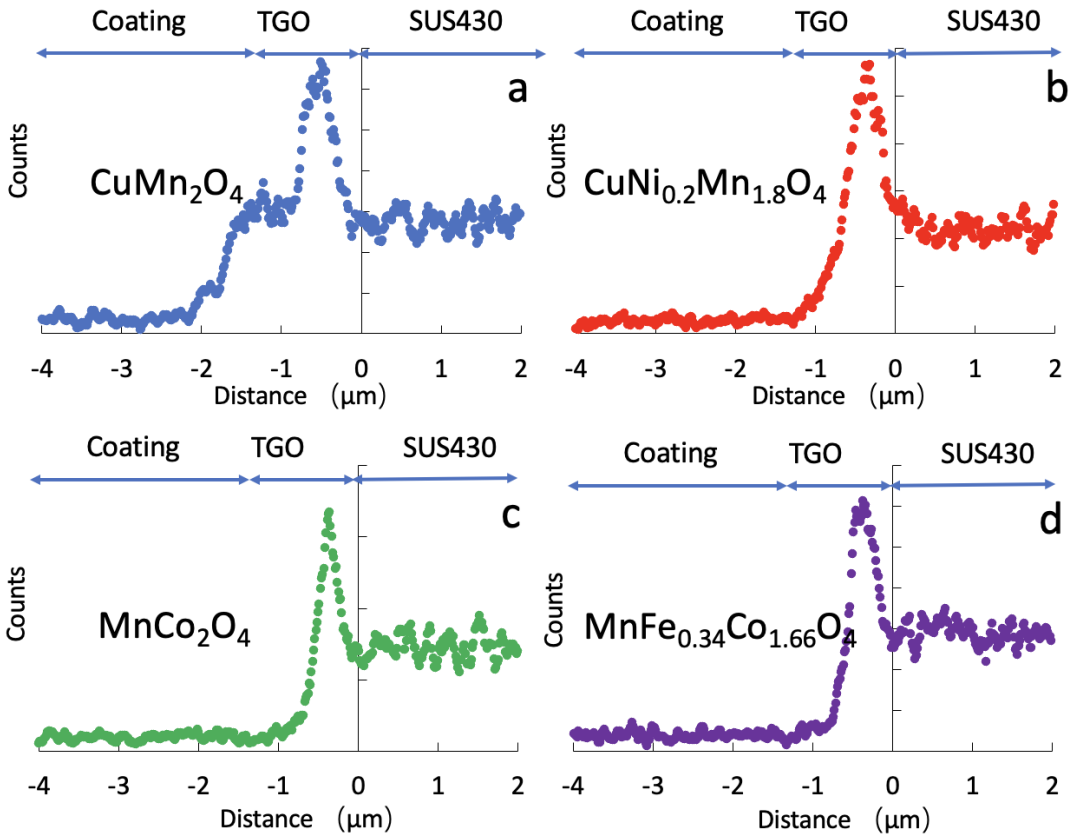

Figure 40. EDS line scans of (a) $CuMn_2O_4$, (b) $CuNi_{0.2}Mn_{1.8}O_4$, (c) $MnCo_2O_4$, and (d) $MnFe_{0.34}Co_{1.66}O_4$ samples after 100h oxidation at 700 ℃ in 20% humidified air.

4.3.7 Interaction between Cr_2O_3 and spinel

The XRD patterns of samples with different molar ratios of $CuMn_2O_4$ and Cr_2O_3 after sintering for 6h at 800°C in air are shown in Figure 41a. For $Cr_2O_3/CuMn_2O_4$ molar ratios of up to 1.2, a pure cubic spinel phase is the only product. At $Cr_2O_3/CuMn_2O_4$ molar ratios of 1.3 and higher, the cubic spinel peaks are accompanied by extra peaks that can be indexed as Cr_2O_3, indicating that saturation has been reached. This suggests that $CuMn_2O_4$

is an excellent getter of Cr (or Cr_2O_3) and at 800°C, and at least 1.2 moles of Cr_2O_3 (or 2.4 moles of Cr) can be incorporated into each mole of $CuMn_2O_4$.

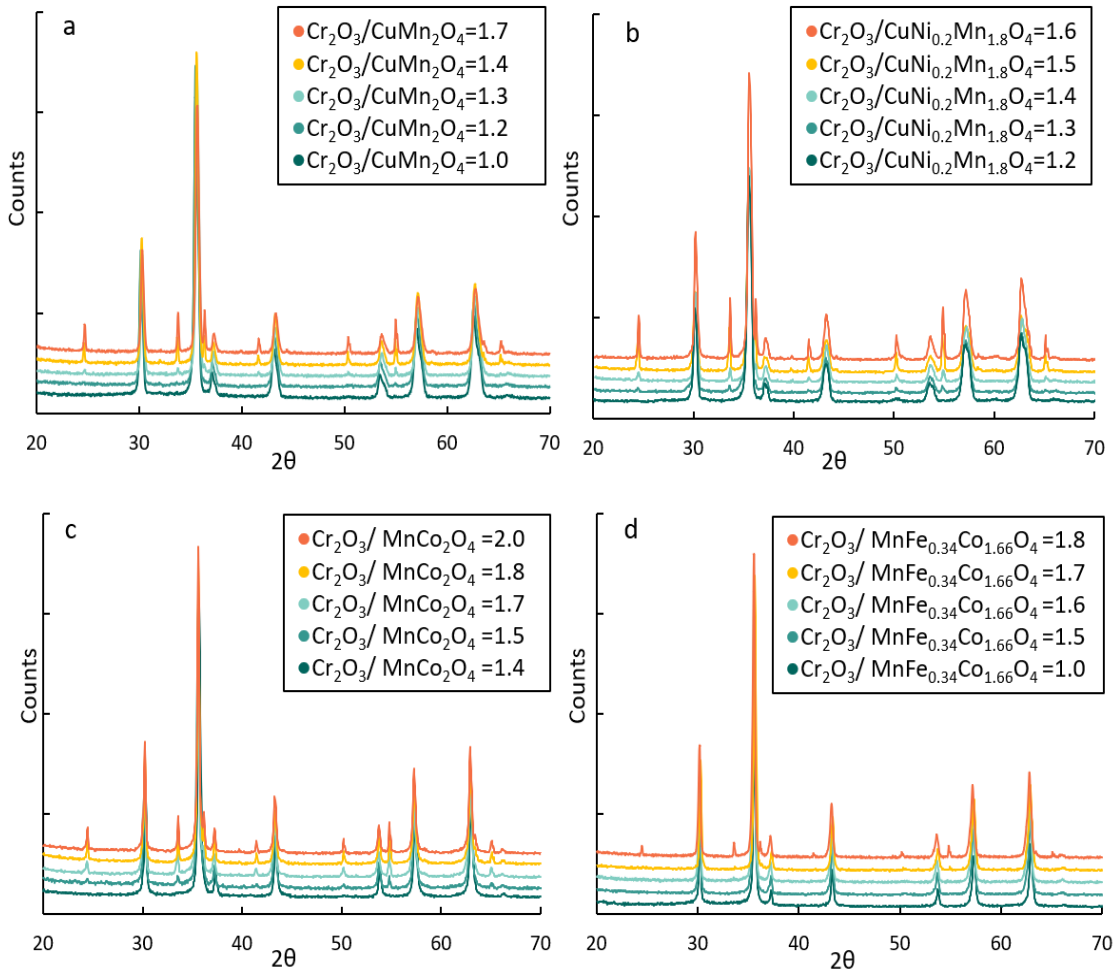

Figure 41. XRD scans of products of reactions between varying molar ratios of (a) $CuMn_2O_4$, (b) $CuNi_{0.2}Mn_{1.8}O_4$, (c) $MnCo_2O_4$, and (d) $MnFe_{0.34}Co_{1.66}O_4$ spinel powders and Cr_2O_3 powders, after annealing the powder mixtures at 800°C in the air for 6 h in air.

The same test was carried out for all other spinel powders, and the results are shown in Figure 41 and summarized in Table 3. The table shows that the saturation $Cr_2O_3/CuNi_{0.2}Mn_{1.8}O_4$ molar ratio is 1.2, which means that Ni doping does not change the

Cr getter ability. In contrast, the saturation $Cr_2O_3/MnFe_{0.34}Co_{1.66}O_4$ molar ratio is 1.7, which is larger than the saturation molar ratio of $Cr_2O_3/MnCo_2O_4$ value 1.4.

Table 3. Cr solubility in all spinel samples.

Sample	**$CuMn_2O_4$**	**$CuNi_{0.2}Mn_{1.8}O_4$**	**$MnCo_2O_4$**	**$MnFe_{0.34}Co_{1.66}O_4$**
Cr solubility	2.4	2.4	2.8	3.4

4.4 Conclusions

In this research, $CuMn_2O_4$, $CuNi_{0.2}Mn_{1.8}O_4$, $MnCo_2O_4$, and $MnFe_{0.34}Co_{1.66}O_4$ spinel powders were fabricated by the glycine nitrate process. Spinel compositions were examined by XRD and SEM, and conductivities were measured. Spinel protective coating layers were deposited by EPD on flat SUS430 substrates. Samples were densified by the two-step densification method. Oxidation tests at 700°C and 800°C in dry air and humidified air were carried out for 100h. Area-specific resistances (ASR) were tracked during oxidation. The changes in Cr concentration profiles were measured. The results show that $CuMn_2O_4$ is not a pure phase at room temperature, and that Ni doping makes $CuNi_{0.2}Mn_{1.8}O_4$ phase pure.

Cu-Mn based spinels have higher conductivities than Mn-Co based spinels. Doping with Ni increases the conductivity of Cu-Mn spinel, but doping with Fe decreases the conductivity of Mn-Co spinel. Mn-Co based spinels coatings are able to better limit TGO growth than Cu-Mn spinel coatings. $MnFe_{0.34}Co_{1.66}O_4$ shows the best performance in limiting TGO growth, it has better stability at high temperatures and the largest Cr gettering ability, but it also has the lowest electrical conductivity. $CuNi_{0.2}Mn_{1.8}O_4$ has the highest

conductivity. It also has high phase stability, low porosity and better sinterability. Finally, Cu is more inexpensive than Co, making the per mole cost of Cu-Mn spinels to be less than Mn-Co spinels. The properties of the four spinels are summarized in Table 4 in relative terms. Overall, based on Table 4, $CuNi_{0.2}Mn_{1.8}O_4$ is the best option of the four spinels tested.

Table 4. Summary of comparative spinel properties.

Spinel/Property	**$CuMn_2O_4$**	**$CuNi_{0.2}Mn_{1.8}O_4$**	**$MnCo_2O_4$**	**$MnCo_{1.66}Fe_{0.34}O_4$**
Sinterability	Worst	Best	Good	Good
Cr gettering	Worst	Worst	Good	Best
Conductivity	Good	Best	Worse	Worst
Cr profile	Bad	Good	Bad	Best
Phase stability	Worst	Good	Good	Good
ASR	Worst	Best	Normal	Good
Humidity test	Worst	Good	Good	Good
Cost	Best	Best	Worse	Worse

5. Composition optimization of $CuNi_xMn_{2-x}O_4$

5.1 Introduction

In the previous chapter, it was shown that Ni-doped Cu-Mn spinel had higher conductivity and better phase stability compared to undoped Cu-Mn spinel. An additional study was carried out to optimize the Ni/Mn ratio to get the best performing Ni-doped Cu-Mn spinel composition for EPD coatings. Four spinel powder samples were produced by the GNP method with varying Ni-doping concentrations, which were $CuMn_2O_4$, $CuNi_{0.2}Mn_{1.8}O_4$, $CuNi_{0.4}Mn_{1.6}O_4$, and $CuNi_{0.6}Mn_{1.4}O_4$. The powders were deposited as coatings on flat SUS430 substrates by electrophoretic deposition using parameters detailed earlier (20V, 5min deposition). The standard two-step densification heat treatment (reduction in 100%H_2 at 950 °C for 6h, re-oxidation in air at 750°C for 24h) was used to form thin, dense, and uniform, coating layers. The phase stability of the powders was examined by XRD, and the powders were sintered into bar samples for conductivity measurements. The coatings were tested for 100 h at 800º C in flowing air to evaluate their ability to limit Cr_2O_3 growth and out-ward Cr diffusion. The microstructure changes and the Cr concentration profiles were characterized after the high temperature oxidation exposures.

5.2 Phase stability

Figure 42 shows the XRD scans of the four spinel powder samples at room temperature. The figure shows that $CuNi_{0.2}Mn_{1.8}O_4$, $CuNi_{0.4}Mn_{1.6}O_4$, and $CuNi_{0.6}Mn_{1.4}O_4$ powders exhibit standard cubic spinel peaks indicating that the spinel powders were phase-

pure. Besides the spinel peaks, $CuMn_2O_4$ powders also exhibited Mn_3O_4 peaks as previously reported in Chapter 4, implying that the powder was a mixture of the spinel and manganese oxide phases at room temperature.

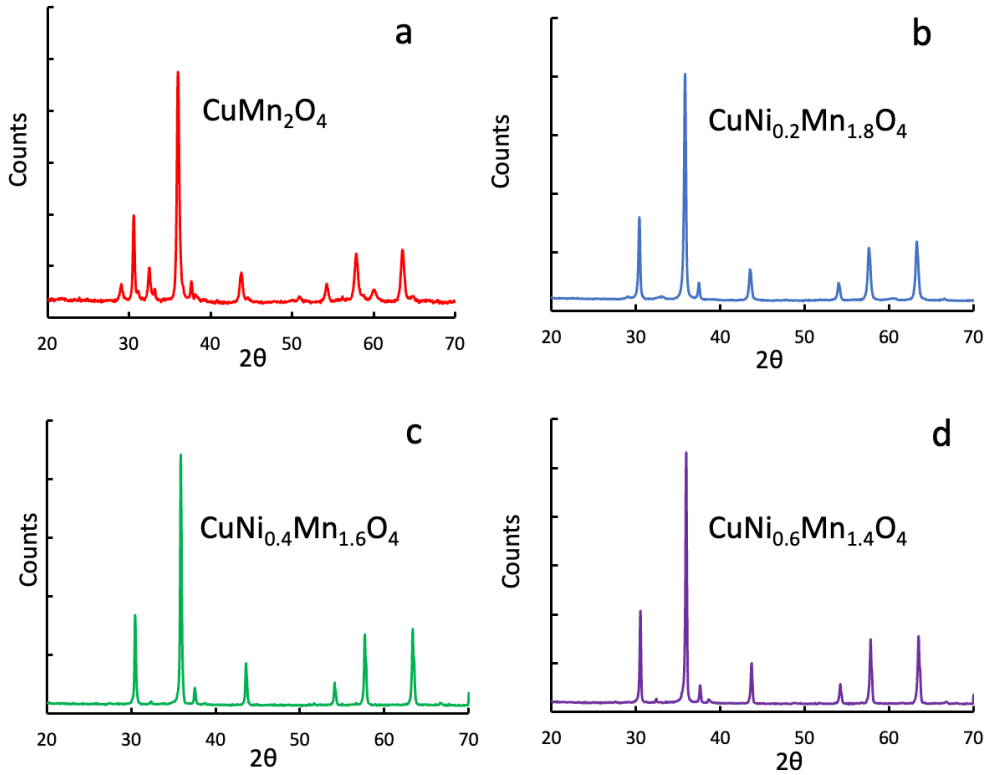

Figure 42. XRD scans of (a) $CuMn_2O_4$, (b) $CuNi_{0.2}Mn_{1.8}O_4$, (c) $CuNi_{0.4}Mn_{1.6}O_4$, and (d) $CuNi_{0.6}Mn_{1.4}O_4$ powders at room temperature.

5.3 Conductivity measurements

To measure the conductivity, spinel powders were compressed in a mold and sintered at 1000℃ for 20 h to get a dense spinel bar, and then held at 800 ℃ for 10h to equilibrate the phase at the measurement temperature. After sintering, the conductivities of the bars were measured by the four-probe method. Figure 43 shows the conductivities of spinel bars, each corrected for sample porosity measured from polished cross-sections

(Figure 44).

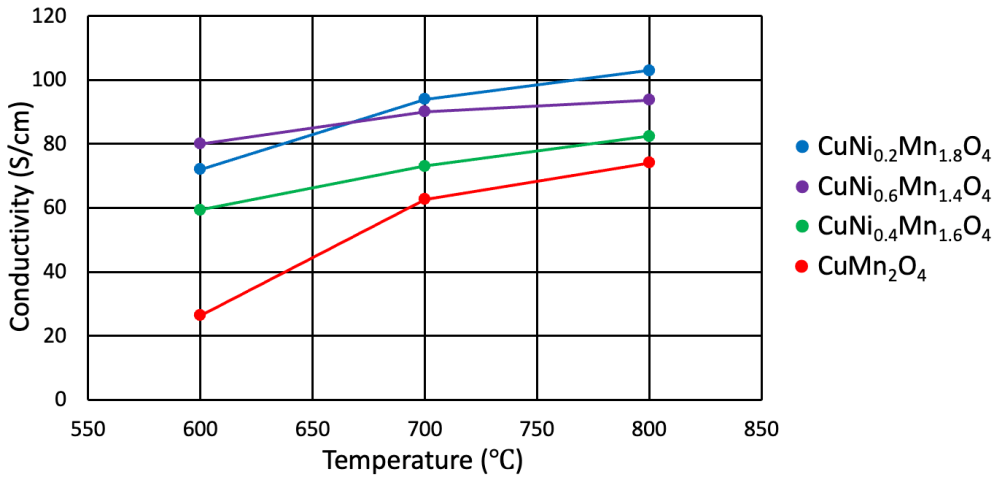

Figure 43. The conductivity of undoped and various Ni-doped Cu-Mn spinels as a function of temperature.

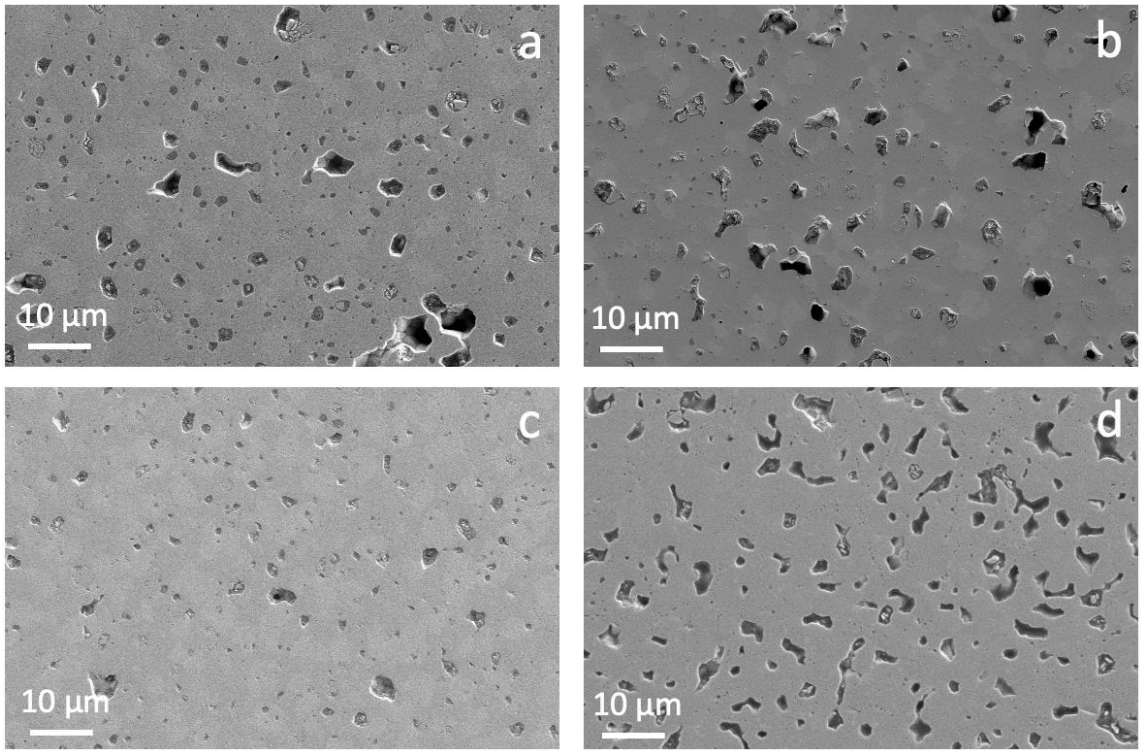

Figure 44. SEM images of polished cross-sections of (a) $CuMn_2O_4$, (b) $CuNi_{0.2}Mn_{1.8}O_4$, (c) Cu $Ni_{0.4}Mn_{1.6}O_4$, and (d) $CuNi_{0.6}Mn_{1.4}O_4$ bar samples.

It was found that $CuMn_2O$ has the lowest conductivity from 600°C to 800°C. $CuNi_{0.2}Mn_{1.8}O_4$ has the highest conductivity from 700°C to 800°C. $CuNi_{0.6}Mn_{1.4}O_4$ had the highest conductivity at 600°C. The results show that at any given temperature, the change in conductivity with increasing Ni content in the Cu-Mn spinel does not change monotonically. This suggests that multiple mechanisms may be responsible for the change in conductivity with changing Ni doping.

5.4 Microstructure of EPD coatings

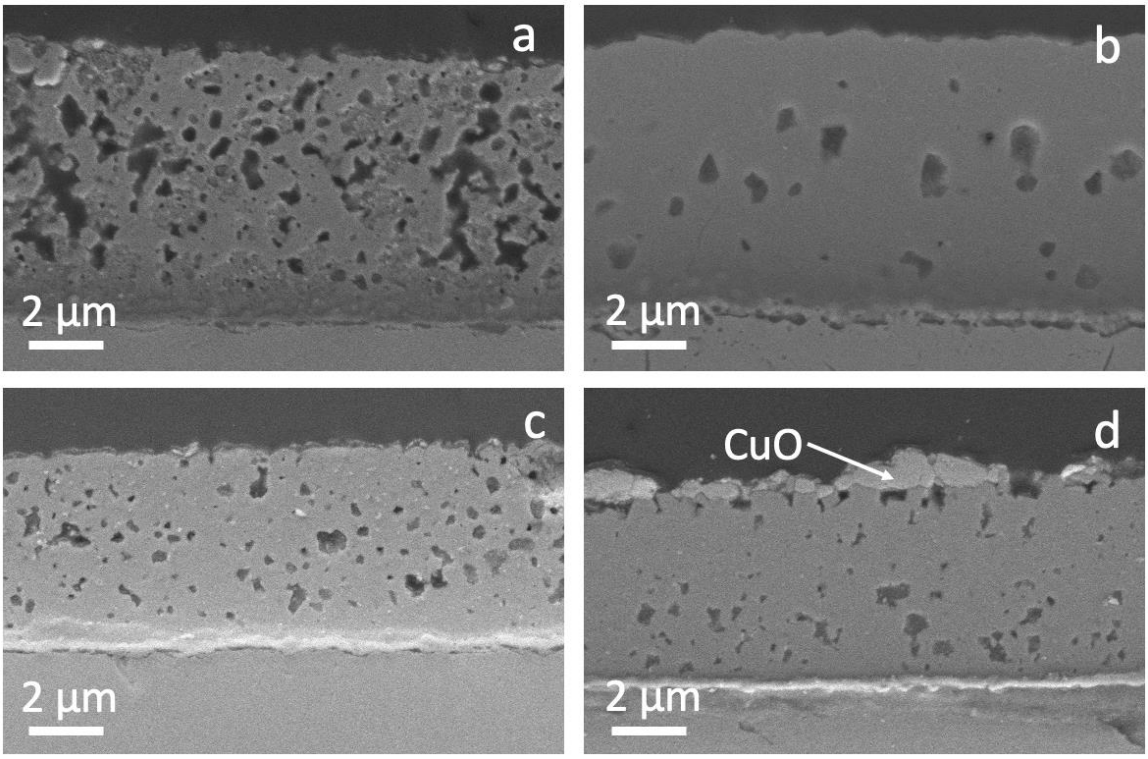

Figure 45. Cross-sectional microstructure of (a) $CuMn_2O_4$, (b) $CuNi_{0.2}Mn_{1.8}O_4$, (c) $CuNi_{0.4}Mn_{1.6}O_4$, and (d) $CuNi_{0.6}Mn_{1.4}O_4$ samples after the re-oxidation anneal.

Figure 45 shows the microstructures of the four Cu-Mn-based spinel coatings after the densification step. The $CuNi_{0.2}Mn_{1.8}O_4$ spinel coating exhibited the smallest porosity of ~ 9%. The porosity $CuNi_{0.4}Mn_{1.6}O_4$ and $CuNi_{0.6}Mn_{1.4}O_4$ layers are similar (~ 13%). $CuMn_2O_4$ shows the largest porosity compared to other samples. The figure shows the presence of a separate phase formed on the surface of the $CuNi_{0.6}Mn_{1.4}O_4$ sample, which shows up as a lighter color. EDS analysis of this phase shows it is Cu-rich. Sun and co-workers observed such Cu-rich phases forming on the surface of $Cu_{1.3}Mn_{1.7}O_4$ coatings and identified them as CuO by XRD [39]. In this case, the formation of the CuO phase could be that the increase in the Ni amount to 0.6, the Ni will not only sit in the B(Mn) site, but also occupy the A(Cu) site, thereby displacing Cu. CuO is an insulating phase and its formation on the surface of the coating can lead to deterioration of the connection between the interconnect and the electrode.

5.5 Oxidation tests for spinel coated samples

The $CuMn_2O_4$, $CuNi_{0.2}Mn_{1.8}O_4$, $CuNi_{0.4}Mn_{1.6}O_4$, and $CuNi_{0.6}Mn_{1.4}O_4$ spinel coated were oxidized for 100 h at 800°C in flowing air. Polished cross-sectional SEM images surface images, and EDS line scans were taken after tests. Figure 46 shows the surface microstructure of the coatings before the oxidation test. The $CuMn_2O_4$ coating surface exhibited the large porosity and roughest surface, The surfaces of $CuNi_{0.4}Mn_{1.6}O_4$ and $CuNi_{0.6}Mn_{1.4}O_4$ coatings had some surface porosity, but it was lower than that in $CuMn_2O_4$. The surface of the $CuNi_{0.2}Mn_{1.8}O_4$ coating appeared much denser than other samples.

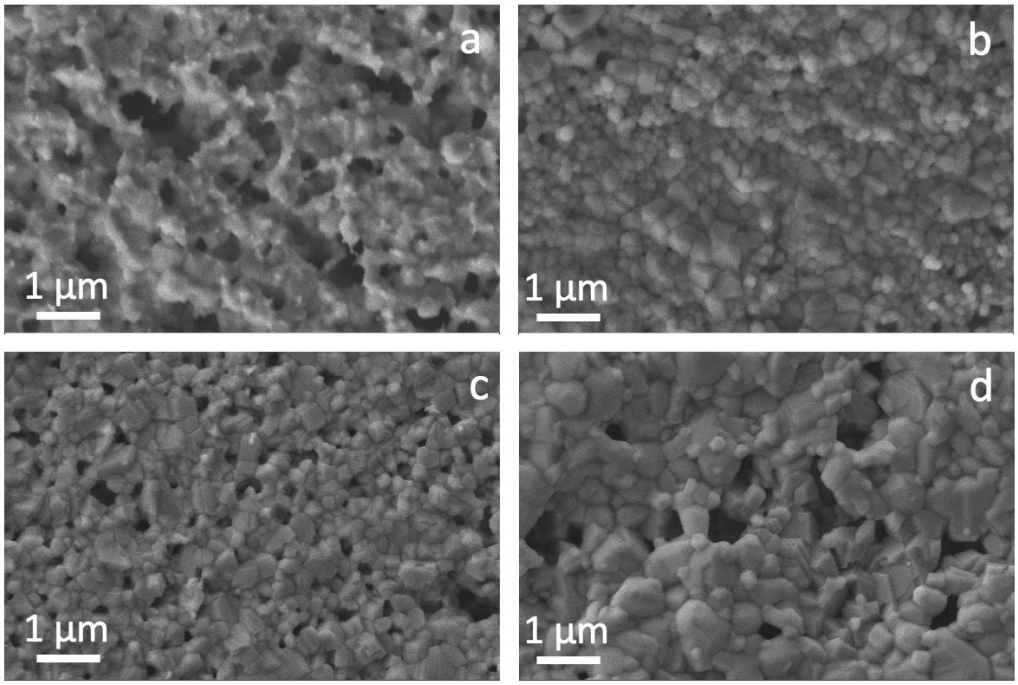

Figure 46. Surface microstructure of (a) $CuMn_2O_4$, (b) $CuNi_{0.2}Mn_{1.8}O_4$, (c) $CuNi_{0.4}Mn_{1.6}O_4$, and (d) $CuNi_{0.6}Mn_{1.4}O_4$ coatings before the oxidation test.

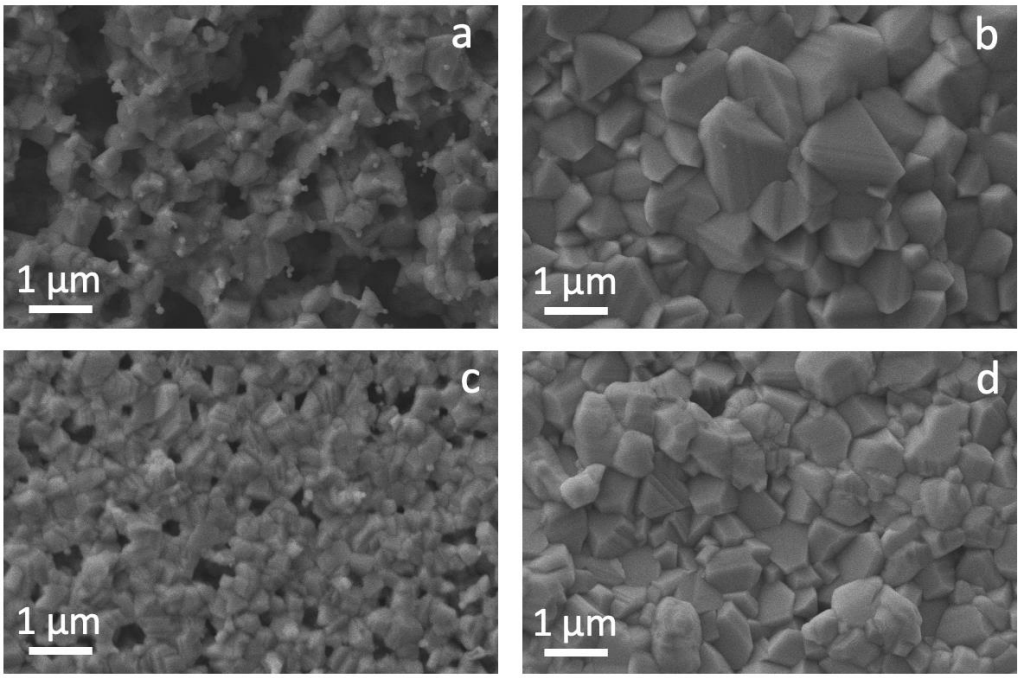

Figure 47. Surface microstructures of (a) $CuMn_2O_4$, (b) $CuNi_{0.2}Mn_{1.8}O_4$, (c) $CuNi_{0.4}Mn_{1.6}O_4$, and (d) $CuNi_{0.6}Mn_{1.4}O_4$ coating samples after100 h oxidation at 800°C in air.

Figure 47 shows the surface microstructure of the four coatings after the 800°C oxidation test. All four spinels clearly exhibited grain growth. For the $CuMn_2O_4$ coated sample, the surface porosity increased after oxidation. The porosity on the surface of the $CuNi_{0.4}Mn_{1.6}O_4$ coating did not change much. The surface of the $CuNi_{0.6}Mn_{1.4}O_4$ coating appeared dense after oxidation test. The $CuNi_{0.2}Mn_{1.8}O_4$ coating surface remained dense after oxidation, but exhibited the largest grain growth among all the coatings.

Figure 48 shows SEM micrographs of polished cross-sections of the coatings after the oxidation test. The excessive porosity in the $CuMn_2O_4$ coating can be clearly seen. The $CuNi_{0.2}Mn_{1.8}O_4$ coating is clearly the densest, and the CuO phase can be seen clearly at the top of the $CuNi_{0.6}Mn_{1.4}O_4$ coating.

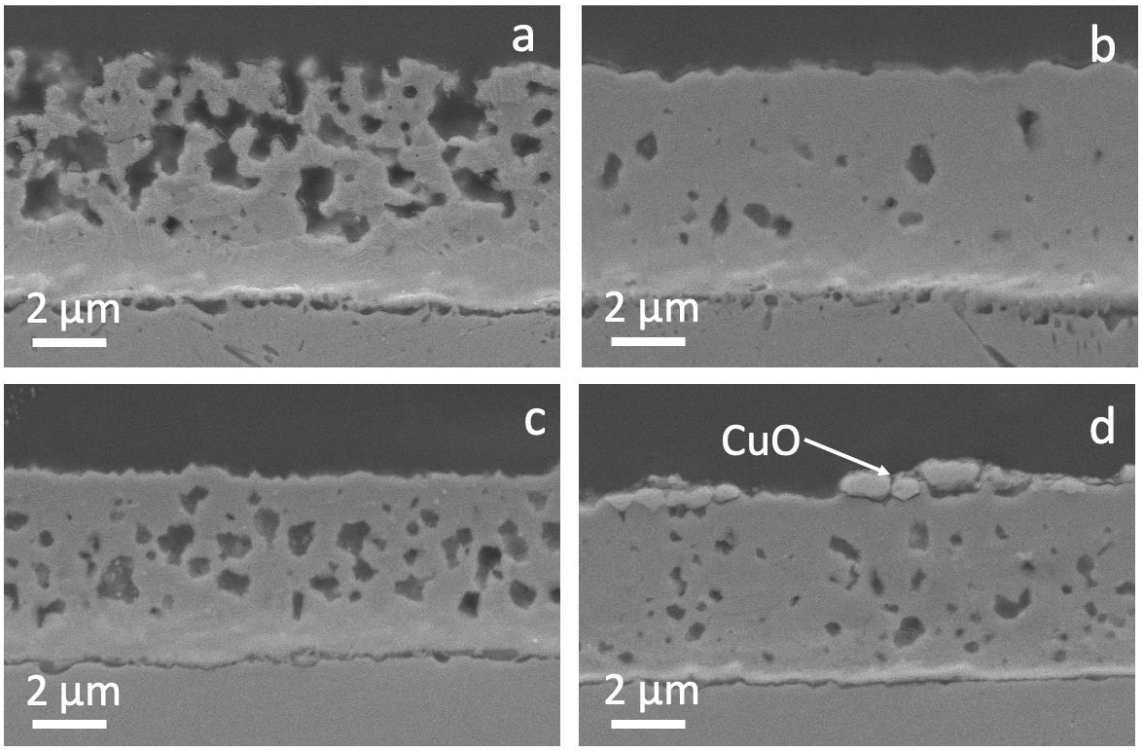

Figure 48. Cross-sectional microstructures of (a) $CuMn_2O_4$, (b) $CuNi_{0.2}Mn_{1.8}O_4$, (c) $CuNi_{0.4}Mn_{1.6}O_4$, and (d) $CuNi_{0.6}Mn_{1.4}O_4$ samples after 100h oxidation at 800 ℃ in air.

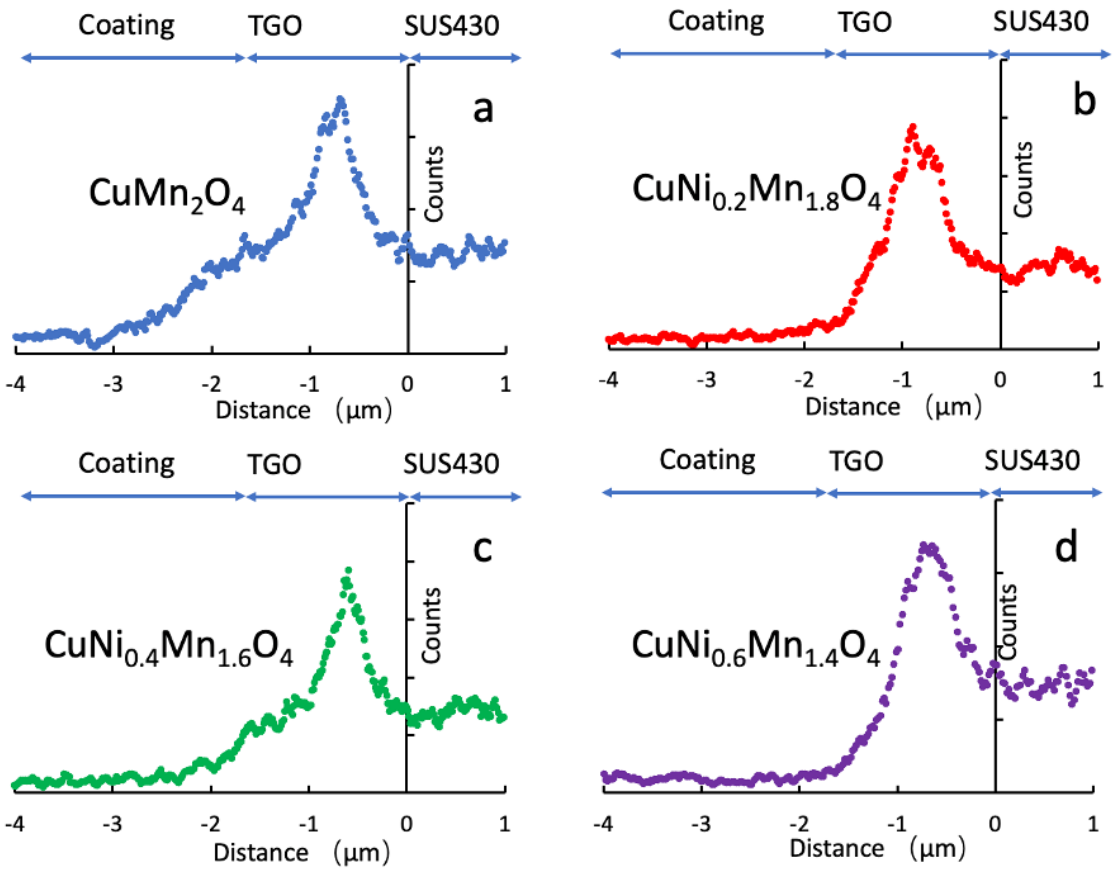

Figure 49. EDS line scans of (a)$CuMn_2O_4$ (b)$CuNi_{0.2}Mn_{1.8}O_4$ (c) $CuNi_{0.4}Mn_{1.6}O_4$ (d) $CuNi_{0.6}Mn_{1.4}O_4$ samples after 100h oxidation at 800°C in air.

Figure 49 shows the Cr EDS line scans across the coating. The thickness of Cr rich layer for $CuNi_{0.2}Mn_{1.8}O_4$ (1.4μm), and $CuNi_{0.6}Mn_{1.4}O_4$ (1.3μm) samples are comparable and are the smallest. In contrast, the Cr profiles show that the Cr-rich later on $CuMn_2O_4$ (1.8μm) and $CuNi_{0.4}Mn_{1.6}O_4$ (1.6μm) samples are thicker, and both have a substantial tail to the left of the peak, indicating Cr out-diffusion in the coatings.

5.6 Conclusions

The large porosity of the $CuMn_2O_4$ coating made the coating layer brittle and cracks formed during the oxidation test. It is possible that the presence of manganese oxide phase

in this coating at room temperature added to the cracking phenomenon observed for this coating. The porosity of the $CuNi_{0.4}Mn_{1.6}O_4$ sample was smaller than that in the $CuMn_2O_4$ sample but still larger than that in the $CuNi_{0.2}Mn_{1.8}O_4$ sample. The $CuNi_{0.6}Mn_{1.4}O_4$ coating formed a CuO phase on the coating surface. The $CuNi_{0.2}Mn_{1.8}O_4$ coating exhibited the smallest porosity, the highest electrical conductivity, and was phase pure. Thus, a Ni doping content of 0.2 was found to be the optimal concentration for doped Cu-Mn spinels.

6. Alternating current EPD on porous substrates

6.1 Introduction

Stainless steels such as SUS430 are not only widely used as interconnects in SOFC applications and also as electrodes in metal-supported SOFCs [15, 16]. However, due to the porous structure, the surface/volume ratio of porous stainless steel interconnects is much larger than dense interconnects. Therefore, per nominal cross-sectional area of the interconnect, the rate of mass gain due to TGO growth is significantly higher than in the case of flat substrates. This can lead to accelerated rates of chromium poisoning.

In order to limit TGO growth and to avoid chromium poisoning, $CuNi_{0.2}Mn_{1.8}O_4$ spinel powders were fabricated and coated on porous SUS430 substrates using AC EPD. The specific challenges of depositing uniform coatings on porous substrates are discussed in this section. A two-step densification method was used after deposition. To evaluate the effectiveness of the protective coating layer, a 100h oxidation test at 700 °C in air was carried out. Area specific resistance and weight gain of the samples were tracked during oxidation. Microstructural changes in the coating were examined, and the Cr concentration profiles were measured. The results showed that despite the considerable complexity of the sample shape, the AC EPD was able to deposit a protective coating layer that limited Cr diffusion in the coating, and significantly reduced the growth rate of the thermally grown oxide. To the best of our knowledge, this is the first example of oxidation-resistant AC EPD coatings on porous metallic substrates for SOFC applications.

6.2 Experimental Methods

The glycine-nitrate combustion synthesis process was used to fabricate fine and homogeneous $CuNi_{0.2}Mn_{1.8}O_4$ spinel powders [28]. Our previous work showed that using glycine/nitrate molar ratio at 0.63 leads to an optimal combustion reaction. Proportional quantities of reactants were dissolved in DI water, and after stirring for 10 minutes, a clear, blue solution was formed. The solution was heated on a hot-plate at ~90°C to evaporate excess water. The beaker was then covered with a fine stainless-steel mesh to prevent ejection of fine powders that form during combustion, and the temperature of the hot plate was then set to 500°C. Heating tape was used around the beaker and set to 100°C to avoid water condensation on beaker wall during the reaction. Spontaneous combustion and powder formation typically occurred before the set temperature was reached. The resulting powders were transferred to a box furnace and calcined in air for 2 h at 800°C to remove residuals [29, 30].

In order to decrease the size of spinel powders, the powders were dispersed in ethanol and ball milled using 0.05 mm yttria-stabilized zirconia (YSZ) balls in a SPEX Sample Prep 8000 M Mixer/Mill. After ball milling, the YSZ balls were removed by sieving. The powders were dispersed in an ethanol and acetone solution. After ultrasonically vibrating the powder solution for 15 minutes, an iodine/ethanol solution was added to the suspension. The I_2 reacts with acetone and releases H^+ ions that adhere to the spinel particles making them positively charged. The suspension was then ultrasonically vibrated for 15 min to ensure thorough mixing and reaction.

An AC signal generating setup was designed in our laboratory (Figure 50). The setup contains a dual DC power supply, a function generator, an oscilloscope, a signal transfer circuit, and a small DC power supply for the transfer circuit. The setup can generate pulsed DC signals or AC signals with variable duty cycles with independently adjustable positive and negative voltages and time ratios. The output voltage ranges from -50V to +50V, and the frequency ranges from 10Hz to 1000Hz.

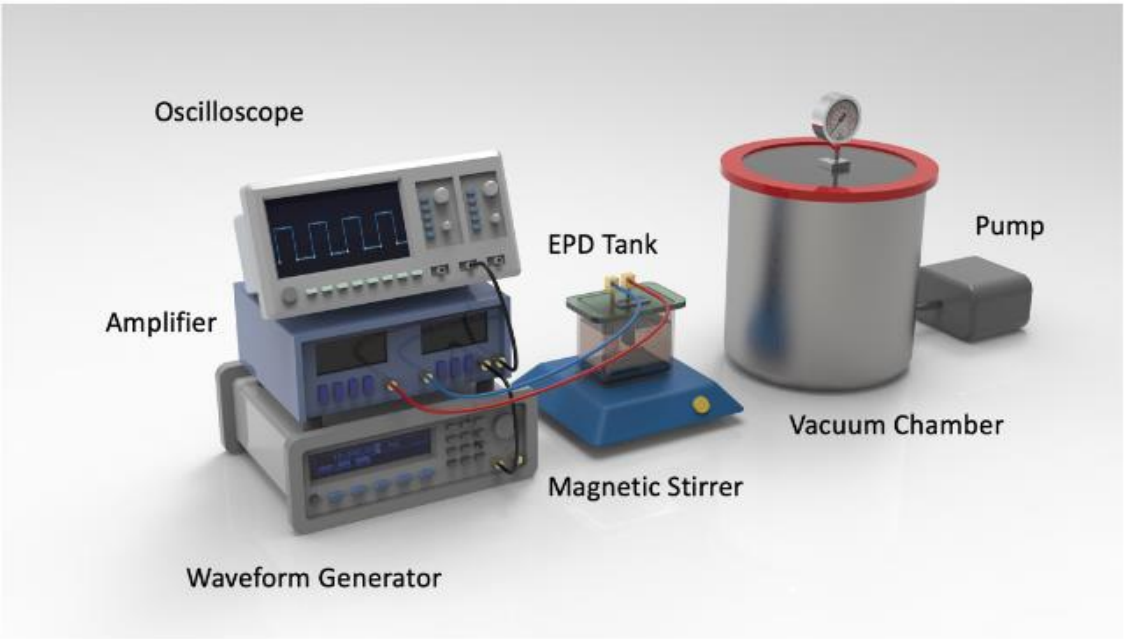

Figure 50. AC signal generating setup.

Porous SUS430 substrates of dimensions 1 cm × 1 cm × 0.4 cm were used as the cathode with a 6 cm × 5 cm × 0.1 cm Cu plate as the anode. The electrodes were immersed into the suspension of spinel powders. Before deposition, the sample within the suspension was placed in a vacuum chamber for 10 min to remove air bubbles. When a negative bias is applied to the cathode, the positively charged spinel particles migrate to the cathode due

to electrostatic forces. The AC signal used for deposition as shown in Figure 51. It should be noted that since the powders are positively charged (due to surface adsorbed H^+), negative voltages correspond to coating deposition mode and positive voltages correspond to coating removal mode. The coatings were deposited for 15 minutes in total and a magnetic stirrer was used to increase powder mobility inside the substrates. To study the effectiveness of using AC EPD, a DC EPD coating was deposited on a reference sample, using a -20V DC signal for 3 min.

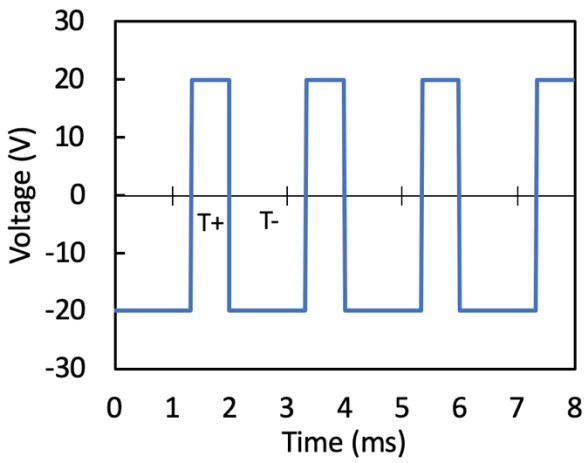

Figure 51. AC signal used for deposition.

The as-deposited coatings need further densification. A two-step heat treatment was used for densification, which consisted of a reduction anneal followed by a re-oxidation anneal. As-deposited samples were reduced at 950°C for 2 h in pure H_2, during which the spinel is reduced to a Cu-Ni alloy and manganese oxide. The sample was then cooled down to room temperature and then annealed in air at 750°C for 24 h, leading to denser $CuNi_{0.2}Mn_{1.8}O_4$ spinel coating.

Oxidation tests were carried out for both uncoated and AC EPD coated samples at 700 °C for 100h in air. During the oxidation exposure, thermogravimetric (TGA, TA Q600 microbalance) measurements were also carried out and the weight changes of both samples were continuously recorded. In addition, area specific resistance (ASR) measurements were separately carried out for 100 h exposure at 700°C in air, using a 4-quadrant power potentiostat (Zahner PP211). For these measurements, silver mesh and paste were applied on both sides of sample, and the potential was tracked when a 0.2A current was applied. It should be noted that the coated samples for TGA and ASR measurements were different, but both were prepared under identical conditions.

Powder samples were examined by the X-ray diffraction (XRD, Bruker D8 Advance XRD system) and scanning electron microscopy (SEM, Zeiss Supra 55 VP). Uncoated and coated samples at various stages were mounted in epoxy and polished in cross-section. Polished cross-sections were examined by SEM to track microstructure changes. Energy dispersive spectroscopy (EDS, Oxford Instruments, High Wycombe, UK) was used in line scan and elementary mapping modes to analyze the compositional distribution in the coating.

6.3 Results and Discussion

Figure 52a and b show SEM micrographs of as-deposited samples by DC EPD and AC EPD. In the figure, images have two parts. The top parts of the images show the microstructures of the middle areas of the porous samples, where the powders have to diffuse through connected pores to reach such areas. The bottom parts of the images show

the microstructures near the surface of the porous samples, where the powders have easier access to the near-surface pores. It shows that AC deposition can get a significantly larger amount of powders into inner pores without clogging pores. The DC EPD sample (Figure 52a) shows a thick coating on the surface of the sample, which effectively clogs up the surface pores, resulting in very little coverage of the inner pore surfaces by the coating. In contrast, the coverage after AC EPD deposition (Figure 52b) is much more uniform. The surface of the sample is coated, but without clogging up the surface pores. This allows for good coverage of the inside pores of the sample. This shows AC EPD is a much more effective deposition process for uniform coverage of porous substrates.

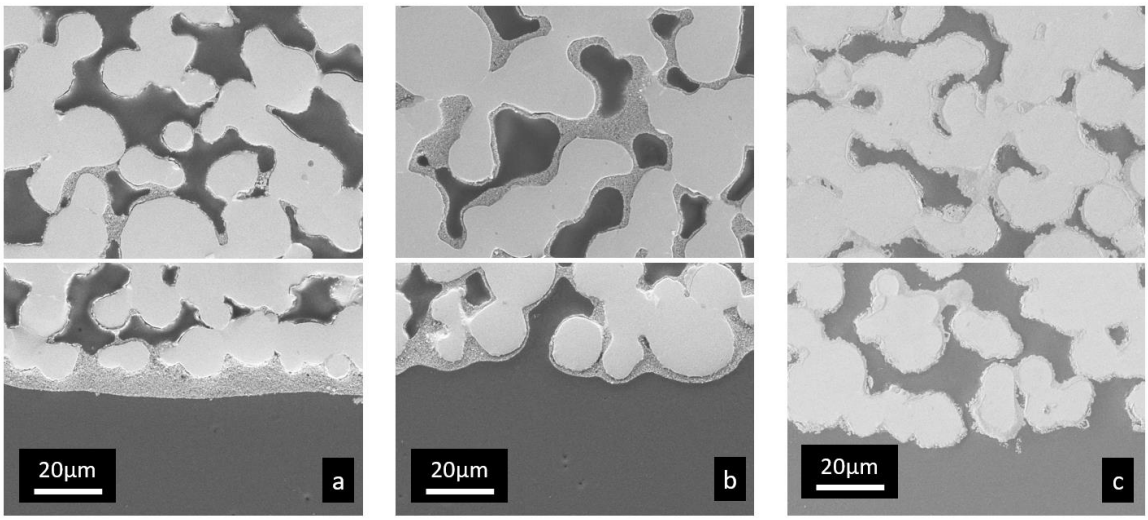

Figure 52. SEM micrographs of cross-sections of (a) as-deposited DC EPD sample, (b) as-deposited AC EPD sample, and (c) AC EPD sample after the two-step densification process. The top parts of the images show pores in the middle of the samples, while the bottom parts of the images show near-surface pores.

Figure 51 shows the AC voltage signal, with -20V signal corresponding to the deposition portion of the cycle, and +20V corresponding to the removal portion of the

cycle. Since the deposition time is longer than the removal time, there is net deposition during the cycle. By alternating deposition and removal, the film thickness can be better controlled. Due to the excellent conductivity of the metallic interconnect, the voltage is fairly uniform in all parts of the porous substrate. As the coating has significantly lower electronic conductivity, the voltage drops rapidly in the coating, going away from the substrate/coating interface. Thus, if the coating gets to be thicker in one part of the sample compared to other areas, powders in the outer part of that area of the coating is most susceptible to removal during the +20V exposure. This creates an auto-correcting mechanism that prevents coating thickness in any portion of the sample to be significantly different from the coating thickness on other parts of the sample. This keeps the surface pores open, which along with the stirring of the EPD solution allows powders to reach the inside pores of the sample. Figure 52c shows the microstructure of AC EPD sample after two-step densification. A dense and uniform coating layer was formed on all pore surfaces.

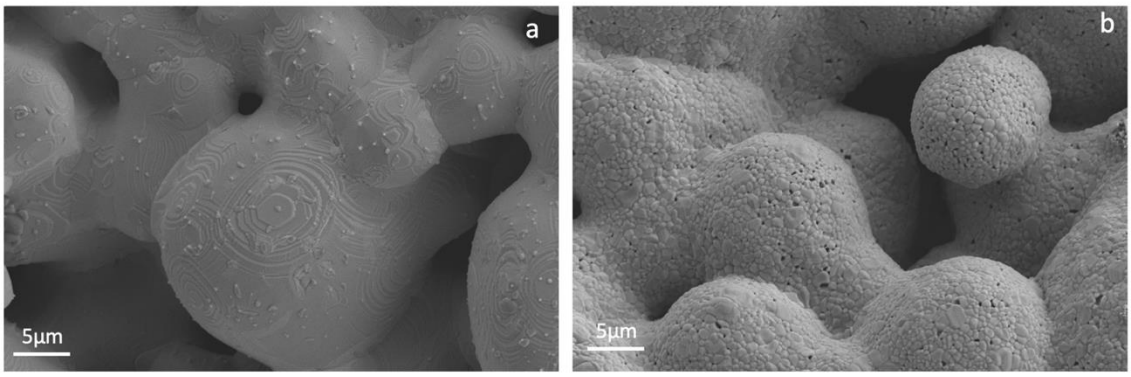

Figure 53. Surface microstructure of (a) uncoated sample and (b) $CuNi_{0.2}Mn_{1.8}O_4$ coated and densified sample.

Figure 53a shows the surface microstructure of an as-received uncoated sample and Figure 53b shows the coated sample before the oxidation test (after the coating densification anneal). The SUS430 stainless steel grains are well covered by a dense spinel layer. The pores on the surface are not blocked by the spinel coating.

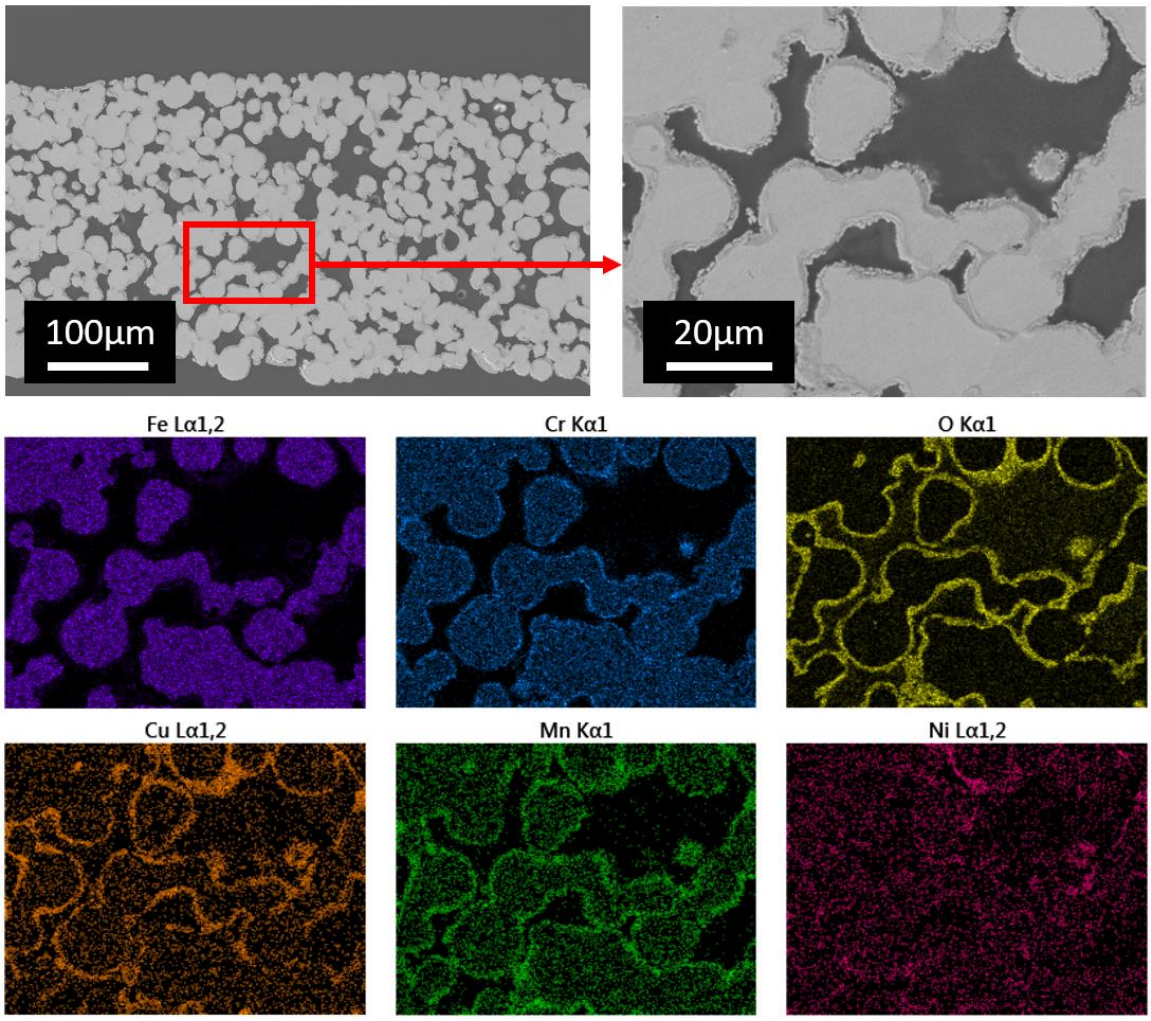

Figure 54. Low magnification SEM image, and EDS mapping of coated sample after two-step densification and 100h oxidation test.

Figure 54 shows a low magnification SEM image of the AC EPD sample after the 100h oxidation test and a randomly picked area inside the substrate is shown at higher magnification with EDS maps of the constitutive elements in the coating and substrate. The maps show the presence of the spinel coating on the surfaces throughout the pores. There is also a Cr rich layer formed at SUS430 pore surfaces, likely formed during the densification process. However, the spinel coating covers the Cr layer and protects the substrate from further oxidization.

Due to the tortuous surface morphology of the substrate, the diffusion rate of spinel powders can differ from pore to pore. Thus, it is more challenging to deposit uniform coatings on porous substrates than on flat samples. However, the figure clearly shows that there is AC EPD allows for reasonably uniform coverage of all pore surfaces in the sample, even for pores in the middle of the porous substrate.

Plots of the weight gain per unit area of the uncoated and coated samples as a function of oxidation time are shown in Figure 55. Oxidation rate constant k_p were calculated [32]. The fits give k_p values of 2.25×10^{-6} mg^2 cm^{-4} s^{-1} for the uncoated sample and 9.0×10^{-8} mg^2 cm^{-4} s^{-1} for the coated sample. The constant time period fluctuations in Figure 55a and b was due to the room temperature variation from day to night, which changes the density of air, and thus the buoyancy on the sample holder in the microbalance. These fluctuations are more obvious on coated sample due to the smaller total weight gain.

Figure 55c and d show the ASR changes during the 100 h exposure in air at 700°C. The ASR value of the uncoated sample increased significantly from 22 m**Ω•**cm^2 to 310 m**Ω•**cm^2 after the 100h oxidation at 700°C. In contrast, the value of the coated sample was

very stable. The ASR for the coated sample slightly decreased from 24 mΩ•cm^2 to 21 mΩ•cm^2 for the first 40 hours. This may due to better sintering of the silver paste and silver wire. This effect is also visible for the uncoated sample, when the increase in the ASR looks to be slower than after this time period. For the coated sample, the ASR increased from 20 mΩ•cm^2 to 22 mΩ•cm^2 from 50h to 100h. Clearly, the EPD coated sample exhibited a significantly superior ASR performance compared to the uncoated sample. This highlights the ability of the AC EPD process to deposit coatings on all surfaces of the porous substrate and significantly reduce the rate of further oxidation of the sample.

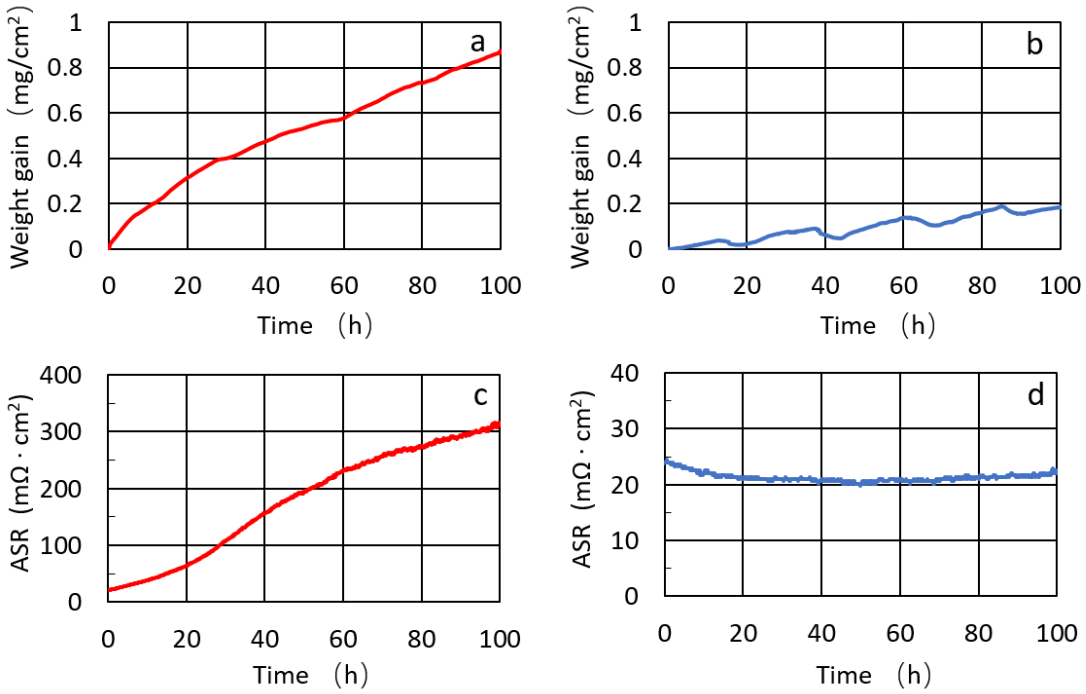

Figure 55. Plot of weight gain per unit area measured by thermogravimetry of (a) uncoated sample and (b) coated sample as a function of time. ASR changes as a function of time for uncoated sample (c) and coated sample (d). All the data are measured at 700 ℃ in air.

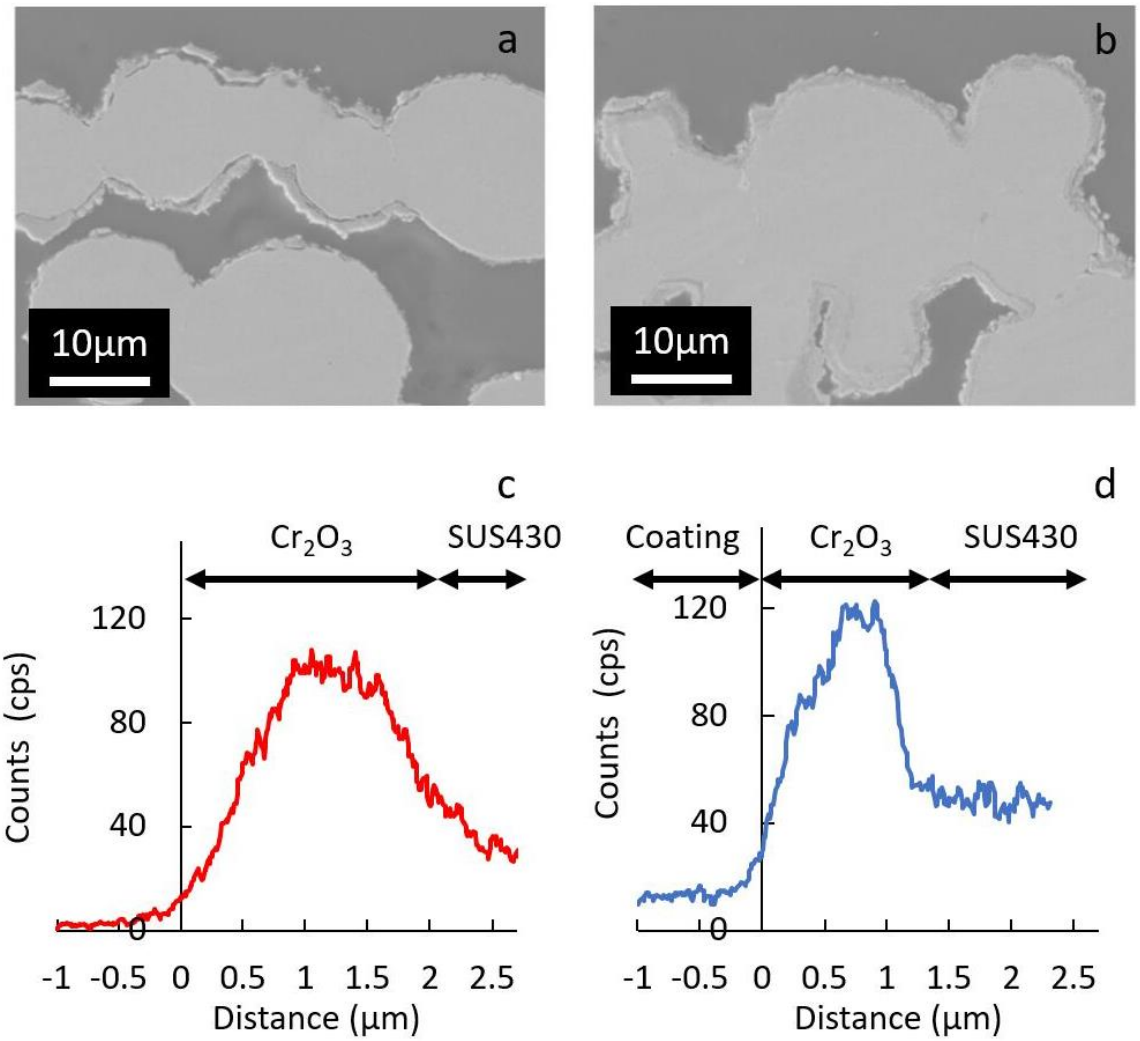

Figure 56. SEM micrographs of cross-sections after 100h oxidation test at 700 ℃ in air, of (a) uncoated sample and (b) coated sample. EDS line scans across the (c) TGO/substrate in the uncoated sample, and (d) coating/TGO/substrate in the coated sample.

Figure 56a and b show the microstructures of uncoated and coated samples after oxidation test. The Cr concentration was quantitatively measured by EDS line scan. Figure 56c and d show the Cr concentration profiles for uncoated and coated sample after the 100h oxidation test. The thickness of Cr_2O_3 for uncoated sample after oxidation is around 1.8 µm. The thickness of Cr_2O_3 for coated sample after oxidation at surface is around 1 µm.

There is a pre-formed Cr_2O_3 layer in coated sample before oxidation test, during the densification anneal at 950°C, before the coating has fully densified. Therefore, the growth rate of the TGO in the coated sample is much lower than in the uncoated sample. The TGA results show that the EPD coating layer on porous SUS430 substrate effectively limited Cr_2O_3 layer growth.

6.4 Conclusions

In this research, deposition of protective $CuNi_{0.2}Mn_{1.8}O_4$ spinel coatings on porous metallic substrates was studied. $CuNi_{0.2}Mn_{1.8}O_4$ spinel powders were made by glycine nitrate process and deposited on porous SUS430 substrates using AC EPD. As deposited samples were densified by a two-step densification anneal consisting of a reduction in H_2 at 950°C for 2h and re-oxidation in at 750°C for 24h in air. Oxidation tests at 700°C in air were carried out for 100h. TGA measurement shows that oxidation rate constant k_p for uncoated sample is 2.25×10^{-6} $mg^2\ cm^{-4}\ s^{-1}$ and for the coated sample is 9.0×10^{-8} $mg^2\ cm^{-4}\ s^{-1}$. ASR measurement shows the uncoated sample increased from 22 $m\Omega\bullet cm^2$ to 310 $m\Omega\bullet cm^2$. In contrast, the ASR of the coated sample was very stable and increased to only 25 $m\Omega\bullet cm^2$. EDS line scans showed that the thickness of Cr_2O_3 for uncoated sample after oxidation is around 1.8 μm, in contrast to 1.0 μm, for the coated sample, most of which formed during the two-step of the densification anneal. The TGA data, ASR measurements and EDS line scan results are consistent. The results confirm the significant positive effect of the EPD coating layer on protecting the porous SUS430 substrate from oxidation and keeping the ASR value low.

7. Conclusions

In this study, two strategies were explored to mitigate Cr poisoning. The first strategy is 'electrochemical cleaning', based on periodic reversible operation in a solid oxide electrolyser cell (SOEC) mode, which mitigates the deleterious effects of chromium poisoning by oxidizing the deposits species back into the vapor phase. LSM based solid oxide fuel cells were fabricated and tested at 800°C. After poisoning with humidified air passing through Cr_2O_3, under cathodic current, performance degradation due to Cr-poisoning was observed. SEM and EDS analyses of the poisoned baseline cell revealed two types of Cr deposits: Cr_2O_3 and (Cr,Mn) spinel. Electrochemical cleaning was implemented by operating the cell in the SOEC mode. A mild electrolytic cleaning condition was chosen to avoid irreversible damage to the cell. I-V and EIS analyses corroborated that chromium poisoning was reversed via electrochemical cleaning. Moreover, the electrochemically cleaned cell shows a relatively clean cathode/electrolyte interface, indicating that most of the Cr_2O_3 deposits were removed.

In order to demonstrate that electrochemical cleaning can be carried out periodically without damaging the cell, cells were subjected to three cycles of repeated poisoning and cleaning. It was found that a similar level of degradation and recovery happened after each cycle. After the third cycle, the cell still maintained the initial level of power output, indicating that periodic electrochemical cleaning under mild electrolytic conditions is an effective method to reverse chromium poisoning without damaging the cell.

The second strategy explored was the deposition of protective coatings on the

SUS430 stainless-steel interconnects. Four spinel compositions for these coatings were studied; $CuMn_2O_4$, $CuNi_{0.2}Mn_{1.8}O_4$, $MnCo_2O_4$, and $MnFe_{0.34}Co_{1.66}O_4$. The coatings were evaluated based on multiple criteria; including phase stability, microstructural stability, conductivity, Cr gettering ability, ability to act as a diffusion barrier to outward chromium and inward oxygen diffusion at 700ºC and 800ºC in dry and humidified air, and the ability to limit the increase in the area specific resistance during high temperature oxidation exposures. The results show that Cu-Mn based spinels have higher conductivities than Mn-Co based spinels. Doping Ni increased the conductivity of Cu-Mn spinel, but doping Fe decreased the conductivity of Mn-Co spinel. Mn-Co based spinels show a better ability to limit Cr layer growth than Cu-Mn spinels. $MnFe_{0.34}Co_{1.66}O_4$ shows the best performance in limiting TGO growth, it has better stability at high temperatures and the largest Cr getter ability but it also has the lowest electrical conductivity. $CuNi_{0.2}Mn_{1.8}O_4$ has the highest conductivity. It also has high phase stability, low porosity and better sinterability. Overall, $CuNi_{0.2}Mn_{1.8}O_4$ is the best option in four spinels.

The further optimization of the Ni doping content in $CuNi_xMn_{2-x}O_4$ spinels was carried out. $CuMn_2O_4$, $CuNi_{0.2}Mn_{1.8}O_4$, $CuNi_{0.4}Mn_{1.6}O_4$, and $CuNi_{0.6}Mn_{1.4}O_4$ spinel powers were prepared and deposited on flat SUS430 substrates. Oxidation test at 700°C and 800°C were carried out. The largest porosity in the $CuMn_2O_4$ sample made the coating layer brittle, and cracks formed during the oxidation test. Also, the unstable composition led the the formation of needle-like manganese oxide at room temperature. The porosity of the $CuNi_{0.4}Mn_{1.6}O_4$ coating was smaller than the $CuMn_2O_4$ coating, but still larger than the $CuNi_{0.2}Mn_{1.8}O_4$ coating. $CuNi_{0.6}Mn_{1.4}O_4$ has formed a Cu-rich layer on the coating surface.

The $CuNi_{0.2}Mn_{1.8}O_4$ shows the smallest porosity, largest conductivity at 700°C, and no second phase formation on the surface or in the coating layer. Therefore, a Ni doping of 0.2 was found to be optimal for doped Cu-Mn spinels.

To mitigate chromium diffusion from porous stainless steel substrates, alternating current deposition of spinel coating was studied. $CuNi_{0.2}Mn_{1.8}O_4$ spinel powders were prepared and deposited on porous SUS430 substrates using AC EPD. After densification, uniform and dense layers were covered on stainless steel grains. Oxidation tests at 700°C in air were carried out for 100h. The TGA data, ASR measurements, and EDS line scan were taken and compared to the uncoated sample. All the results were consistent and confirmed the significant positive effect of the EPD coating layer on protecting porous SUS430 substrates from oxidation and keeping the ASR value low.

8. Contributions and Recommendations for Future Work

8.1 Original Contributions

The original contributions to the literature based on this study include:

1. First demonstration of the feasibility of electrochemical cleaning in the literature.
2. First demonstration of the effectiveness of multiple cycles of cleaning in the literature.
3. To the best of our knowledge, the first comprehensive study of comparing the properties of doped and undoped Cu-Mn and Mn-Co based spinels, to identify optimal coating composition.
4. To the best of our knowledge, the first demonstration of AC EPD deposition of protective coatings on porous interconnects.

8.2 Future work on electrochemical cleaning

As reported in this thesis (Chapter 2), electrochemical cleaning parameters removed the chromium oxide phase, but not the spinel phase that formed on the cathode. Further research is required to devise strategies to remove the spinel deposits that form on the cathode without harming the cell. This is currently being studied by Ms. Michelle Sugimoto in our group.

8.3 Future work on spinel coatings for interconnects

Future work on spinel coatings for interconnects include:

1. Longer term (1000 h or greater testing of the coatings).

2. Understanding site occupancy of dopants in the spinel phase using Rietveld refinement of high-resolution X-ray data from doped spinel powders.
3. Quantify changes in oxygen and chromium diffusion in the spinels based on point-defect models.
4. Study changes in spinel conductivity based on Cr content.
5. Combine measured TGO growth kinetics, Cr diffusion kinetics and resultant decrease in conductivity to model long-term ASR changes in coated interconnects.

BIBLIOGRAPHY

[1] B. C. H. Steele, "Running on natural gas," *Nature,* vol. 400, no. 6745, pp. 619–621, 1999, doi: 10.1038/23144.

[2] A. B. Stambouli and E. Traversa, "Solid oxide fuel cells (SOFCs): a review of an environmentally clean and efficient source of energy," *Renewable and Sustainable Energy Reviews,* vol. 6, no. 5, pp. 433–455, 2002, doi: 10.1016/S1364-0321(02)00014-X.

[3] R. M. Ormerod, "Solid oxide fuel cells," *Chemical Society Reviews,* vol. 32, no. 1, pp. 17–28, 2003.

[4] S. Mekhilef, R. Saidur, and A. Safari, "Comparative study of different fuel cell technologies," *Renewable and Sustainable Energy Reviews,* vol. 16, no. 1, pp. 981–989, 2012.

[5] O. Yamamoto, "Solid oxide fuel cells: fundamental aspects and prospects," *Electrochimica Acta,* vol. 45, no. 15–16, pp. 2423–2435, 2000.

[6] S. C. Singhal, "Solid oxide fuel cells for stationary, mobile, and military applications," *Solid State Ionics,* vol. 152, pp. 405–410, 2002.

[7] N. Q. Minh, "Solid oxide fuel cell technology—features and applications," *Solid State Ionics,* vol. 174, no. 1–4, pp. 271–277, 2004.

[8] M. Kendall, "Fuel cell development for New Energy Vehicles (NEVs) and clean air in China," *Progress in Natural Science: Materials International,* vol. 28, no. 2, pp. 113–120, 2018.

[9] A. Hagen, A. C. Wulff, P. Zielke, X. Sun, B. Talic, I. Ritucci, H. L. Frandsen, S. Jensen, W.-R. Kiebach, and P. V. Hendriksen, "SOFC stacks for mobile applications with excellent robustness towards thermal stresses," *International Journal of Hydrogen Energy*, vol. 45, no. 53, pp. 29201–29211, 2020.

[10] S. C. Singhal, "Advances in solid oxide fuel cell technology," *Solid State Ionics*, vol. 135, no. 1–4, pp. 305–313, 2000.

[11] C. Sun, R. Hui, and J. Roller, "Cathode materials for solid oxide fuel cells: a review," *Journal of Solid State Electrochemistry*, vol. 14, no. 7, pp. 1125–1144, 2010.

[12] N. Mahato, A. Banerjee, A. Gupta, S. Omar, and K. Balani, "Progress in material selection for solid oxide fuel cell technology: A review," *Progress in Materials Science*, vol. 72, pp. 141–337, 2015.

[13] S. Badwal, S. Giddey, C. Munnings, and A. Kulkarni, "Review of progress in high temperature solid oxide fuel cells," *ChemInform*, vol. 46, no. 31, 2015.

[14] S. P. Jiang and S. H. Chan, "A review of anode materials development in solid oxide fuel cells," *Journal of Materials Science*, vol. 39, no. 14, pp. 4405–4439, 2004.

[15] T. Kariya, H. Tanaka, T. Hirono, T. Kuse, K. Yanagimoto, K. Uchiyama, M. Henmi, M. Hirose, I. Kimura, and K. Suu, "Development of a novel cell structure for low-temperature SOFC using porous stainless steel support combined with hydrogen permeable Pd layer and thin film proton conductor," *Journal of Alloys and Compounds*, vol. 654, pp. 171–175, 2016.

[16] S. Molin, B. Kusz, M. Gazda, and P. Jasinski, "Evaluation of porous 430L stainless steel for SOFC operation at intermediate temperatures," *Journal of Power Sources,* vol. 181, no. 1, pp. 31–37, 2008.

[17] J. W. Fergus, "Electrolytes for solid oxide fuel cells," *Journal of Power Sources,* vol. 162, no. 1, pp. 30–40, 2006.

[18] W. Zhu and S. Deevi, "A review on the status of anode materials for solid oxide fuel cells," *Materials Science and Engineering: A,* vol. 362, no. 1–2, pp. 228–239, 2003.

[19] D. J. Brett, A. Atkinson, N. P. Brandon, and S. J. Skinner, "Intermediate temperature solid oxide fuel cells," *Chemical Society Reviews,* vol. 37, no. 8, pp. 1568–1578, 2008.

[20] Z. Yang, "Recent advances in metallic interconnects for solid oxide fuel cells," *International Materials Reviews,* vol. 53, no. 1, pp. 39–54, 2008.

[21] T. Brylewski, M. Nanko, T. Maruyama, and K. Przybylski, "Application of Fe–16Cr ferritic alloy to interconnector for a solid oxide fuel cell," *Solid State Ionics,* vol. 143, no. 2, pp. 131–150, 2001.

[22] J. Wu and X. Liu, "Recent development of SOFC metallic interconnect," *Journal of Materials Science & Technology,* vol. 26, no. 4, pp. 293–305, 2010.

[23] T. Horita, H. Kishimoto, K. Yamaji, Y. Xiong, N. Sakai, M. E. Brito, and H. Yokokawa, "Evaluation of Laves-phase forming Fe–Cr alloy for SOFC interconnects in reducing atmosphere," *Journal of Power Sources,* vol. 176, no. 1, pp. 54–61, 2008.

[24] Z. Yang, G.-G. Xia, and J. W. Stevenson, "Evaluation of Ni–Cr-base alloys for SOFC interconnect applications," *Journal of Power Sources,* vol. 160, no. 2, pp. 1104–1110, 2006.

[25] Z. Yang, K. S. Weil, D. M. Paxton, and J. W. Stevenson, "Selection and evaluation of heat-resistant alloys for SOFC interconnect applications," *Journal of the Electrochemical Society,* vol. 150, no. 9, p. A1188, 2003.

[26] S. Badwal, R. Deller, K. Foger, Y. Ramprakash, and J. Zhang, "Interaction between chromia forming alloy interconnects and air," *Solid State Ionics,* vol. 99, pp. 297–310, 1997.

[27] L. Blum, W. A. Meulenberg, H. Nabielek, and R. Steinberger‐Wilckens, "Worldwide SOFC technology overview and benchmark," *International Journal of Applied Ceramic Technology,* vol. 2, no. 6, pp. 482–492, 2005.

[28] R. S. Gemmen and C. D. Johnson, "Evaluation of fuel cell system efficiency and degradation at development and during commercialization," *Journal of Power Sources,* vol. 159, no. 1, pp. 646–655, 2006, doi: 10.1016/j.jpowsour.2005.10.109.

[29] H. Yokokawa, H. Tu, B. Iwanschitz, and A. Mai, "Fundamental mechanisms limiting solid oxide fuel cell durability," *Journal of Power Sources,* vol. 182, no. 2, pp. 400–412, 2008.

[30] C. Gindorf, "Chromium Vaporization from Metallic Interconnect and Retention by Perovskite Layers," *ECS Proceedings Volumes,* vol. 1999-19, no. 1, pp. 774–782, 1999, doi: 10.1149/199919.0774PV.

[31] K. Hilpert, D. Das, M. Miller, D. Peck, and R. Weiss, "Chromium vapor species over solid oxide fuel cell interconnect materials and their potential for degradation processes," *Journal of the Electrochemical Society,* vol. 143, no. 11, p. 3642, 1996.

[32] S. Heo, J. Hong, A. Aphale, B. Hu, and P. Singh, "Chromium Poisoning of $La_{1-x}Sr_xMnO_{3\pm\delta}$ Cathodes and Electrochemical Validation of Chromium Getters in Intermediate Temperature-Solid Oxide Fuel Cells," *Journal of The Electrochemical Society,* vol. 166, no. 13, 2019, doi: 10.1149/2.0931913jes.

[33] S. Wang, T. A. Cruse, M. Krumpelt, B. J. Ingram, and P. A. Salvador, "Microstructural Degradation of (La,Sr)MnO_3/YSZ Cathodes in Solid Oxide Fuel Cells with Uncoated E-Brite Interconnects," *Journal of The Electrochemical Society,* vol. 158, no. 2, 2011, doi: 10.1149/1.3515073.

[34] E. Konysheva, H. Penkalla, E. Wessel, J. Mertens, U. Seeling, L. Singheiser, and K. Hilpert, "Chromium poisoning of perovskite cathodes by the ODS alloy $Cr_5Fe_1Y_2O_3$ and the high chromium ferritic steel Crofer22APU," *Journal of the Electrochemical Society,* vol. 153, no. 4, pp. A765–A773, 2006.

[35] R. Wang, M. Würth, U. B. Pal, S. Gopalan, and S. N. Basu, "Roles of humidity and cathodic current in chromium poisoning of Sr-doped $LaMnO_3$-based cathodes in solid oxide fuel cells," *Journal of Power Sources,* vol. 360, pp. 87–97, 2017, doi: 10.1016/j.jpowsour.2017.06.005.

[36] R. Wang, Z. Sun, U. B. Pal, S. Gopalan, and S. N. Basu, "Mitigation of chromium poisoning of cathodes in solid oxide fuel cells employing $CuMn_{1.8}O_4$ spinel coating on metallic interconnect," *Journal of Power Sources,* vol. 376, pp. 100–110, 2018.

[37] X. Chen, "Chromium deposition and poisoning of cathodes of solid oxide fuel cells–a review," *International Journal of Hydrogen Energy,* vol. 39, no. 1, pp. 505–531, 2014.

[38] S. Jiang and X. Chen, "Chromium deposition and poisoning of cathodes of solid oxide fuel cells – A review," *International Journal of Hydrogen Energy,* vol. 39, no. 1, pp. 505–531, 2014, doi: 10.1016/j.ijhydene.2013.10.042.

[39] Z. Sun, S. Gopalan, U. B. Pal, and S. N. Basu, "$Cu_{1.3}Mn_{1.7}O_4$ spinel coatings deposited by electrophoretic deposition on Crofer 22 APU substrates for solid oxide fuel cell applications," *Surface and Coatings Technology,* vol. 323, pp. 49–57, 2017.

[40] Z. Sun, R. Wang, A. Y. Nikiforov, S. Gopalan, U. B. Pal, and S. N. Basu, "$CuMn_{1.8}O_4$ protective coatings on metallic interconnects for prevention of Cr-poisoning in solid oxide fuel cells," *Journal of Power Sources,* vol. 378, pp. 125–133, 2018.

[41] Z. Zhu, M. Sugimoto, U. Pal, S. Gopalan, and S. Basu, "Electrochemical cleaning: An in-Situ method to reverse chromium poisoning in solid oxide fuel cell cathodes," *Journal of Power Sources,* vol. 471, p. 228474, 2020.

[42] Z. Zhu, M. Sugimoto, U. Pal, S. Gopalan, and S. Basu, "Multiple cycle chromium poisoning and in-situ electrochemical cleaning of LSM-based solid oxide fuel cell cathodes," *Journal of Power Sources Advances,* vol. 6, p. 100037, 2020.

[43] S. J. Heo, J. Hong, A. Aphale, B. Hu, and P. Singh, "Chromium poisoning of $La_{1-x}Sr_xMnO_{3\pm\delta}$ cathodes and electrochemical validation of chromium getters in

intermediate temperature-solid oxide fuel cells," *Journal of The Electrochemical Society*, vol. 166, no. 13, p. F990, 2019.

[44] M. Reisert, A. Aphale, and P. Singh, "Solid oxide electrochemical systems: Material degradation processes and novel mitigation approaches," *Materials*, vol. 11, no. 11, p. 2169, 2018.

[45] Y. Chen, S. Yoo, X. Li, D. Ding, K. Pei, D. Chen, Y. Ding, B. Zhao, R. Murphy, and B. Deglee, "An effective strategy to enhancing tolerance to contaminants poisoning of solid oxide fuel cell cathodes," *Nano Energy*, vol. 47, pp. 474–480, 2018.

[46] K. Fujita, K. Ogasawara, Y. Matsuzaki, and T. Sakurai, "Prevention of SOFC cathode degradation in contact with Cr-containing alloy," *Journal of Power Sources*, vol. 131, no. 1–2, pp. 261–269, 2004, doi: 10.1016/j.jpowsour.2003.12.051.

[47] N. Shaigan, W. Qu, D. G. Ivey, and W. Chen, "A review of recent progress in coatings, surface modifications and alloy developments for solid oxide fuel cell ferritic stainless steel interconnects," *Journal of Power Sources*, vol. 195, no. 6, pp. 1529–1542, 2010.

[48] M. Stanislowski, J. Froitzheim, L. Niewolak, W. J. Quadakkers, K. Hilpert, T. Markus, and L. Singheiser, "Reduction of chromium vaporization from SOFC interconnectors by highly effective coatings," *Journal of Power Sources*, vol. 164, no. 2, pp. 578–589, 2007, doi: 10.1016/j.jpowsour.2006.08.013.

[49] M. Krumpelt, T. A. Cruse, B. J. Ingram, J. L. Routbort, S. Wang, P. A. Salvador, and G. Chen, "The Effect of Chromium Oxyhydroxide on Solid Oxide Fuel Cells," *Journal of The Electrochemical Society,* vol. 157, no. 2, 2010, doi: 10.1149/1.3266930.

[50] S. C. Paulson and V. I. Birss, "Chromium Poisoning of LSM-YSZ SOFC Cathodes," *Journal of The Electrochemical Society,* vol. 151, no. 11, 2004, doi: 10.1149/1.1806392.

[51] S. Taniguchi, M. Kadowaki, H. Kawamura, T. Yasuo, Y. Akiyama, Y. Miyake, and T. Saitoh, "Degradation phenomena in the cathode of a solid oxide fuel cell with an alloy separator," *Journal of Power Sources,* vol. 55, no. 1, pp. 73–79, 1995.

[52] R. Wang, U. B. Pal, S. Gopalan, and S. N. Basu, "Chromium Poisoning Effects on Performance of (La,Sr)MnO_3-Based Cathode in Anode-Supported Solid Oxide Fuel Cells," *Journal of The Electrochemical Society,* vol. 164, no. 7, 2017, doi: 10.1149/2.0441707jes.

[53] A. R. Boccaccini and I. Zhitomirsky, "Application of electrophoretic and electrolytic deposition techniques in ceramics processing," *Current Opinion in Solid State and Materials Science,* vol. 6, no. 3, pp. 251–260, 2002.

[54] L. Besra and M. Liu, "A review on fundamentals and applications of electrophoretic deposition (EPD)," *Progress in Materials Science,* vol. 52, no. 1, pp. 1–61, 2007.

[55] I. Aznam, J. C. W. Mah, A. Muchtar, M. R. Somalu, and M. J. Ghazali, "A review of key parameters for effective electrophoretic deposition in the fabrication of solid

oxide fuel cells," *Journal of Zhejiang University-Science A,* vol. 19, no. 11, pp. 811–823, 2018.

[56] L. Kremser, D. Blaas, and E. Kenndler, "Capillary electrophoresis of biological particles: viruses, bacteria, and eukaryotic cells," *Electrophoresis,* vol. 25, no. 14, pp. 2282–2291, 2004.

[57] H.-J. Keh and J. Anderson, "Boundary effects on electrophoretic motion of colloidal spheres," *Journal of Fluid Mechanics,* vol. 153, pp. 417–439, 1985.

[58] M. R. Bateni, P. Wei, X. Deng, and A. Petric, "Spinel coatings for UNS 430 stainless steel interconnects," *Surface and Coatings Technology,* vol. 201, no. 8, pp. 4677–4684, 2007.

[59] P. Gannon, M. Deibert, P. White, R. Smith, H. Chen, W. Priyantha, J. Lucas, and V. Gorokhovsky, "Advanced PVD protective coatings for SOFC interconnects," *International Journal of Hydrogen Energy,* vol. 33, no. 14, pp. 3991–4000, 2008.

[60] V. I. Gorokhovsky, P. Gannon, M. Deibert, R. J. Smith, A. Kayani, M. Kopczyk, D. VanVorous, Z. Yang, J. W. Stevenson, and S. Visco, "Deposition and evaluation of protective PVD coatings on ferritic stainless steel SOFC interconnects," *Journal of The Electrochemical Society,* vol. 153, no. 10, p. A1886, 2006.

[61] S. Beresnev, O. Bobrenok, B. Kuzin, N. Bogdanovich, A. Kurteeva, D. Osinkin, G. Vdovin, and D. Bronin, "Single fuel cell with supported LSM cathode," *Russian Journal of Electrochemistry,* vol. 48, no. 10, pp. 969–975, 2012.

[62] S. Fontana, R. Amendola, S. Chevalier, P. Piccardo, G. Caboche, M. Viviani, R. Molins, and M. Sennour, "Metallic interconnects for SOFC: Characterisation of

corrosion resistance and conductivity evaluation at operating temperature of differently coated alloys," *Journal of Power Sources,* vol. 171, no. 2, pp. 652–662, 2007.

[63] G. Cabouro, G. Caboche, S. Chevalier, and P. Piccardo, "Opportunity of metallic interconnects for ITSOFC: Reactivity and electrical property," *Journal of Power Sources,* vol. 156, no. 1, pp. 39–44, 2006.

[64] L. Mikkelsen, M. Chen, P. V. Hendriksen, Å. Persson, N. Pryds, and K. Rodrigo, "Deposition of $La_{0.8}Sr_{0.2}Cr_{0.97}V_{0.03}O_3$ and $MnCr_2O_4$ thin films on ferritic alloy for solid oxide fuel cell application," *Surface and Coatings Technology,* vol. 202, no. 4–7, pp. 1262–1266, 2007.

[65] W. Qu, L. Jian, D. G. Ivey, and J. M. Hill, "Yttrium, cobalt and yttrium/cobalt oxide coatings on ferritic stainless steels for SOFC interconnects," *Journal of Power Sources,* vol. 157, no. 1, pp. 335–350, 2006.

[66] B. Chi, J. Li, X. Yang, H. Lin, and N. Wang, "Electrophoretic deposition of $ZnCo_2O_4$ spinel and its electrocatalytic properties for oxygen evolution reaction," *Electrochimica Acta,* vol. 50, no. 10, pp. 2059–2064, 2005.

[67] J. Zhu, Y. Zhang, A. Basu, Z. Lu, M. Paranthaman, D. Lee, and E. Payzant, "$LaCrO_3$-based coatings on ferritic stainless steel for solid oxide fuel cell interconnect applications," *Surface and Coatings Technology,* vol. 177, pp. 65–72, 2004.

[68] Z. Yang, G. Xia, S. P. Simner, and J. W. Stevenson, "Thermal growth and performance of manganese cobaltite spinel protection layers on ferritic stainless

steel SOFC interconnects," *Journal of The Electrochemical Society,* vol. 152, no. 9, p. A1896, 2005.

[69] J. C. Mah, A. Muchtar, M. R. Somalu, and M. J. Ghazali, "Metallic interconnects for solid oxide fuel cell: A review on protective coating and deposition techniques," *International Journal of Hydrogen Energy,* vol. 42, no. 14, pp. 9219–9229, 2017.

[70] E. Stefan, D. Neagu, P. B. Tullmar, Å. H. Persson, B. R. Sudireddy, D. Miller, M. Chen, and J. Irvine, "Spinel-based coatings for metal supported solid oxide fuel cells," *Materials Research Bulletin,* vol. 89, pp. 232–244, 2017.

[71] E. Zanchi, A. Sabato, S. Molin, G. Cempura, A. Boccaccini, and F. Smeacetto, "Recent advances on spinel-based protective coatings for solid oxide cell metallic interconnects produced by electrophoretic deposition," *Materials Letters,* vol. 286, p. 129229, 2021.

[72] A. Petric and H. Ling, "Electrical conductivity and thermal expansion of spinels at elevated temperatures," *Journal of the American Ceramic Society,* vol. 90, no. 5, pp. 1515–1520, 2007.

[73] T. Uehara, N. Yasuda, M. Okamoto, and Y. Baba, "Effect of Mn–Co spinel coating for Fe–Cr ferritic alloys ZMG232L and 232J3 for solid oxide fuel cell interconnects on oxidation behavior and Cr-evaporation," *Journal of Power Sources,* vol. 196, no. 17, pp. 7251–7256, 2011.

[74] H. Zhang, Z. Zhan, and X. Liu, "Electrophoretic deposition of $(Mn, Co)_3O_4$ spinel coating for solid oxide fuel cell interconnects," *Journal of Power Sources,* vol. 196, no. 19, pp. 8041–8047, 2011.

[75] H. Abdoli and P. Alizadeh, "Electrophoretic deposition of (Mn, Co)$_3$O$_4$ spinel nano powder on SOFC metallic interconnects," *Materials Letters*, vol. 80, pp. 53–55, 2012.

[76] B. Talic, P. V. Hendriksen, K. Wiik, and H. L. Lein, "Thermal expansion and electrical conductivity of Fe and Cu doped MnCo$_2$O$_4$ spinel," *Solid State Ionics*, vol. 326, pp. 90–99, 2018.

[77] Z. Yang, G.-G. Xia, X.-H. Li, and J. W. Stevenson, "(Mn, Co)$_3$O$_4$ spinel coatings on ferritic stainless steels for SOFC interconnect applications," *International Journal of Hydrogen Energy*, vol. 32, no. 16, pp. 3648–3654, 2007.

[78] T. Brylewski, W. Kucza, A. Adamczyk, A. Kruk, M. Stygar, M. Bobruk, and J. Dąbrowa, "Microstructure and electrical properties of $Mn_{1+x}Co_{2-x}O_4$ ($0 \leq x \leq 1.5$) spinels synthesized using EDTA-gel processes," *Ceramics International*, vol. 40, no. 9, pp. 13873–13882, 2014.

[79] K. Wang, Y. Liu, and J. W. Fergus, "Interactions between SOFC interconnect coating materials and chromia," *Journal of the American Ceramic Society*, vol. 94, no. 12, pp. 4490–4495, 2011.

[80] M. Galbo, K. J. Yoon, U. B. Pal, S. Gopalan, and S. N. Basu, "Evaluating electrophoretically deposited Cu-Mn-O spinel coatings on stainless steel substrates used in solid oxide fuel cell interconnects," in *Energy Technology 2015*: Springer, 2015, pp. 337–344.

[81] S. Joshi, C. Silva, P. Wang, Y. Mozharivskyj, and A. Petric, "Copper-Magnesium-Manganese spinel coatings for solid oxide fuel cell interconnects," *Journal of The Electrochemical Society,* vol. 161, no. 3, p. F233, 2013.

[82] Z. Sun, S. Gopalan, U. B. Pal, and S. N. Basu, "Electrophoretically deposited copper manganese spinel coatings for prevention of chromium poisoning in solid oxide fuel cells," in *Energy Technology 2019*: Springer, 2019, pp. 265–272.

[83] K. Yoon, P. Zink, S. Gopalan, and U. B. Pal, "Polarization measurements on single-step co-fired solid oxide fuel cells (SOFCs)," *Journal of Power Sources,* vol. 172, no. 1, pp. 39–49, 2007, doi: 10.1016/j.jpowsour.2007.03.003.

[84] M. A. Laguna-Bercero, "Recent advances in high temperature electrolysis using solid oxide fuel cells: A review," *Journal of Power Sources,* vol. 203, pp. 4–16, 2012, doi: 10.1016/j.jpowsour.2011.12.019.

[85] H. Kurokawa, C. P. Jacobson, L. C. DeJonghe, and S. J. Visco, "Chromium vaporization of bare and of coated iron–chromium alloys at 1073 K," *Solid State Ionics,* vol. 178, no. 3–4, pp. 287–296, 2007, doi: 10.1016/j.ssi.2006.12.010.

[86] Y. Matsuzaki and I. Yasuda, "Electrochemical properties of a SOFC cathode in contact with a chromium-containing alloy separator," *Solid State Ionics,* vol. 132, no. 3–4, pp. 271–278, 2000.

[87] S. Jiang, J. Zhang, L. Apateanu, and K. Foger, "Deposition of Chromium Species at Sr‐Doped $LaMnO_3$ Electrodes in Solid Oxide Fuel Cells. I. Mechanism and Kinetics," *Journal of The Electrochemical Society,* vol. 147, no. 11, p. 4013, 2000.

[88] M. C. Tucker, H. Kurokawa, C. P. Jacobson, L. C. Jonghe, and S. J. Visco, "A fundamental study of chromium deposition on solid oxide fuel cell cathode materials," *Journal of Power Sources,* vol. 160, no. 1, pp. 130–138, 2006, doi: 10.1016/j.jpowsour.2006.02.017.

[89] D. Röhrens, A. Neumann, A. Beez, I. Vinke, L. de Haart, and N. Menzler, "Formation of chromium containing impurities in (La, Sr)MnO_3 solid-oxide-fuel-cell cathodes under stack operating conditions and its effect on performance," *Ceramics International,* vol. 42, no. 8, pp. 9467–9474, 2016.

[90] L. A. Chick, L. Pederson, G. Maupin, J. Bates, L. Thomas, and G. Exarhos, "Glycine-nitrate combustion synthesis of oxide ceramic powders," *Materials Letters,* vol. 10, no. 1–2, pp. 6–12, 1990.

[91] N. Hosseini, M. Abbasi, F. Karimzadeh, and G. Choi, "Development of $Cu_{1.3}Mn_{1.7}O_4$ spinel coating on ferritic stainless steel for solid oxide fuel cell interconnects," *Journal of Power Sources,* vol. 273, pp. 1073–1083, 2015.

CURRICULUM VITAE

[redacted]

[redacted]